Development of ion beam sputtering for multilayer dispersive mirrors

Yu Chen

München 2021

Development of ion beam sputtering for multilayer dispersive mirrors

Yu Chen

Dissertation
der Fakultät für Physik
der Ludwig-Maximilians-Universität
München

vorgelegt von
Yu Chen
aus Shandong, China

München, den 20.10.2021

Erstgutachter: Prof. Dr. Ferenc Krausz
Zweitgutachter: Prof. Dr. Vitaly Gruzdev
Tag der mündlichen Prüfung: 09.12.2021

Contents

Zusammenfassung viii

Abstract x

List of Publications xi

List of Figures xiv

List of Tables xv

1 Introduction 1
- 1.1 Motivation . . . 1
- 1.2 Thesis outline . . . 3

2 Theoretical background 5
- 2.1 Description of ultrashort pulses . . . 5
- 2.2 Influence of different dispersion characteristics on ultrashort pulses . . . 7
- 2.3 Dispersion compensation for ultrashort pulses . . . 10
  - 2.3.1 Grating compressors . . . 10
  - 2.3.2 Prism compressors . . . 11
  - 2.3.3 Multilayer dispersive mirrors . . . 12
    - 2.3.3.1 Design process of multilayer dispersive mirrors . . . 12
    - 2.3.3.2 Concept of suppressing GDD oscillations . . . 16

3 Experimental techniques 19
- 3.1 Coating process . . . 19
  - 3.1.1 Electron beam evaporation . . . 19
  - 3.1.2 Magnetron sputtering . . . 21
  - 3.1.3 Ion beam sputtering . . . 23
    - 3.1.3.1 Layer thickness control technique . . . 23
    - 3.1.3.2 Adjusting the non-uniformity . . . 25
- 3.2 Characterization of multilayer dispersive mirrors . . . 26
  - 3.2.1 Transmittance, reflectance and total loss . . . 26
  - 3.2.2 GD and GDD . . . 28

4 Dispersive mirrors with IBS and comparison with MS 29
4.1 Design, production and characterization of BBDMs 30
4.1.1 Design of BBDMs 30
4.1.2 Deposition and characterization of BBDMs 32
4.2 Design, production and characterization of the robust HDMs 34
4.2.1 Design of HDMs 34
4.2.2 Deposition and characterization of HDMs 36
4.3 Comparison of IBS with MS 37
4.4 Conclusion and outlook 39

5 New approaches to suppress the GDD oscillations 41
5.1 Suppression of GDD oscillations of HDMs by non-uniformity and post-deposition treatment 41
5.1.1 Design of the HDM 42
5.1.2 Deposition and characterization 43
5.1.3 Post-deposition annealing and discussion 46
5.1.4 Conclusions 49
5.2 One octave DM pair with smooth GDD characteristics based on non-uniformity 50
5.2.1 Design and production of the one octave DM pair 52
5.2.2 Comparison of the one octave DM pair with double angle DM pair 56
5.2.2.1 GDD characteristics 56
5.2.2.2 Pulse analysis 58
5.2.3 Conclusions 60

6 3-6 μm dispersive mirrors compensating the dispersion introduced by the GaAs crystal 61
6.1 Determination of the refractive indices of the layer materials 62
6.2 Design and production of the DMs 64
6.3 Characterization of the DMs 65
6.4 Conclusions and outlook 67

7 Production of multilayer coatings with large substrates 69
7.1 300 × 130 mm rectangular HR coatings 69
7.2 200 mm in diameter chirped mirrors 70
7.3 Conclusions 73

8 Summary and outlook 75

A Ion beam sputtering coating process 77

B Data archiving 79

Bibliography 81

Danksagung **95**

Zusammenfassung

Die Erzeugung von ultrakurzen Laserpulsen benötigt passende Verstärkungsmedien, Modenkopplung, sowie eine ausgezeichnete Dispersionskompensation. Diese kann man mit dispersiven Spiegeln erreichen. Diese Spiegel bestehen aus dutzenden aperiodischen Schichten und erzeugen die gewünschte Dispersion mit Hilfe der von der Wellenlänge abhängigen Eindringtiefe und den Resonanzen für bestimmte Frequenzen. Dispersive Spiegel, die eine präzise Dispersionskontrolle mit hoher Genauigkeit und Effizienz ermöglichen, sind eine unverzichtbare Komponente bei der Erzeugung ultrakurzer Laserpulse. Laserpulse mit nur wenigen Schwingungen des elektrischen Feldes und einer mittleren Leistung im kW-Bereich sind von großer Bedeutung für Kielfeld-Beschleuniger und Thompson-Röntgenquellen mit hoher Brillianz. Die Erzeugung solcher hochintensiven ultrakurzen Pulse benötigt großflächige, hochqualitative optische Beschichtungen, zu denen Beschichtungen mit einer hohen Reflektivität gehören, um mehrere Reflexionen in einer nichtlinearen Verbreiterungsstufe zu ermöglichen, sowie dispersive Spiegel, um die Dispersion zu kontrollieren. Die Physikalische Gasphasenabscheidung wurde lange verwendet, um optische Beschichtungen für die verschiedensten Typen von Lasern zu produzieren. Sputtern ist das bisher beste und am meisten verbreitete Verfahren zur Produktion mehrlagiger dispersiver Spiegel wegen seiner hohen Schichtdickengenauigkeit. Ionenstrahlsputtern als einer der Sputtermethoden, die es ermöglicht großflächige mehrlagige Beschichtungen herzustellen, bei gleichzeitig minimalen Verlusten und einer hohen Zerstörschwelle.

Als erstes wurde das Ionenstrahlsputtern mit dem Ziel, mehrlagige dispersive Spiegel, weiterentwickelt. Dazu zählen breitbandige dispersive Spiegel und hochdispersive Spiegel. Dies sind beides Typen dispersiver Spiegel, die empfindlich auf verschiedene Beschichtungsfehler reagieren. Eine erfolgreiche Produktion dieser beiden Spiegeltypen würde belegen, dass Ionenstrahlsputtern in der Lage ist dispersiven Spiegel herzustellen. Außerdem, es wurde ein direkter Vergleich, basierend auf breitbandigen dispersiven Spiegeln und hochdispersiven Spiegeln bzgl. der Gruppenphasenverzögerung, zwischen Ionenstrahl- und Magentronsputtern gezogen. Ein Vergleich der Gruppenphasenverzögerung hat gezeigt, dass Ionenstrahlsputtern eine vergleichbare Genauigkeit bei der Schichtdicke wie Magetronsputtern erreicht und damit in der Lage ist dispersive Spiegel zu beschichten.

Außerdem haben Oszillationen der Gruppenphasenverzögerung, die nachteilig für ultrakurze Laserpulse sind, immer die Entwicklung dispersiver Spiegel begleitet. Als erstes wurden Oszillationen in der Gruppenphasenverzögerung eines einzelnen hochdispersiven Spiegels mithilfe eines hochdispersiven Spiegelpaars unterdrückt, welches einen fest-

gelegte spektrale Verschiebung zueinander hat. Diese spektrale Verschiebung wurde durch die Kombination der Inhomogenität der Beschichtungsanlage, sowie tempern nach der Beschichtung erzeugt. Als zweites wurde ein neuartiges Spiegelpaar mit einer Bandbreite von einer Oktave und einer glatten Gruppenphasenverzögerung demonstriert. Durch die frei einstellbaren Beschichtungsparameter beim Ionenstrahlsputtern war es möglich, die gewünschte Inhomogenität durch die Veränderung des Abstands zwischen Substrat und Sputterziel zu erreichen. Im Vergleich zu den weit verbreiteten dispersiven Spiegeln mit zwei verschiedenen Einfallswinkeln, sind die neuen Spiegelpaare für beide Polarisationen einsetzbar und weniger empfindlich beim Einfallswinkel.

Um den möglichen Einsatzbereich des Ionenstrahlsputterns in den mittelinfraroten Spektralbereich zu vergrößern, wurde ein dispersiver Spiegel für die Wellenlänge von 3-6 μm, der die Dispersion eines 0.5 mm dicken GaAs-Kristalls kompensieren soll, entworfen, produziert und charakterisiert. Dazu wurde die neue Materialkombination aus Si und SiO_2 verwendet, um den Spiegel zu produzieren. Mit diesem neuen dispersiven Spiegel kann die Dispersion eines GaAs-Kristalls perfekt kompensiert wurden, was ein noch breiteres Spektrum und die Erzeugung noch kürzerer Pulse ermöglicht.

Als letztes wurden noch zwei großflächige Beschichtungen mit Hilfe des Ionenstrahlsputterns hergestellt. Dazu gehören ein 300 $\times$ 130 mm hochreflektiver Spiegel und ein dispersiver Spiegel mit einem Durchmesser von 200 mm. Diese beiden Beschichtungen widerstehen dabei ultrakurzen Pulsen mit Energien von bis zu 100 mJ und einer Pulsfrequenz im multi-kHz Bereich. Außerdem hat die erfolgreiche Entwicklung dieser beiden Beschichtungen gezeigt, dass das Ionenstrahlsputtern in der Lage ist, großflächige Substrate zu beschichten.

Abstract

Ultrashort pulse generation relies on proper gain media and mode-locking techniques as well as perfect dispersion compensation. The perfect dispersion compensation can be achieved with dispersive mirrors. These dispersive mirrors consist of dozens of aperiodic layers and introduce the desired dispersion by the wavelength-dependent penetration effect and frequency trapping resonance effect. Dispersive mirrors providing dispersion compensation with excellent accuracy and efficiency have been the indispensable components for ultrashort pulse. Few-cycle ultrashort pulse with kilowatt scale average power and hundreds of millijoule of pulse energy are of great interest for kilohertz laser wavefield acceleration experiments or high photon flux Thmopson x-ray sources. Such intense and ultrashort pulses generation requires large-scale and high-quality optical coatings, which include high reflective coatings for providing multiple reflections in a multipass nonlinear broadening stage and dispersive mirrors for compensating the dispersion. Physical vapor deposition techniques have long been used to deposit optical coatings for all kinds of lasers. Sputtering has been the most successful and widely-used technique for the production of multilayer dispersive mirrors due to the accurate layer thickness control. Ion beam sputtering (IBS) as one form of sputtering has the advantage of being able to produce large-scale, low-loss and high damage threshold multilayer coatings.

First, IBS has been developed towards the production of multilayer dispersive mirrors, including broadband dispersive mirrors (BBDMs) and high dispersive mirrors (HDMs). BBDMs and HDMs are two kinds of dispersive mirrors and sensitive to different deposition errors. Successfully producing these dispersive mirrors shows the ability of IBS to produce multilayer dispersive mirrors. Moreover, a direct comparison between IBS and magnetron sputtering (MS) based on BBDMs and HDMs in terms of group delay dispersion (GDD) characteristics has been investigated. GDD comparison has verified that the IBS has comparable deposited thickness accuracy to MS and is capable of depositing dispersive mirrors.

Furthermore, the unavoidable GDD oscillations have always accompanied the development of dispersive mirrors, which are detrimental for ultrashort laser pulse. Two mirror-pair methods have been proposed to suppress GDD oscillations. In the first method, GDD oscillations of high dispersive mirrors were suppressed with a high dispersive mirror pair with certain spectral shift. Such spectral shift was realized by combining the non-uniformity in the coating plant and post-deposition annealing. In the second method, a new one octave dispersive mirror pair with smooth GDD oscillations was demonstrated. The suppression

of GDD oscillations for the novel dispersive mirror pair was realized with the desired non-uniformity. Thanks to the high degrees of freedom in adjusting the coating parameters of the IBS technology, the desired non-uniformity can be obtained by changing the distance between the target and substrates. Compared to the widely-used double angle dispersive mirror pair, the new dispersive mirror pair has the advantages of working at both polarizations and less sensitive to the angle of incidence.

In order to extend the working range of IBS to mid-infrared range, a 3 to 6 μm dispersive mirror compensating the dispersion introduced by a 0.5 mm thick GaAs crystal has been designed, produced and characterized. A new Si and SiO_2 material combination was employed to synthesize the new dispersive mirror. With the new dispersive mirror, the dispersion of the GaAs crystal can be perfectly compensated, which realize even wider spectrum and shorter pulse generation.

Last but not least, two large-scale multilayer coatings were produced with the IBS technology, which include the 300 $\times$ 130 mm high reflective mirrors and the 200 mm in diameter chirped mirrors. These multilayer coatings support the ultrashort pulses with energies up to 100 mJ and a multi-kilohertz repetition rate. Furthermore, the successful development of both multilayer coatings has demonstrated the capacity of IBS to coat large diameter substrates.

List of Publications

Journal Articles

Yu Chen, Daniel Hahner, Michael Trubetskov and Vladimir Pervak, “Suppression of group delay dispersion oscillations of highly dispersive mirrors by non-uniformity and post-deposition treatment”, Optics and Laser Technology, 142 2021.

Contribution: I came up with the new concept for suppressing GDD oscillations. I designed and produced the mirrors as well as performed the simulations and measurements.

Yu Chen, Daniel Hahner and Vladimir Pervak, “3-6 µm dispersive mirrors compensating the dispersion introduced by the GaAs crystal”, Applied Optics, 60(29) 2021.

Contribution: I designed and produced the mirrors as well as performed the simulations and measurements.

Yu Chen, Daniel Hahner, Michael Trubetskov and Vladimir Pervak, “One octave dispersive mirror pair” In preparation.

Contribution: I designed and produced the mirrors as well as performed the simulations and measurements.

Yu Chen, Daniel Hahner, Michael Trubetskov, Stefan Schrameyer, Wjatscheslaw Sakiew, Kai Starke and Vladimir Pervak, “Comparison of magnetron sputtering and ion beam sputtering on dispersive mirrors”, Applied Physics B, 126(5) 2020.

Contribution: I designed and produced the mirrors as well as performed the measurements and analyzed the results.

Penghui Ma, **Yu Chen**, Tatiana Amotchkina, Michael Trubetskov, Vladimir Pervak, and Li Li, “Design, fabrication and measurement of highly-dispersive mirrors with total internal reflection”, Optics Express, 28(20) 2020.

Contribution: I characterized the sample and discussed the results.

Martin Kaumanns, Vladimir Pervak, Dmitrii Kormin, Vyacheslav Leshchenko, Alexander Kessel, Moritz Ueffing, **Yu Chen**, and Thomas Nubbemeyer, “Multipass spectral broadening of 18 mJ pulses compressible from 1.3 ps to 41 fs”, Optics Letters, 43(23) 2018.

Contribution: I did the design and production of the big HR coatings.

Proceedings of refereed conferences

Martin Kaumanns, Vladimir Pervak, Dmitrii Kormin, Vyacheslav Leshchenko, Alexander Kessel, Moritz Ueffing, **Yu Chen**, and Thomas Nubbemeyer, “Multipass Spectral Broadening with Tens of Millijoule Pulse Energy”, CLEO/Europe-EQEC, Munich, 2019.

Contribution: I did the design and production of the big HR coatings.

List of Figures

2.1 Electric field of a 5 fs Gaussian pulse with different CEP. 6
2.2 Examples for different spectral phases on a Transform limited 10 fs pulse. . 9
2.3 The schematic diagram of a grating compressor. 11
2.4 The schematic diagram of a prism compressor. 12
2.5 Schematic explanation of the penetration effect and the resonance effect. . 13
2.6 Schematic of a multilayer coating. 14

3.1 Schematic of electron beam evaporation 21
3.2 Schematic diagram of magnetron sputtering 22
3.3 IBS coating plant with all important components. 24
3.4 Schematic representation of an angular distribution of sputtered particles at oblique incidence. 26
3.5 Interior view on the process chamber. 27

4.1 Layer thicknesses of double angle DMs. 32
4.2 Theoretical GDD and reflectance of double angle DMs. 32
4.3 Measured and theoretical transmittance of double angle DMs. 33
4.4 Measured and theoretical GDD of double angle DMs. 34
4.5 Layer thicknesses of HDMs. 36
4.6 Theoretical GDD and reflectance of HDMs. 36
4.7 Measured and theoretical transmittance of HDMs. 37
4.8 Measured and theoretical GDD of HMDs. 37
4.9 Measured GDD of MS-produced and IBS-produced DMs. 38

5.1 Layer thickness of the HDM. 44
5.2 Theoretical GDD and reflectance of the HDM. 44
5.3 Measured transmittance and theoretical transmittance of HDMs. 45
5.4 Measured transmittance of HDM with annealing and without annealing. . 46
5.5 Measured GDD of HDMs 47
5.6 Measured GD of HDMs. 48
5.7 Measured transmittance of HDM-1 with annealing at different time. 48
5.8 Input and output pulse simulations. 50
5.9 Layer thickness structure of the two designs. 53

5.10 GD and GDD characteristic of the one octave DM. 53
5.11 The schematic picture of the substrate holder with the desired non-uniformity. 54
5.12 Transmittance spectra of single Nb_2O_5, SiO_2 layers and a multilayer filter. 54
5.13 Comparison of measured transmittance and theoretical transmittance of the two mirrors. 55
5.14 Measured GD and GDD compared to the theoretical values. 56
5.15 Measured GDD at the designed incident angle and polarization. 57
5.16 Measured GDD at both polarizations. 57
5.17 Measured GDD at different AOI. (a) PC70-modified, (b) PC70. 58
5.18 Input and output pulse simulations. 59
5.19 Input and output pulse simulations. 59

6.1 Optical constant and fitting of Si layer 63
6.2 Optical constant and fitting of SiO_2 layer 63
6.3 Correspondence between the experimental and model reflectance. 64
6.4 Layer structure and theoretical reflectance and GD of the DM. 65
6.5 Comparison between the measured and theoretical reflectance. 66
6.6 Comparison between measured and theoretical GD and GDD. 67
6.7 Simulated input and output pulses. 67

7.1 Layer thickness structure and theoretical reflectance and GDD of the HR coating 70
7.2 The substrate holder for 300×130 mm rectangular substrate 71
7.3 The 300×130 mm rectangular HR coating compared to 1-inch sample. . . . 71
7.4 Layer thickness structure and theoretical reflectance and GDD of the CM . 72
7.5 200 mm in diameter mirror compared to 1-inch mirror in the substrate holder. 72
7.6 Comparison of the theoretical and experimental data for the CM. 73

List of Tables

4.1 Cauchy formula coefficients for the layer materials and the Suprasil substrate. 31
4.2 Cauchy formula coefficients for the layer materials and the Suprasil substrate. 34
4.3 MF values for the broadband double angle DMs and Robust HDMs. 38

5.1 Cauchy formula coefficients for the layer materials and the Suprasil substrate. 43

7.1 Cauchy formula coefficients for HfO_2 and SiO_2. 70

Chapter 1

Introduction

1.1 Motivation

Since the first laser was demonstrated by Theodore Maiman in 1960 [1], physicists have endeavored to achieve short pulses of light. The invention of mode-locking technique was a big breakthrough for the ultrashort pulse generation [2–4]. With a mode-locked continuous wave (CW) dye laser, ultrashort pulse have entered the femtosecond regime for the first time [5–7]. However, dye lasers suffered from significant disadvantages [8], such as rapid degradation during operation, limited output power and highly toxic laser medium, which made it far from ideal for ultrashort pulse generation. The discovery of Ti:sapphire laser media [9] and Kerr-lens mode-locking (KLM) [10] marked the next generation of ultrashort pulses. With these elements and optimization of the intro-cavity group delay dispersion (GDD), sub-100 fs pulses became routinely available [11–13]. However, in order to obtain even shorter few-cycle pulses, accurate dispersion control is required, which can only be fulfilled by chirped mirrors (CMs).

The first CM, which is also called dispersive mirror (DM) nowadays was invented by Robert Szipocs in 1994 [14]. The CM utilizes the wavelength-dependent penetration depth to introduce the negative GDD, which is known as the penetration effect. On the other hand, another type of Gires-Tournois interferometer (GTI) was first introduced in 1964 [15], but has not drawn much attention until the 1980s [16–18]. In the GTI structure, the negative GDD was obtained by resonant trapping of a selected wavelength in one or several thick layers, which act like cavities of a Fabry–Pérot interferometer [19]. Such effect to introduce the GDD is know as the resonance effect. With this resonance effect, a relatively large amount of GDD in a narrower band can be obtained. In the past three decades, since both CMs and GTI were applied to ultrashort lasers, DMs have developed further and further. The modern DMs [20] combing the penetration effect and the resonance effect are able to introduce larger amount of GDD and cover a wider bandwidth. Broadband dispersive mirrors [21–33] (BBDMs) and highly dispersive mirrors [30,34–46] (HDMs) have been the main research areas for DMs. BBDMs allowing for chirp compensation over more than one octave enabled few-cycle pulse generation [22–26,32,33], while HDMs introducing

highly negative dispersion were used in all kinds of ultrafast oscillators [37–40]. All in all, DMs which provide second or even higher-order dispersion compensation with high accuracy and efficiency have been the indispensable components in ultrashort lasers.

Apart from achieving ever shorter pulses, ultrashort pulses with higher intensity and repetition rate are also of great importance and interest. Such high power lasers have been the essential tools for studying laser matter interaction [47], electrons and proton acceleration [48–50] and laboratory astrophysics [51]. However, with the increasing intensity, the laser-induced damage threshold of the multilayer coating becomes the weak point and limits the achievable intensity. Two methods are available to deal with the optical breakdown of the multilayer coating. The straightforward one is to increase the beam size of the laser system. With a larger beam diameter, the power density on the coating surface will be smaller, resulting in a higher laser resistance of the coating. However, larger beam size requires larger optics. In order to produce larger optics, an appropriate coating technology must be employed. The other method is to improve the damage threshold of the coating, which could be realized in a way by modifying the design and the coating process. The formation of electric field maxima inside the coating and defects produced by the coating process are the two major reasons triggering laser induced damage. It is possible to optimize the design in order to decrease the field maxima and move the maxima into a larger band gap material. Improving the coating process is able to reduce defects in the coating. Both of these methods can improve the damage threshold.

Sputtering [21–25, 29, 30, 34–45] has long been the best technique to produce high-quality multilayer coatings. The sputtered coatings tend to be denser, having less defects and be more robust to the environment compared to the evaporated coatings, due to the higher energies involved in the formation of the layers [52]. Magnetron sputtering (MS) [21–25, 38–40, 44, 53] and ion beam sputtering (IBS) [26, 30, 41, 43, 54, 55] are the two widely-used and successful technologies for the production of multilayer DMs. Electron beam evaporation (EB) as one more method is able to evaporate large varieties of materials. However, due to its relatively lower thickness accuracy, it is mainly used to deposit mid-infrared (MIR) DMs [27, 53]. Compared to MS, IBS has the advantage of being able to manufacture large-scale and high-quality coatings, including low loss and high damage threshold coatings. With our current IBS coating plant, coatings with a diameter of up to 300 mm with the non-uniformity better than 1% can be realized [56]. Moreover, the substrate diameter could be easily increased to 600 mm with an extended version [57]. High reflective (HR) coatings with total loss as low as 3 ppm were successfully produced with our IBS plant. Based on these advantages, IBS is very suitable to make large-scale and high-quality coatings, including HR coatings and multilayer DMs for high-power lasers.

Prior to the deposition of large-scale DMs, the layer thickness accuracy of IBS must be verified good enough to deposit DMs. BBDMs and HDMs are two types of DMs, where the penetration effect and the resonance effect play a major role in introducing the GDD, respectively. These two effects are sensitive to absolute errors and relative errors, respectively. Successful production of BBDMs and HDMs has been realized by IBS. Moreover, below we show that a direct comparison between similar BBDWs and HDMMS produced by IBS and MS can be a proof of the thickness accuracy of IBS.

Since the invention of first DM [14], GDD oscillation problems have been accompanying the development of DMs. These oscillations originating from the impedance mismatching between the incident medium and the top layers limit the achievable minimum pulse duration and introduce satellites. Several methods have been proposed to suppress GDD oscillations, including various single-mirror methods, e.g., double chirped mirrors [54, 58–60], Brewster angle DMs [61, 62], Back-side coated DMs [63], tilt-front-interface DMs [64] and wedged DMs [25], and mirror-pair methods, e.g.,complementary DM pair [22, 26, 29] and double angle DM pair [24]. However, the single-mirror methods have their own limitations, which include the limited bandwidth, the complex structure and the production difficulty. The mirror-pair method is the most widely-used and effective method to provide negative dispersion with smooth GDD oscillations so far. However, the complementary DM pair has to be deposited in two coating runs and is sensitive to the deposition rate deviations, since any rate deviations between the two coating runs will lead to an imperfect match of the GDD oscillations and increase the residual GDD oscillations. This is not the case for double angle DM pair, since the double angle DM pair is produced within one coating run. However, the double angle DM pair works at two angles of incidence (AOI) , which increases the difficulty for the alignment and only works at one polarization. Two new mirror-pair methods which are applied to suppress the GDD oscillations of HDMs and BBDMs, respectively, are presented in chapter 5.

IBS has been widely-used for the production of ultraviolet, visible and near-infrared optical coatings. Further extending the IBS to the mid-infrared region will be beneficial for the advancement of MIR DMs as well as MIR lasers. The MIR fingerprint region where molecules have their distinct absorption is crucial for high-resolution spectroscopy [65, 66], trace molecular sensing [67] and chemical stand off detection [68]. As more scientists are attracted towards MIR lasers, the demand of corresponding DMs is growing. Electron beam evaporation has been the mostly used technique to deposit MIR DMs [27, 53]. However, EB does not have good thickness control and is unable to produce more complex DMs. In addition, the maximum deposited thickness is limited by the volume of the crucible. IBS, which has better thickness accuracy and is not limited by the deposited thickness is a promising option for the production of high-quality and high-accuracy MIR DMs.

1.2 Thesis outline

Chapter 2 introduces the ultrashort pulse and presents the influence of different dispersion characteristics on the ultrashort pulse as well as dispersion compensation methods, including grating compressors, prism compressors and multilayer DMs. The design process of DMs and concept of suppressing GDD oscillations are presented in detail. Chapter 3 provides the basic experimental techniques for this thesis, which include the coating plants and characterization devices. Chapter 4 introduces the comparison of MS and IBS based on BBDMs and HDMs. This chapter demonstrates the capacity of IBS to produce DMs and that IBS has a comparable accuracy of layer thicknesses to MS. Chapter 5 deals with the GDD oscillations of DMs and proposes two mirror-pair approaches to suppress GDD

oscillations of HDMs and BBDMs, respectively. Chapter 6 is devoted to extending the working region of IBS to the mid-infrared and introduces a 3 to 6 μm DM compensating the dispersion introduced by a GaAs crystal, which is the first mid-infrared DM produced with IBS. Chapter 7 presents two multilayer coatings with large substrate size, including 300×130 mm rectangular HR coatings and 200 mm in diameter chirped mirrors. This chapter demonstrates the capability of IBS to produce large-scale coatings. Chapter 8 concludes this thesis and provides an outlook on the further development of multilayer DMs with IBS.

Chapter 2

Theoretical background

In this chapter, the basic theoretical principles are presented. We start by describing the ultrashort pulses and defining the important terms in dispersive mirrors, which are group delay and group delay dispersion. Then we theoretically investigate the influence of different dispersion characteristics on temporal pulse duration and spectrograms in section 2.2. A brief introduction of dispersion compensation methods including grating compressors, prism compressors and dispersive mirrors is presented in Section 2.3. A detailed introduction on the design of dispersive mirrors and suppressing group delay dispersion oscillations, which are the key processes of developing dispersive mirrors, are discussed in detail in section 2.3.3.

2.1 Description of ultrashort pulses

The time-dependent electric field of a linearly polarized ultrashort pulse at a fixed position in space can be described as [69, 70]:

$$E\left(t\right) = A\left(t\right)e^{i\left(\omega_0 t + \phi_0 + \phi_a(t)\right)} = A\left(t\right)e^{i\phi(t)} \tag{2.1}$$

where $A(t)$ is the temporal amplitude or envelope function, ω_0 is the angular frequency, ϕ_0 is the carrier envelope phase (CEP) and $\phi_a\left(t\right)$ is the time dependent phase function. The total temporal phase $\phi\left(t\right)$ contains frequency-vs.-time information, and the instantaneous light frequency is the first derivative of temporal phase $\phi\left(t\right)$ with respect to time t and defined as:

$$\omega\left(t\right) = \frac{d\phi\left(t\right)}{dt} = \omega_0 + \frac{d\phi_a\left(t\right)}{dt} \tag{2.2}$$

This time dependent phase function $\phi_a\left(t\right)$ describes variations of the frequency in time, called a chirp. If $\frac{d\phi_a(t)}{dt}$ is >0, it is called up-chip, while it is called down-chip if $\frac{d\phi_a(t)}{dt}$ is <0. For $\frac{d\phi_a(t)}{dt}$ equals 0, there is no chirp and it is called Fourier transform limited pulse or bandwidth limited pulse.

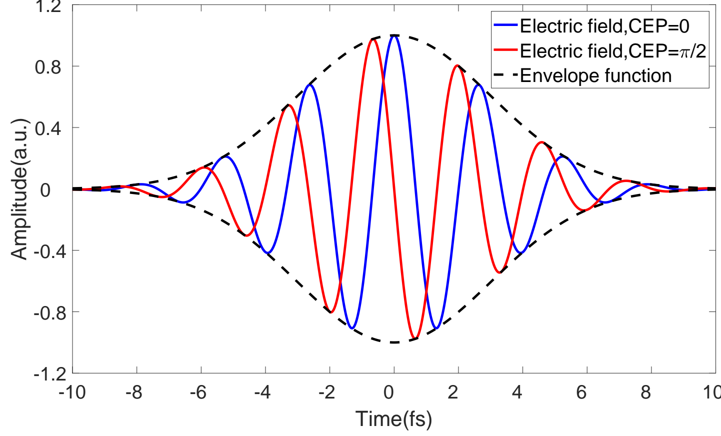

Figure 2.1: Electric field of a 5 fs Gaussian pulse with different CEP.

For a Fourier transform limited Gaussian pulse, the electric field can be defined as [69]:

$$E\left(t\right)=e^{-2\ln 2\frac{t^2}{\tau^2}}e^{i(\omega_0 t+\phi_0)} \tag{2.3}$$

where τ is the temporal pulse duration defined by the full width at half maximum (FWHM) of the temporal intensity. Figure 2.1 displays the electric field $E(t)$ for a Gaussian pulse with CEP of 0 and $\frac{1}{2}\pi$, a pulse duration of 5 fs (1 fs=1×10^{-15} s) and an angular frequency of 2.35 rad/fs corresponding to a wavelength of 800 nm.

However, a direct manipulation of the temporal phase cannot be achieved by any electronic device. It is better to switch from time domain to frequency domain, when describing an optical pulse and dealing with the dispersion. This can be simply done with Fourier theory. The complex electric field and the complex spectrum are linked by the Fourier transform:

$$E\left(\omega\right)=\int_{-\infty}^{+\infty}E\left(t\right)e^{-i\omega t}dt \tag{2.4}$$

$$E\left(t\right)=\frac{1}{2\pi}\int_{-\infty}^{+\infty}E\left(\omega\right)e^{i\omega t}d\omega \tag{2.5}$$

where $E\left(\omega\right)$ is the complex spectrum in the frequency domain, which can be represented by amplitude and phase term:

$$E\left(\omega\right)=\sqrt{S\left(\omega\right)}e^{i\varphi(\omega)} \tag{2.6}$$

where $S\left(\omega\right)$ is the spectral amplitude and $\varphi\left(\omega\right)$ is the spectral phase. The spectral phase is of great importance when studying the propagation and dispersion compensation of the optical pulse. It plays an important role obtaining the pulse duration. The spectral phase is usually expanded in a Taylor series around ω_0:

$$\varphi\left(\omega\right)=\sum_{j=0}^{\infty}\frac{\varphi^j\left(\omega_0\right)}{j!}\left(\omega-\omega_0\right)=\varphi\left(\omega_0\right)+\frac{d\varphi}{d\omega}\left(\omega-\omega_o\right)+\frac{1}{2}\frac{d^2\varphi}{d\omega^2}\left(\omega-\omega_0\right)^2+\ldots \tag{2.7}$$

The first three terms in the Taylor expansion are of great importance. The zero order describes the absolute phase corresponding to the CEP in the time domain. The first order term is also known as group delay (GD), which is just related to the shift of the temporal envelope and defined as:

$$GD = \frac{d\varphi}{d\omega} = -\frac{d\varphi}{d\lambda}\frac{\lambda^2}{2\pi c} \tag{2.8}$$

Second and higher order terms are responsible for changes in the temporal structure of the electric field. The second order term is the group delay dispersion (GDD), which causes the temporal linear chirp and plays the dominant role in obtaining the pulse duration. It is defined as:

$$GDD = \frac{d^2\varphi}{d\omega^2} = \frac{dGD}{d\omega} = -\frac{dGD}{d\lambda}\frac{\lambda^2}{2\pi c} \tag{2.9}$$

In addition, third and higher order terms can affect the pulse shape and introduce the satellite pulses. These effects become more severe as the bandwidth increases.

2.2 Influence of different dispersion characteristics on ultrashort pulses

When a laser pulse propagates in a dielectric medium, the spectral phase will be affected by the dispersion, which is the wavelength dependent refractive index. For many materials the well-known Sellmeier equation [71] is used to describe the refractive index:

$$n^2(\lambda) = 1 + \sum_i \frac{A_i\lambda^2}{\lambda^2 - B_i} \tag{2.10}$$

where A_i and B_i are the Sellmeier coefficients, λ is specified in micrometer. The accumulated phase propagating through a material with the thickness of L is given by:

$$\varphi_m(\omega) = k(\omega)L = \frac{\omega n(\omega)}{c}L \tag{2.11}$$

where $k(\omega)$ is the angular frequency dependent wavenumber. The GDD of a dispersive medium which is the second derivative of $\varphi_m(\omega)$ to the angular frequency can be converted to the wavelength unit and defined as:

$$GDD = \frac{d^2\varphi_m}{d\omega^2} = \frac{d^2\frac{\omega n(\omega)}{c}L}{d\omega^2} = \frac{\lambda^3 L}{2\pi c^2}\frac{d^2 n}{d\lambda^2} \tag{2.12}$$

Group velocity delay (GVD) is the second derivate of $k(\omega)$ with respect to ω and commonly used to describe the material dispersion, which can be simply linked with GDD by:

$$GDD = GVD \times L \tag{2.13}$$

When a pulse passes through a dispersive material, the spectral phase $\varphi_m(\omega)$ will cause changes in the pulse shape and pulse duration. Mathematically studying the impact of the material dispersion on the pulse shape can be done by calculating the accumulated spectral phase $\varphi_m(\omega)$ from the material and multiplying the spectral phase of the laser pulse by $e^{i\varphi(\omega)}$. In addition to the phase accumulation, the frequency dependent transmission of the material, $T(\omega)$, should be also taken into account. Then temporal electric field can be obtained by inverse Fourier transforming the new complex spectrum. The whole process is illustrated as below:

$$E(t) \overset{FT}{\rightarrow} E(\omega) = A(\omega)\, e^{i\varphi(\omega)} \overset{material}{\rightarrow} E'(\omega) = A(\omega) \times T(\omega)\, e^{i(\varphi(\omega)+\varphi_m(\omega))} \overset{IFT}{\rightarrow} E'(t) \tag{2.14}$$

Besides the temporal and spatial representation of the ultrashort pulse, time-frequency distributions for instance the spectrogram [72, 73] are more intuitive to show the time-frequency couplings and the influence of material dispersion on the pulse, which is defined as:

$$S(t,\omega) = \left| \int E\left(t'\right) g\left(t' - t\right) e^{-i\omega t'} dt' \right|^2 \tag{2.15}$$

where $E(t)$ is the electric field of an input pulse and $g(t)$ is the electric field of a gate pulse. The spectrogram is the time convolution of the electric field with a gate $g(t)$ that can be the pulse itself. It is widely-used in the characterization of ultrashort pulses, especially in the frequency-resolved optical gating (FROG) technique [74]. Depending on the instantaneous nonlinear optical effect in FROG, the gate function can be different.

The influence of different spectral phase characteristics on the temporal pulse and the spectrogram for a transform limited Gaussian pulse with a pulse duration of 10 fs is illustrated in Figure 2.2. The gate pulse in equation 2.15 is considered as the 10 fs pulse itself.

Figure 2.2 (b) shows clearly that the linear spectral phase, namely non-zero constant GD and zero GDD, just leads to the shift of the pulse and the spectrogram does not change at all except the shift. In figure 2.2 (c), one can see that the quadratic phase with 100 fs^2 GDD causes the broadening of the pulse, and in the spectrogram it is even more intuitive to see the broadening. Figure 2.2 (d) shows the cubic phase with 900 fs^3 third-order dispersion (TOD) introducing the post-pulses after the main pulse. The larger the TOD, the higher the side pulses and the less meaningful the FWHM pulse duration. Figure 2.2 (e-g) display the influence of different GDD characteristics on the pulse, which include different amount of GDD oscillations and different frequency of GDD oscillations. As we can see, the larger the GDD oscillations, the bigger the pre-and post-pulses and the lower the peak intensity. On the other hand, faster GDD oscillations lead to smaller pre-and post-pulses and higher peak intensity. The side pulses can be clearly seen from the spectrograms. Moreover, the side pulses are separated farther from the main pulse for faster GDD oscillations. The GDD oscillations are mainly introduced by multilayer DMs, which is inevitable due to the special property of DMs, which is the impendence mismatch between the incident medium and the front layers. These GDD oscillations significantly change the pulse shape, resulting in the appearance of satellites and the energy drop of the

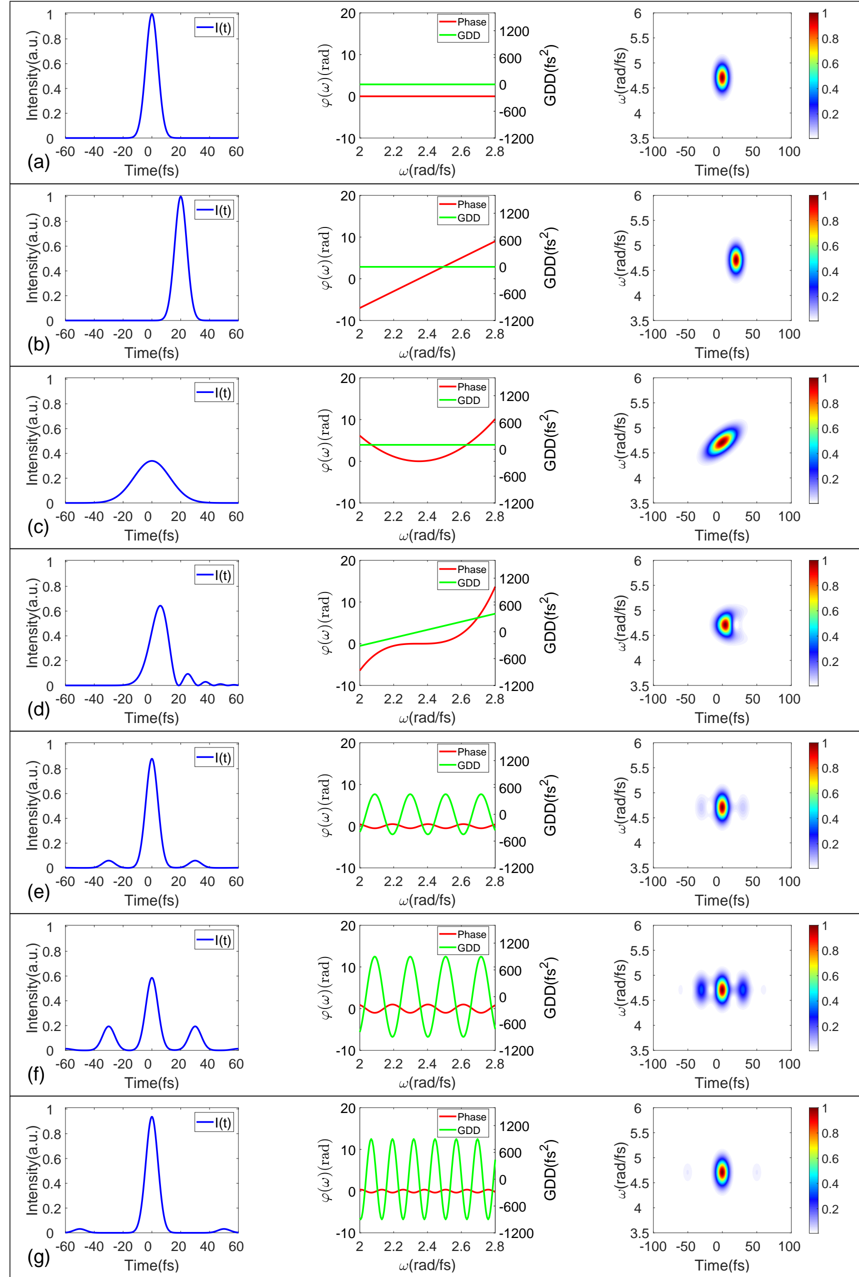

Figure 2.2: Examples for different spectral phases on a Transform limited 10 fs pulse. The first, second and last columns represent the temporal intensity, the spectral phase and GDD and the spectrogram. (a) A Transform limited pulse with zero phase (b) Linear phase with GD=20 fs, (c) Quadratic phase with GDD=100 fs^2, (d) Cubic phase with TOD=900 fs^3, (e)-(g) Demonstrate the influence of different GDD oscillations on the pulse. (e) GDD oscillation ±450 fs^2 and low oscillation frequency, (f) GDD oscillation ±900 fs^2 and low oscillation frequency, (g) GDD oscillation ±900 fs^2 and fast oscillation frequency.

main pulse, and are detrimental to the laser pulse, especially to the few-cycle ultrashort pulse. The GDD oscillations could be highly suppressed by the special DM structure or DM pair. Two new methods which are able to suppress such oscillations are presented in chapter 5.

2.3 Dispersion compensation for ultrashort pulses

As discussed in the last section, an ultrashort pulse will undergo a temporal broadening when passing through a medium due to the accumulated spectral phase which is mainly the GDD. In a laser system, the gain medium, optical elements and even air could introduce the positive dispersion. Therefore, optical setups which provide the opposite dispersion to compress the pulse back to the Fourier transform limited value are needed. There are several compression techniques available, including grating compressors, prism compressors and multilayer DMs. Among them, grating and prism compressors are based on the angular dispersion to manipulate the optical path for each wavelength. For example, negative dispersion can be realized by letting the red component travel a longer optical path than the blue component. The other way is multilayer DMs, which use the interference effect inside the structure including the penetration effect and the resonance effect to provide the negative dispersion. In this section, brief introductions of grating and prism compressors are presented, the emphasis of this section focuses on multilayer DMs.

2.3.1 Grating compressors

Two parallel gratings used to introduce a negative dispersion were first proposed by Treacy in 1969 [75]. Grating compressor consists of two identical parallel gratings in a double-pass configuration, as shown in Figure 2.3. The first grating disperses the laser pulse into separated spectral components. The second grating re-collimates the beam. The collimated beam then is reflected back by a high reflective (HR) mirror that inverts the beam. In this kind of setup, the red spectral components experience a longer optical path than the blue spectral components. Such an arrangement is able to introduce the negative dispersion and is suitable to compensate for material dispersion. The GDD introduced by a double pass grating compressor shown in Figure 2.3 can be defined as:

$$\frac{d^2\varphi_g}{d\omega^2} = -\frac{\lambda^3}{\pi c^2 d^2}\frac{L}{\cos\left[\theta\left(\lambda\right)\right]^3} \tag{2.16}$$

where d is the grating period, L is the distance between the two gratings and $\theta\left(\lambda\right)$ is the diffraction angle, which is given by

$$\theta\left(\lambda\right) = \cos^{-1}\sqrt{1-\left(\frac{\lambda}{d}-\sin\left(\gamma\right)\right)^2} \tag{2.17}$$

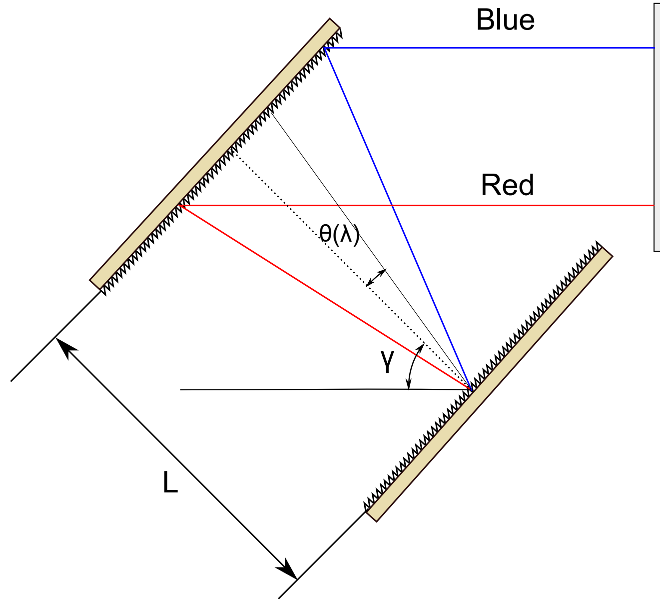

Figure 2.3: The schematic diagram of a grating compressor.

As we can see from equation 2.16, the smaller the grating spacing d and the larger the distance L, the larger the negative GDD. A grating compressor has the advantage of being able to introduce a large amount of negative dispersion. As a result, it has been used as the stretcher and compressor in the chirped pulse amplification (CPA) invented by Donna Strickland and Gerard Mourou [75], who were awarded the Nobel Prize in Physics in 2018. However, the grating compressor also suffers from high losses, a relatively narrow bandwidth and higher-order dispersion.

2.3.2 Prism compressors

The use of prism pairs for dispersion compensation was first introduced in the 1980s [76, 77]. Prism compressors provide the negative GDD in a similar manner to the grating compressors. Negative GDD is obtained by the angular dispersion of the first prism, where the second prism re-collimates the beam. Recovering the original beam can be accomplished by a HR mirror, which is illustrated in Figure 2.4. The total dispersion introduced by a pair of prisms is composed of the negative angular dispersion and the dispersion of the prism material. For a double pass prism compressor as shown in Figure 2.4, the GDD is approximated to be:

$$\frac{d^2\varphi_p}{d\omega^2} \approx \frac{d^2\varphi_A}{d\omega^2} + \frac{d^2\varphi_m}{d\omega^2} = -\frac{4L_s\lambda^3}{\pi c^2}\left(\frac{dn}{d\lambda}\right)^2 + \frac{L_p\lambda^3}{2\pi c^2}\frac{d^2n}{d\lambda^2} \tag{2.18}$$

where φ_A and φ_m are the phase from angular dispersion and prism material, respectively, L_s and L_p are the prism separation and the path through each prism. The dispersion is adjustable by translating any prism perpendicular to the beam path to add or decrease

glass without misaligning the beam. Moreover, the negative GDD can be increased by increasing the distance between two prisms. However, a prism distance exceeding 1m is often impractical. Furthermore, the higher third-order dispersion introduced by the prism compressor prevents the generation of sub-10 fs ultrashort pulses.

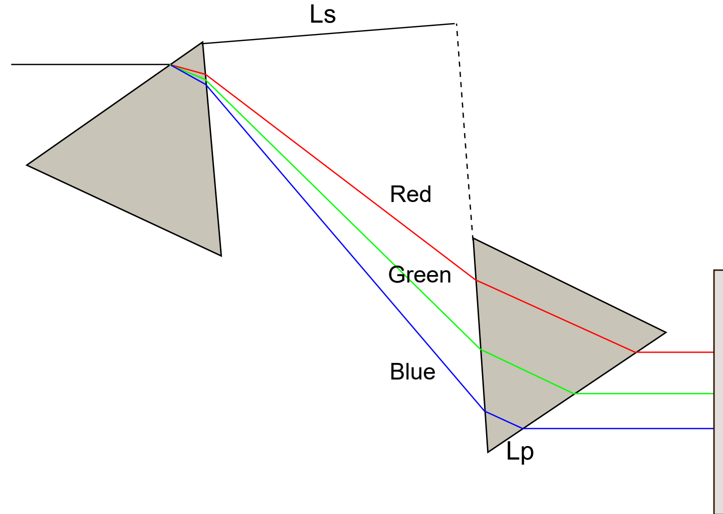

Figure 2.4: The schematic diagram of a prism compressor.

2.3.3 Multilayer dispersive mirrors

DMs are composed of dozens of aperiodic alternating high and low refractive index materials. The dispersion introduced by DMs can be fully controlled by such layer structure. The dispersion is obtained by the so-called penetration effect and the resonance effect, which are illustrated in Figure 2.5. The penetration effect is the wavelength-dependent penetration depth, for example the red light penetrates and reflects deeper in the layer structure than blue light, resulting in the negative dispersion, while the resonance effect means that certain frequencies of light are trapped and oscillating in the cavities, which acts like a Fabry–Perot interferometer in the multilayer structure. Therefore, large amounts of group delay dispersion can be introduced at the selected frequency.

In this section, the theoretical approach for optimizing multilayer DMs and the concept of suppressing GDD oscillations are presented.

2.3.3.1 Design process of multilayer dispersive mirrors

Designing a multilayer coating is a process to determine the thickness of each layer and the total number of layers. Prior to designing the coating, the refractive indexes of the selected materials should be known. Then the theoretical calculations of reflectance, transmittance, spectral phase and other characteristics of a multilayer coating can be performed.

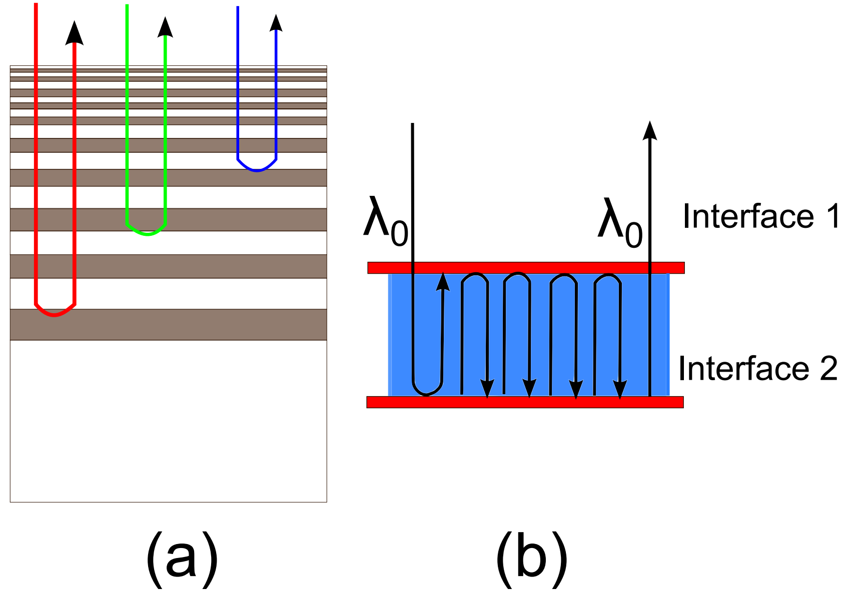

Figure 2.5: Schematic explanation of the penetration effect and the resonance effect. (a) the penetration effect, the optical thickness of the DMs increases gradually from the top layer to the bottom layer, which causes longer wavelengths to reflect at deeper positions than the short wavelengths and introduces the negative dispersion. (b) the resonance effect, when the optical thickness of the layer is close to the half of the wavelength, it will act like a Fabry–Pérot interferometer. A certain frequency of light will be trapped and oscillating in the cavity, which introduces the negative dispersion.

The multilayer coating is usually regarded as a number of boundaries between various homogeneous media and it is the effect that boundaries have on an incident wave which we wish to calculate. A single boundary is the simplest and most basic case.

The optical admittance η of the medium is defined as [78]:

$$\eta = \frac{N}{c\mu} = N\sqrt{\frac{\varepsilon_0}{\mu_0}} = NY \tag{2.19}$$

The optical admittance at oblique angle can be given by:

$$\eta_s = NY\cos(\theta) \tag{2.20}$$

$$\eta_p = \frac{NY}{\cos(\theta)} \tag{2.21}$$

where N is the complex refractive index, Y is the optical admittance in free space which equals to 2.6544×10^{-3} s and θ is the angle of incidence.

For a single boundary, the amplitude of reflection and transmission coefficients are written as:

$$\rho = \frac{\eta_0 - \eta_1}{\eta_0 + \eta_1} \tag{2.22}$$

$$\tau = \frac{2\eta_0}{\eta_0 + \eta_1} \tag{2.23}$$

The corresponding reflectance and transmittance are given by:

$$R = \left(\frac{\eta_0 - \eta_1}{\eta_0 + \eta_1}\right)\left(\frac{\eta_0 - \eta_1}{\eta_0 + \eta_1}\right)^* \tag{2.24}$$

$$T = \frac{4\eta_0 Re\left(\eta_1\right)}{\left(\eta_0 + \eta_1\right)\left(\eta_0 + \eta_1\right)^*} \tag{2.25}$$

where η_0 and η_1 are the optical admittance of incident and exit medium and $*$ denotes the complex conjugate.

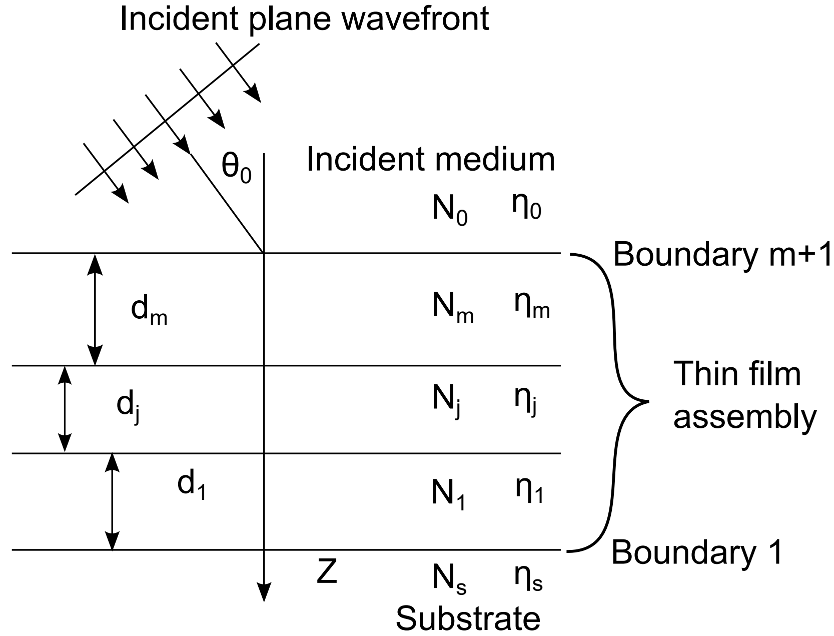

Figure 2.6: Schematic of a multilayer coating. A plane wave is incident on a multilayer coating with AOI of θ_0. The multilayer consists of m layers. The symbol d, N and η represent the thickness, refractive index and optical admittance, respectively. The layer number and boundary start from the substrate.

A multilayer composed of a number of boundaries between various thicknesses of thin films is schematically shown in Figure 2.6. Each layer can be regarded as a 2×2 matrix which is known as the characteristic matrix of the thin film. The combination of the first layer and substrate can be linked with the characteristic matrix [78]:

$$\begin{bmatrix} E_1 \\ H_1 \end{bmatrix} = \begin{bmatrix} \cos\delta_1 & \left(\frac{i\sin\delta_1}{\eta_1}\right) \\ i\eta_1\sin\delta_1 & \cos\delta_1 \end{bmatrix} \begin{bmatrix} E_s \\ H_s \end{bmatrix} \tag{2.26}$$

if we divide E_s on both sides of the equation, it will be more intuitive to see the connection between the first layer and the substrate.

$$\begin{bmatrix} E_1/E_s \\ H_1/E_s \end{bmatrix} = \begin{bmatrix} B \\ C \end{bmatrix} = \begin{bmatrix} \cos\delta_1 & \left(\frac{i\sin\delta_1}{\eta_1}\right) \\ i\eta_1\sin\delta_1 & \cos\delta_1 \end{bmatrix} \begin{bmatrix} 1 \\ \eta_s \end{bmatrix} \tag{2.27}$$

The optical admittance of the new assembly can be written as:

$$Y = \frac{H_1}{E_1} = \frac{C}{B} = \frac{\eta_s\cos\delta_1 + i\eta_1\sin\delta_1}{\cos\delta_1 + (i\eta_s/\eta_1\sin\delta_1)} \tag{2.28}$$

where $\delta_1 = \frac{2\pi}{\lambda}N_1 d_1\cos\theta_1$ is the first layer phase thickness with the angle of refraction θ_1, the refractive index N_1 and the thickness d_1, η_1 and η_s are the optical admittance of the first layer and the substrate. This result can be immediately extended to the general case of an assembly of m layers, when the characteristic matrix is simply the product of the individual matrices taken in the correct order.

$$\begin{bmatrix} B \\ C \end{bmatrix} = \left\{ \prod_{j=m}^{1} \begin{bmatrix} \cos\delta_j & (i\sin\delta_j/\eta_j) \\ i\eta_j\sin\delta_j & \cos\delta_j \end{bmatrix} \right\} \begin{bmatrix} 1 \\ \eta_s \end{bmatrix} \tag{2.29}$$

where δ_j and η_j are the phase thickness and optical admittance in the j-th layer. Y equals to C/B. Based on the characteristic matrix method [78], the formulas for calculating characteristics of a multilayer coating are given as follows:

$$R = \left(\frac{\eta_0 B - C}{\eta_0 B + C}\right)\left(\frac{\eta_0 B - C}{\eta_0 B + C}\right)^* \tag{2.30}$$

$$T = \frac{4\eta_0 Re\,(\eta_s)}{(\eta_0 B + C)\,(\eta_0 B + C)^*} \tag{2.31}$$

The phase change on the reflection can be written as:

$$\varphi_r = \tan^{-1}\left(\frac{Im\,[\eta_s\,(BC^* - CB^*)]}{(\eta_s^2 BB^* - CC^*)}\right) \tag{2.32}$$

The phase change on transmission is defined as:

$$\varphi_t = \tan^{-1}\left[\frac{-Im\,(\eta_0 B + C)}{Re\,(\eta_0 B + C)}\right] \tag{2.33}$$

The GD and GDD which are the first and second derivative of phase with angular frequency are given by:

$$GD = \frac{d\varphi}{d\omega} \tag{2.34}$$

$$GDD = \frac{d^2\varphi}{d\omega^2} \tag{2.35}$$

Making a coating design with desired spectral properties is an inverse process to determine the number of layers m and the thickness of each layer d_i for $i = 1, \ldots, m$, which are called the design parameters. These design parameters which include a set of physical layer thickness can be described by a vector X:

$$X = \{d_1, d_2, d_3, \ldots, d_m\} \tag{2.36}$$

In order to obtain design parameters, a target with required spectral properties as a function of wavelength and a merit function are needed. The target can be reflectance, transmittance, GD and GDD, which depend on the required characteristic of the coating. The wavelength which the target covers is treated as a discrete set of L points,$\lambda_1, \lambda_2, \lambda_3, \ldots, \lambda_L$. The most common targets for a DM are reflectance and GDD, which can be represented as $R(\lambda_j)$ and $GDD(\lambda_j)$. The merit function is used to estimate the discrepancies between the resultant and the target characteristics and can be described as [79, 80]:

$$MF(X)^2 = \frac{1}{L}\sum_{j=1}^{L}\left\{\left[\frac{R(X, \lambda_j - R(\lambda_j))}{\Delta R_j}\right]^2 + \left[\frac{GDD(X, \lambda_j - GDD(\lambda_j))}{\Delta GDD_j}\right]^2\right\} \tag{2.37}$$

where $R(X, \lambda_j)$ and $GDD(X, \lambda_j)$ are the theoretical reflectance and GDD for the physical thickness vector X and wavelength λ_j, ΔR_j and ΔGDD_j are the corresponding tolerances at each wavelength. By introducing the merit function, the design problem has turned to be a mathematical optimization problem. Optimization algorithms evaluates gradient of the merit function in order to arrive at a local minimum of the function. However, the merit function can have several local minimums, and it is required a human operator to decide, which specific minimum is appropriate. Moreover, the tolerances of reflectance and GDD have to be balanced to fit both target characteristics. It should also be pointed out that an optimal design is not the one with the lowest merit function but a compromise between the merit function and the design structure. The commercial Optilayer software [81] with the state-of-the-art needle [82] and gradual evolution algorithms [83] was used to design all the multilayer DMs presented in this thesis.

2.3.3.2 Concept of suppressing GDD oscillations

The interface mismatch between the incident medium and the top layer of DMs causes the undesirable GDD oscillations. In addition, the GDD oscillations will be enhanced by the interference effect between the light strongly reflected from the back section of the DMs and slightly reflected in the front section [58]. The interference effect becomes larger as the bandwidth of the DMs increases. The amplitude of GDD oscillations can be approximately proportional to the bandwidth.

Several approaches have been developed to suppress GDD oscillations, which can be divided into two groups. One group is known as the single-mirror method, which focuses on decreasing the effect of the interface mismatch by suppressing the reflection from the top layer. It includes double chirped mirrors [54, 58], Brewster angle DMs [61, 62], Back-side coated DMs [63], tilt-front-interface DMs [64] and wedged DMs [25]. These methods are

very effective to suppress GDD oscillations, however, they are limited by the achievable bandwidth and the complex structure. The other group is the so-called mirror-pair method. This method is not aiming at reducing GDD oscillations of the single mirror, while it utilizes two mirrors which have antiphase GDD to suppress and cancel GDD oscillations. It includes the complementary DM pair [22, 26, 29] and the double angle DM pair [24]. The complementary DM pair consists of two different mirrors which have different designs and is produced in two coating runs, while the double angle DM pair is composed of two identical mirrors working at two AOI and is produced in one coating run. The complementary DM pair is more sensitive to the deposition rate deviations, since any deviations in the rates will lead to an imperfect match of the GDD oscillations and significantly increase the residual GDD oscillations. This is not a problem for the double angle DM pair, due to the fact that all the mirrors are produced in one coating run. However, the double angle DM pair works at two AOI which increase the difficulty for mirrors alignment and are very sensitive to the polarization. Theoretically, the complementary DM pair is able to provide lower GDD oscillations and cover wider bandwidths than the double angle DM pair without considering the production errors. The mirror-pair method is still the most effective and widely-used method to suppress GDD oscillations in broadband ranges so far. Two new mirror-pair approaches will be presented in chapter 5.

Chapter 3

Experimental techniques

Optical coatings are the most basic components in laser systems. The most common technique to produce these optical coatings is the physical vapor deposition (PVD), where the material condenses on the substrates directly from vapor to solid phase. Among these PVD processes, evaporation as a simple, high-deposition-rate and low-cost process has been the principal process to deposit optical coatings, including high reflective mirrors, anti-reflective mirrors and thin film filters. Moreover, a large variety of materials can be deposited by evaporation. However, it possesses major shortcomings in respect of microstructure and low deposition accuracy. For high performance special coatings, sputtering processes, which deposit sputtered target atoms or molecules on the substrates with significantly higher energies than those of thermal evaporation, have been adopted. With such high energies, the deposited film tends to be denser and has fewer defects, as well as being more robust to the environment. At the same time, the deposition rates are more stable, which makes it the most successful and widely-used technique to produce the complex dispersive mirrors. In this chapter, three different coating processes available for this research are presented in section 3.1, which include electron beam evaporation, magnetron sputtering and ion beam sputtering. Among them, ion beam sputtering is the main workhorse to deposit multilayer dispersive mirrors in this work, which are described in detail. Once the dispersive mirrors are fabricated, they need to be characterized to inspect their properties such as transmittance, loss and GDD. The necessary characterization devices used in this work are shown in section 3.2.

3.1 Coating process

3.1.1 Electron beam evaporation

In evaporation processes, the vapor is generated simply by heating the material, known as the evaporant. The vapor then travels in straight lines from the vapor source to the substrate and condenses as a solid film on it. The variation in the thickness of film is principally dependant on the position and orientation of the substrate with respect to the

vapor source. Evaporating the material can be realized by proper crucibles or commonly-known as boats with an electric current passing through it. Such boats have low resistance and several hundred amps at low voltages can be generated to heat the material up to the evaporation point. However, manufacturing the boats with appropriate materials is very tricky, since some materials react with the boats, which contaminates the deposited films. Another form of heating which avoids many of the difficulties associated with directly and indirectly heated boats is the electron-beam heating, which is the preferred technique for most materials so far. The electrons are emitted by a hot filament by applying a high voltage. The electron beam is bent around through a semicircle by a magnetic field and focused on the material in the boat. Then the material will be evaporated by the electron beam. The electron beam source is particularly useful for materials that react with boats and require very high evaporation temperatures. Furthermore, with the electron beam source, multiple pockets in the crucible can be constructed so that more kinds of materials can be deposited in one coating cycle.

The SyrusPro 710 from Leybold Optics (Bühler Alzenau GmbH, Germany) is employed in our group, which is schematically shown in Figure 3.1. It is equipped with two electron guns and one thermal evaporator. The thermal evaporator can be replaced with a plasma source. As a result, more compact and denser films can be deposited with the plasma ion assisted deposition process. Two infrared heaters are installed below the substrates, which can heat the substrates up to 300℃. The temperature of the substrate plays a big role in determining the properties of the films. For example, metals and ultraviolet reflective coatings usually need to be deposited at room temperature to avoid the scattering issue. However, some oxides, fluorides as well as infrared materials need to be produced at a higher temperature, often 200-300℃. On the other hand, optimal mechanical properties demand deposition at a temperature that is different from that for optimum optical properties and a compromise that depends on the particular application is necessary.

The SyrusPro 710 is equipped with a quartz-crystal monitoring system. The quartz crystal is built close to the substrates with a geometry of a flat disc. The principle of quartz-crystal monitoring is to expose the crystal to the evaporant stream and to measure the variation in the frequency as the film deposits on its surface and changes the total mass. The resonant frequency of a uncoated crystal is about 5.9 MHz and is permanently measured with an accuracy of 0.3 Hz. The deposited thickness of films on the crystal is calculated from the change in frequency. The quartz-crystal monitoring is almost suitable for all kinds of materials, whether it is dielectric or metal and is independent of optical properties of the materials. However, it also posses some disadvantages. The sensitivity of the crystal decreases with the increasing build up of the mass and the amount of materials. In addition, the accuracy of the thickness control is relatively low and not satisfactory for monitoring UV and visible dispersive mirrors. For mid-infrared dispersive mirrors, due to its lower sensitivity to thickness errors, quartz crystals monitoring is employed [27, 53].

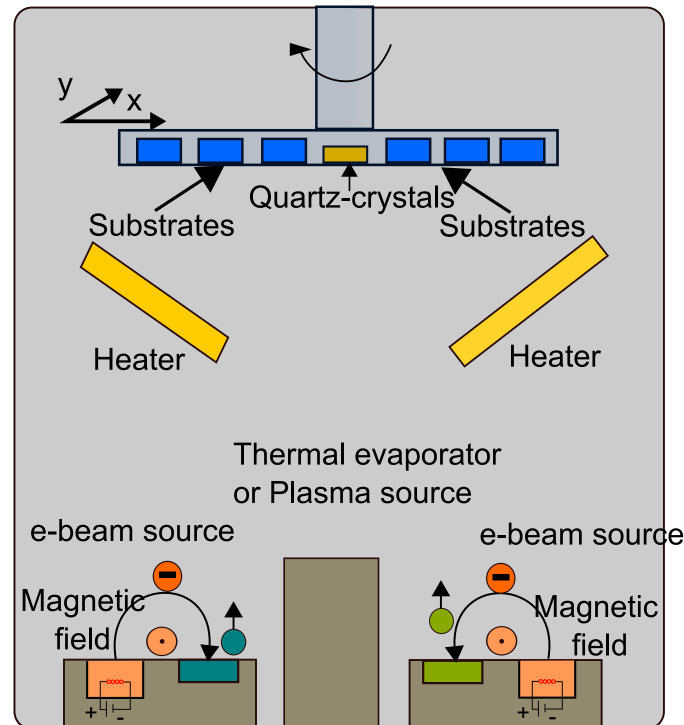

Figure 3.1: Schematic of thermal evaporation (SyrusPro 710). The SyrusPro plant is equipped with two electron beam sources. A thermal evaporator is available, which can be replaced with a plasma source. The substrates are installed in the fixtures on top of the coating chamber and the coating surface is downward. The quartz-crystals are installed near the substrates to monitor the thickness. Two infrared heaters are used to heat up the substrates.

3.1.2 Magnetron sputtering

Magnetron sputtering is one of the energetic processes, which involves greater energies than thermal evaporation. In the magnetron sputtering process, the vapor is generated by bombarding a target with energetic electrons and ions in order to eject the atoms and molecules from the target. The kinetic energy and momentum of the ejected particles are so high that the growing film is subjected to a much greater impulse each time a fresh particle arrives, which disrupts the void and columnar structure and forms much denser and more solid films. A magnetic field introduced by the permanent magnets behind the targets confines the electrons near the surface of the target, which not only leads to a higher density plasma and increased deposition rates, but also prevents damage which would be caused by direct impact of these electrons with the substrate or the growing film. In the conventional form of magnetron sputtering, namely the direct current (DC) magnetron sputtering, the target is metallic and used as an electrode. In order to deposit oxides or nitrides, the sputtering gas is usually a mixture of a noble gas with a process

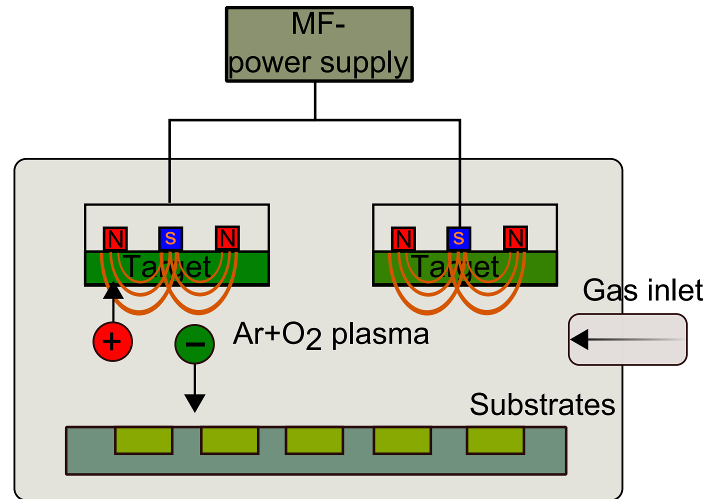

Figure 3.2: Schematic diagram of magnetron sputtering (Helios). Helios plant is equipped with dual magnetrons and a plasma source for reactive sputtering.

gas such as argon and oxygen or nitrogen. This reactive gas reacts also with the target to produce a skin of oxide or nitride and the skin tends to build up in the less eroded regions, which is called target poisoning. This problem can be solved by twin magnetron targets that are connected to opposite poles of a mid-frequency power supply so that each is alternately anode and cathode. Radio-frequency (RF) magnetron sputtering as another form of magnetron sputtering does not require the target to be a metal and avoids the problems of an insulating target. Therefore, any material can be deposited using RF magnetron sputtering theoretically.

The Helios magnetron sputtering plant developed by Leybold Optics (Bühler Alzenau GmbH, Germany) was employed in this work. Figure 3.2 shows the basic mechanism of the magnetron sputtering. It is equipped with two proprietary TwinMags magnetrons and a plasma source for plasma-ion assisted reactive middle-frequency dual-magnetron sputtering. The commonly-used oxides can be produced in a reactive middle-frequency dual-magnetron sputtering mode. In this mode, the deposition rates can be as high as 0.4 nm/s, allowing for rapid manufacturing as well as the production of extremely dense, smooth and amorphous layers with high reproducibility. The Helios machine covers the spectral range from 250 to 4000 nm and substrates with diameters up to 100 mm are suitable for coating. Due to the stable deposition rate of the Helios plant, time control is used to monitor the thickness. Moreover, it is also equipped with a broadband optical monitoring (BBOM), which covers the range from 420 to 1000 nm. The BBOM is employed in a passive mode and presents the in-situ transmittance. The deposition time can be calibrated with the BBOM results.

3.1.3 Ion beam sputtering

Ion beam sputtering (IBS) is another form of sputtering. The biggest advantage of IBS over the other sputtering processes is that ion generation and acceleration, generation of film particle and thin film growth are spatially separated. It avoids the interaction of plasma, target and substrate, which is very helpful for the production of fewer defects and higher purity coatings. In addition, such separation offers a higher degrees of freedom in adjusting the coating parameters.

In this work, the IBS coating plant made by Cutting-Edge-Coating company was employed. The basic principle of the process is illustrated schematically in Figure 3.3. Within the coating chamber, a cryopump [84] located at the bottom is employed to maintain the high vacuum. The basic pressure can reach 1×10^{-7} mbar. Ions are generated by the radio frequency (RF) [85] radiation in an isolated quartz vessel with noble gas, which can be Argon or Xenon or even the combination of a noble gas and oxygen. Then they are accelerated and extracted by a three-grid system. Negative electrons generated by a RF neutralizer are utilized to neutralize the positively charged ions. The ion beam is shining on the target, which is mounted on a zone-target assembly. In principle, with such an assembly, four different materials could be coated in one coating process. In addition, the so-called rugate-filter [86] can be produced with the co-sputtering of two targets. The rugate-filter design [87,88] is a good option to increase the laser induced damage threshold of optical coatings. The targets are made of pure metal or semiconductor. In order to deposit oxides, additional oxygen is ejected near the target. The incident angle on the target influences the sputtering yield and energy distribution of sputtered particles. As a result, the deposition rates and non-uniformity are related to the ion incident angle. The atoms and molecules sputtered from the target are directly condensed on the substrates above the target with a tilted angle instead of directly above the target. Two infrared quartz heaters are equipped to heat the substrates. An assistant ion source is integrated in the coating chamber, which directly irradiates to the substrates and transfers the energy from to the charged ions to the film, supporting the formation of dense layers. The assistant source can be also used to clean or etch the substrates.

3.1.3.1 Layer thickness control technique

The IBS coating plant is equipped with a broadband optical monitoring system (BBOM) [89, 90], which mainly includes a combined deuterium and halogen lamp, a spectrometer with a silicon based back-thinned charge-coupled device (CCD) and the corresponding BBOM software. In order to record the transmission, three positions must be triggered, which are dark, reference and sample, respectively. During every revolution of the substrate holder, three independent spectra are taken to calculate the transmission spectra of the sample by the equation:

$$T(\lambda) = \left(I_{sample}(\lambda) - I_{dark}(\lambda)\right) / \left(I_{reference}(\lambda) - I_{dark}(\lambda)\right) \tag{3.1}$$

An online characterization algorithm can calculate the current thickness from the trans-

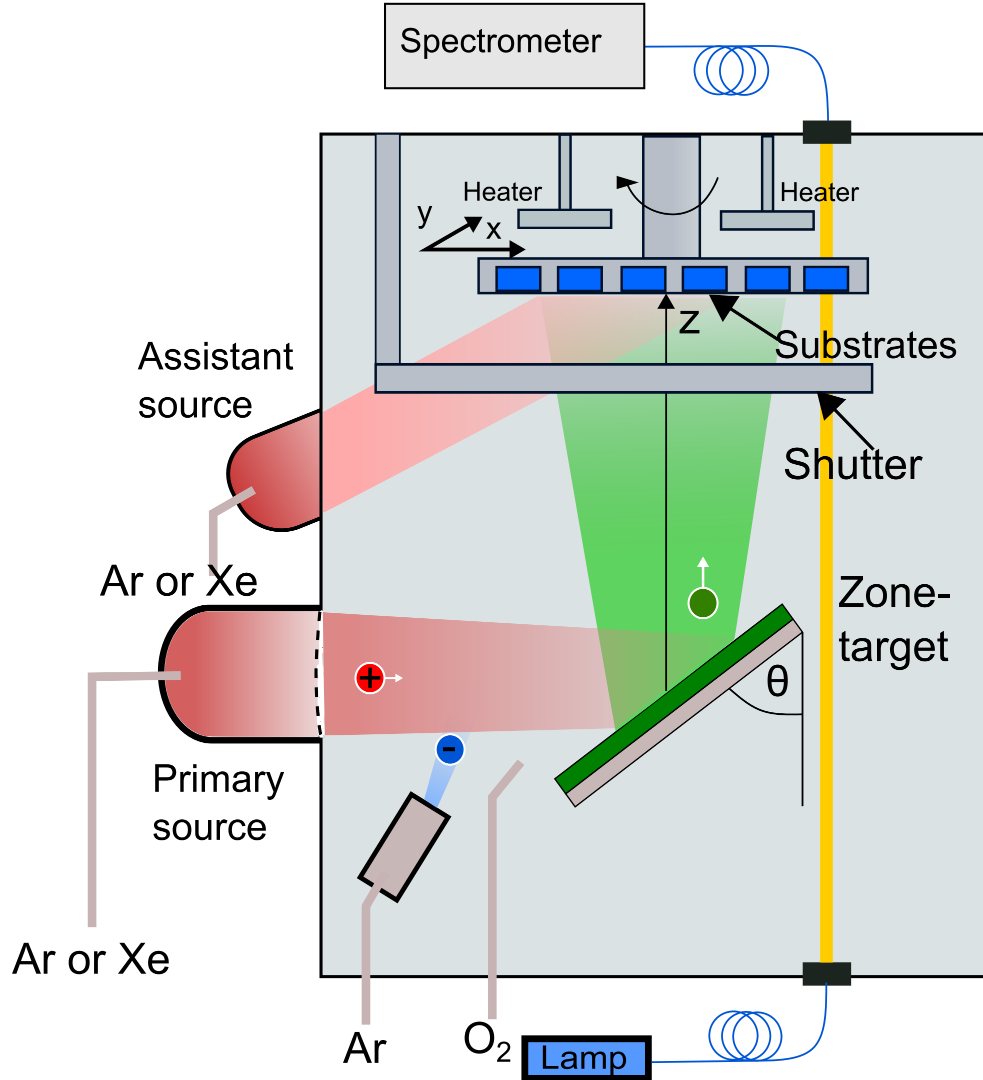

Figure 3.3: IBS coating plant with all important components. The plasma is generated in the primary source shown on the left. An assistant source ,which is used to modify the stoichiometry of material and clean substrates is also equipped. The neutralizer generating negative electrons is used to neutralize the positively charged ions shown at the bottom. The targets are mounted on a zone-target assembly. The BBOM system consisting of a broadband lamp, fiber and a spectrometer is also included.

mission spectra by the minimization of the discrepancy function:

$$F^j = \frac{1}{L} \sum \left[T^j \left(d_{(1,\lambda)}, \ldots, d_{(j,\lambda)} \right) - T^j \left(\lambda \right) \right]^2 \qquad (3.2)$$

For the termination of the current layer, the design to be produced is loaded to the BBOM software. In every measurement, the thickness is calculated from the transmittance spectra. When the target layer thickness is reached, the BBOM informs the system control

by the internal machine interface. Then the system control terminates the coating of the actual layer. In order to get a reliable determination of the current thickness, an accurate and stable transmittance measurement must be performed. The BBOM does not need any intervention during coating and a completely automated coating process is possible. However, the BBOM has some disadvantages. The thickness errors accumulate as the layer increases. Such accumulation of these errors will become extremely high after 20 or 30 layers [91], which fails to terminate the layer with correct thickness and introduces larger thickness errors to the top layers. This is detrimental especially for the production of dispersive mirrors, since the top layers of dispersive mirrors are much more sensitive to the thickness errors than the bottom layers. This method is also not suitable for ultra-broadband dispersive mirrors. Due to the broadband high reflection range, there is very less transmittance information, which makes it impossible to calculate the thickness precisely. Because of these disadvantages, the BBOM is not a good option for monitoring the production of dispersive mirrors.

The thickness can be controlled by the deposition time as long as the deposition rate is stable. IBS is known to have the property of a stable rate. For our IBS coating plant, the time control technique becomes possible. However, due to the consumption of the target and the erosion in the grid system, the rates might differ a little from coating run to run, resulting in the spectral shift of the coating. The spectral shift causes the degradation of the GDD characteristics, especially for the complementary dispersive mirror pair. The GDD oscillations will not be in anti-phase, resulting in large residual GDD oscillations. Moreover, the rates tend to fluctuate a little at the beginning of the coating process because of the instability of the ion source and the increase of the substrate temperature. In order to improve the monitoring technique for the production of dispersive mirrors, a combination of time control and BBOM control is applied.

3.1.3.2 Adjusting the non-uniformity

Non-uniformity is known to be the variation of physical thickness along the deposition area. It can be improved by implementing special designed masks and substrate rotation [92,93]. The non-uniformity is also limited by the angular distribution of the sputtered particles. The angular distributions for obliquely incident Ar ions are described by a superposition of a random part and a few collision part, which are schematically shown in Figure 3.4 [94]. The random part and the few collision part correspond to the indirect and direct knockout process, respectively. For our IBS plant, the best non-uniformity, which can be achieved based on the optimal substrate height and ion beam incident angle, is about 1% in a deposition area of 300 mm in diameter [56]. In addition, the desired non-uniformity can be obtained by adjusting the substrate height. As red arrows show in Figure 3.5, we can lift up and down the substrate holder to adjust the non-uniformity. Due to the substrate rotation during coating, the mirrors produced in the same ring are almost identical, there is only non-uniformity in the radial direction. This method is employed to suppress the GDD oscillations in chapter 5.

The non-uniformity is also adjustable by the post-deposition treatment. It is well-known

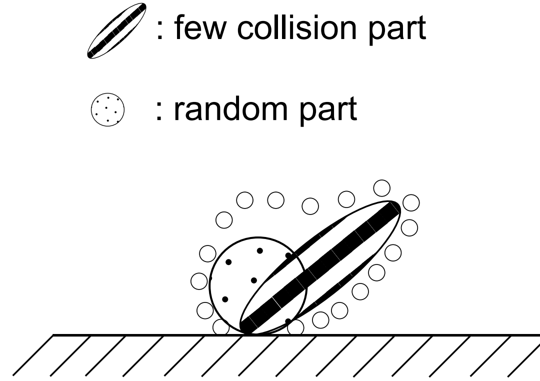

Figure 3.4: Schematic representation of an angular distribution of sputtered particles at oblique incidence.

that the property of multilayer coatings can be optimized by a proper post deposition treatment. Post deposition annealing (PDA) is a general process which is applied to treat the defects, reduce the impurities in the film and improve the dielectric properties [95, 96]. The PDA process were carried out in a small oven made by Linn Elektro Therm. The temperature is adjustable from 0 to 500 ℃, and the time can be set as up to 24 hours. During annealing, the oven is in an air atmosphere. For the coatings produced by our IBS plant, the annealing causes a decrease in the refractive index and an increase in the physical thickness. The optical thickness, which is a comprehensive result of changes in refractive index and physical thickness increases with the annealing. The spectral red shift resulted from the increase in the optical thickness is dependent on the annealing temperature, time and the thermal expansion coefficient of the substrate. Therefore, the non-uniformity between two samples can be increased or decreased by annealing one of the samples at the post-deposition stage.

3.2 Characterization of multilayer dispersive mirrors

Characterization is of the same importance to the design and production process. Successful and accurate characterization enables us to evaluate the coatings. For multilayer dispersive mirrors, transmittance, reflectance, total loss, GD and GDD are the characteristics of interest.

3.2.1 Transmittance, reflectance and total loss

The wavelength-resolved transmittance and reflectance measurements distinguished by the wavelength are performed by two techniques. The spectrometer unit is a device that diverses and measures the light, while the photometer unit measures the intensity of the light. In our case, the Perkin Elmer Lambda 950 spectrophotometer is employed to measure the transmittance and reflectance in the UV-VIS-NIR range. A universal reflectance

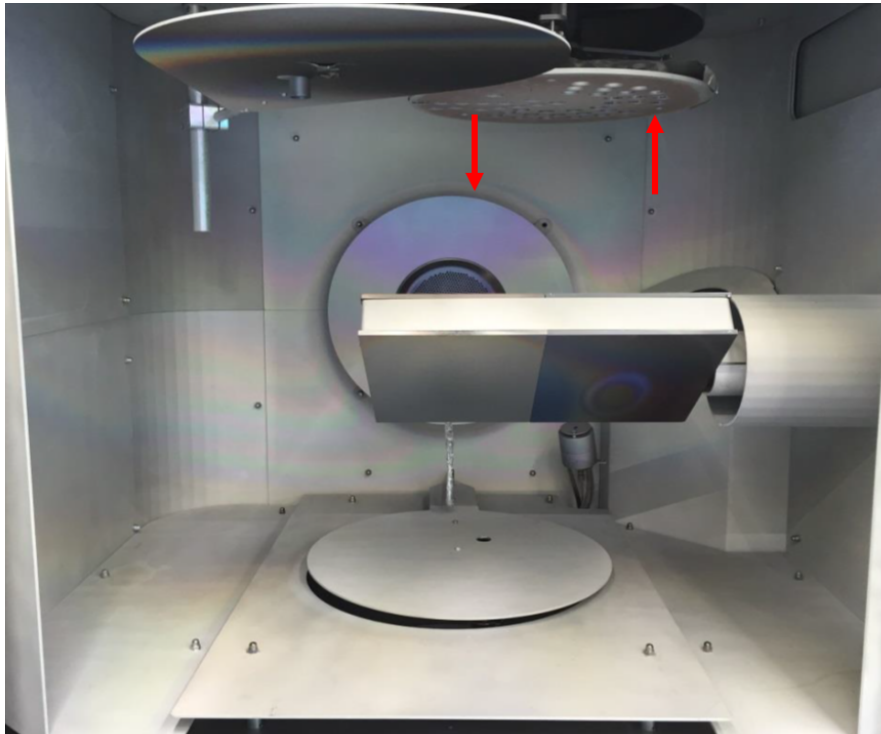

Figure 3.5: Interior view on the process chamber. The non-uniformity is adjustable by changing the substrate height as the red arrows show.

accessory (URA) is used for the absolute reflectance measurements at the incident angle from 8° to 65°. Deuterium and tungsten light sources and two detectors are able to cover the measurement range from 170 to 3300 nm. An integration sphere collecting light from a wide range of input angles, which can correct for inaccuracies due to refraction or light scattering effects, is applied for the transmittance measurements. Thus, an accurate and reproducible measurement can be achieved. The measurement errors are estimated to be less than 0.3%.

The other technique is based on a Fourier Transform Infrared spectrometer (FTIR). For a dispersive spectrometer, the samples are analyzed step by step, whereby the samples are irradiated with different single wavelengths split by a grating or prism, while for the FTIR spectrometer, the spectra data of all wavelengths are collected in one pass. The core of the FTIR spectrometer is a Michelson Interferometer, which is used to split one beam of light into two so that the paths of the two beams are different. Then the Michelson interferometer recombines the two beams, passes through the sample and conducts them into the detector where the difference of the intensity of these two beams is measured as a function of the difference of the paths. The interferogram as a function of path difference is transformed to the frequency domain by Fast Fourier Transform. To characterize the mid-infrared dispersive mirrors demonstrated in chapter 6, a Bruker Vertex 70 FTIR Spectrometer was employed. The spectral range covers from 1.25 to 28.5 μm, which is limited by the light

source, beam splitter and the detector. For transmittance measurements the accessory A480 from Bruker is used, which collimates the beam at the sample position for precise absolute results. The absolute reflectance measurements are performed with the V-W accessory A519.

In order to measure the total loss or reflectance with high precision for high reflective mirrors (usually higher than 99.9%), another reflectometer GLACIER made by Ultrafast innovations was employed, which is based on the cavity ring down (CRD) technique [97,98]. The measurement can be carried out at AOI of 7.5° and 45° at the available wavelengths of 808 nm, 1030 nm and 1550 nm. Total loss on the scale of a few parts per million (ppm) can be accurately measured by the CRD method [97]. The minimum instrument precision is typically less than 1% of the total measured loss.

3.2.2 GD and GDD

In this work, GD and GDD of the dispersive mirrors were measured by two home-built white light interferometers (WLI), which are based on the well-known Michelson Interferometer. One of them is responsible for the VIS-NIR measurements. The principle and setup were described in the thesis of Dirk Grupe [99]. A robust and reliable algorithm was developed by Amotchkina et al. [100]. Based on our home-built WLI and algorithm, the GDD measurement error is estimated to be about 5 fs^2. The GD and GDD measurement in chapter 4 and 5 were carried out by this setup and algorithm. The second WLI was developed by Florian Habel [101], which was used to characterize the mid-infrared DM in chapter 6.

Chapter 4

Dispersive mirrors with ion beam sputtering and comparison with magnetron sputtering

Dispersive mirrors (DMs) were first invented by Szipocs et al. in 1994 [14]. Since 1994, a lot of scientists have been attracted into this field. For the past two decades, DMs exploited as intracavity and extracavity dispersion compensation components have been widely used in all kinds of ultrafast laser systems, including Ti:sapphire oscillators [34–37], Yb:YAG disk oscillators [38–40], Erbium-doped fiber chirped pulse amplification systems [41], etc. [45,102]. DMs have covered the wavelength range from the ultraviolet [103], visible [34–37], infrared [38–42, 45, 102, 104], to the mid-infrared region [21, 53]. Nowadays DMs become the key elements to control dispersion in ultrafast laser systems.

Broadband dispersive mirrors (BBDMs) [21–25,53] and high dispersive mirrors (HDMs) [34–42] are the two mostly used DMs. Design and manufacture of both kinds of DMs are the challenges. The first dispersive mirror [14] was fabricated by electron beam evaporation in spite of its relatively low accuracy in layer thickness control. However, as more complicated DMs were required to meet the dispersion control in laser systems, the electron beam evaporation technique was no longer suitable for producing DMs. Magnetron sputtering (MS) [21–25, 38–40, 53] and ion beam sputtering (IBS) [41, 54], which have improved layer thickness accuracy and process stability, became the most widespread coating processes for manufacturing DMs. Both processes deposit layers with excellent uniformity of physical thicknesses and high stability to environmental conditions compared to layers produced by electron beam evaporation. Many experiments and studies about the comparison between different coating processes have been done before. However, they mainly focused on the single layers and simple multilayers and compared their structural, optical and the electrical properties. These single layers and multilayers are relatively simple and not sensitive to deposition errors. Thus, the production of these coatings has no challenge. However, DMs are one of the most complicated multilayer coatings. The production of DMs is still quite challenging. MS and IBS are the most widely-used technologies to produce DMs. Compared to MS, IBS has some advantages of being able to deposit larger-scale

and lower-loss coatings. Coatings with diameters up to 600 mm is achievable for IBS, while only 200 mm in diameter coatings is available for MS. IBS has the potential to produce large-scale and low-loss DMs. However, the deposition accuracy of IBS must be first verified good enough for the production of DMs. BBDM and HDM are two typical DMs, which are sensitive to absolute errors and relative errors, respectively. Successful production of both DMs could prove the capacity of IBS to produce all kinds of DMs. In addition, a direct comparison of GDD characteristic between MS-produced and IBS-produced DMs can be a concrete proof for the deposition accuracy of IBS. The design, production and characterization of BBDMs and HDMs are presented in section 4.1 and section 4.2. Comparisons of GDD performance of DMs produced by MS and IBS are shown in section 4.3. Finally, a conclusion and an outlook of this chapter are drawn in section 4.4.

4.1 Design, production and characterization of broadband double angle DMs

4.1.1 Design of BBDMs

Double angle DMs were designed by the OptiLayer software [81]. In order to cover a wide-range from 500 nm to 1050 nm, Nb_2O_5 and SiO_2, which have a large refractive index ratio, were chosen as the layer materials. Suprasil was used as the substrate. The optical constants of the substrate and layer materials are specified by the Cauchy formula:

$$n(\lambda) = A_0 + A_1/\lambda^2 + A_2/\lambda^4 \tag{4.1}$$

where λ is expressed in micrometer and the coefficients of A_0, A_1 and A_2 are presented in Table 4.1 [30]. In order to compare the refractive indexes between MS and IBS intuitively, the indexes at the wavelength of 800 nm are shown in Table 4.1 as well. One can see that for the high refractive index material, IBS has a smaller index than MS, while for the low refractive index material, IBS has a larger index than MS, which makes the refractive index ratio of MS greater than that of IBS. Larger ratio means larger bandwidth of a quarter-wave-high-reflective coating (QWHR). Moreover, it is a little easier to design a dispersive mirror with a larger ratio.

5° and 19° were chosen as the two different working angles [24]. The target reflectance was set to 100%. GDD should compensate 1 m of air and 1 mm of fused silica in two reflections with this mirror. The needle optimization and gradual evolution algorithms [82, 83] were used to minimize the merit functions, which were defined as below:

$$\mathrm{MF}^2 = \alpha_1 {\mathrm{MF}_1}^2 + \alpha_2 {\mathrm{MF}_2}^2 + {\mathrm{MF}_\Sigma}^2 \tag{4.2}$$

$${\mathrm{MF}_1}^2 = \sum_{j=1}^{500} \left(\frac{\mathrm{R}(X^{(1)};\lambda_j) - 100}{\Delta \mathrm{R}_\mathrm{j}^{(1)}} \right)^2 + \sum_{j=1}^{500} \left(\frac{\mathrm{GDD}(X^{(1)};\lambda_j) - \mathrm{GDD}(T;\lambda_j)}{\Delta \mathrm{GDD}_\mathrm{j}^{(1)}} \right)^2 \tag{4.3}$$

Technology	Material	A_0	$A_1(\mu m^2)$	$A_2(\mu m^4)$	n (0.8 μm)
IBS	SiO_2	1.486272	-3.996783e^{-3}	5.8433165e^{-4}	1.49
	Nb_2O_5	2.179779	0.032789	1.9913311e^{-3}	2.24
	Suprasil	1.443268	0.004060	6.9481764e^{-6}	1.45
MS	SiO_2	1.465294	0.0	4.710804e^{-4}	1.47
	Nb_2O_5	2.218485	0.021827	3.9996753e^{-3}	2.26
	Suprasil	1.443268	0.004060	6.9481764e^{-6}	1.45

Table 4.1: Cauchy formula coefficients for the layer materials and the Suprasil substrate.

$$\mathrm{MF_2}^2 = \sum_{j=1}^{500} \left(\frac{\mathrm{R}(X^{(2)}; \lambda_j) - 100}{\Delta \mathrm{R}_\mathrm{j}^{(2)}} \right)^2 + \sum_{j=1}^{500} \left(\frac{\mathrm{GDD}(X^{(2)}; \lambda_j) - \mathrm{GDD}(T; \lambda_j)}{\Delta \mathrm{GDD}_\mathrm{j}^{(2)}} \right)^2 \tag{4.4}$$

$$\mathrm{MF_\Sigma}^2 = \sum_{j=1}^{500} \left(\frac{\mathrm{R_\Sigma}(\lambda_j) - 100}{\Delta \mathrm{R}_\mathrm{j}^{\Sigma}} \right)^2 + \sum_{j=1}^{500} \left(\frac{\mathrm{GDD_\Sigma}(\lambda_j) - \mathrm{GDD}(T; \lambda_j)}{\Delta \mathrm{GDD}_\mathrm{j}^{\Sigma}} \right)^2 \tag{4.5}$$

where the MF is the combined merit function, MF_1 and MF_2 are the merit function of the design at the incident angle of 5° and 19°, MF_Σ is the merit function of the mirror pair, α_1 and α_2 are the target weight of the design at two different angles; λ_j are evenly distributed wavelength points in the spectral range of 500 to 1050 nm; $X = d_1, \ldots, d_m$ is the vectors of layer thicknesses; $R(X^{(1)}; \lambda_j)$ and $R(X^{(2)}; \lambda_j)$ are the reflectance of the design at the angle of incidence of 5° and 19° , $\Delta R_j^{(1)}$ and $\Delta R_j^{(2)}$ are the corresponding reflectance tolerance ; $GDD(X^{(1)}; \lambda_j)$ and $GDD(X^{(2)}; \lambda_j)$ are the $GDDs$ of the design at two incident angles, $\Delta GDD_j^{(1)}$ and $\Delta GDD_j^{(2)}$ are GDD tolerance; $GDD(T; \lambda_j)$ is the GDD target which is the opposite sign of the dispersion of 0.5 m of air and 0.5 mm of fused silica; R_Σ is the geometric mean of $R(X^{(1)}; \lambda_j)$ and $R(X^{(2)}; \lambda_j)$, while GDD_Σ is the arithmetic mean of $GDD(X^{(1)}; \lambda_j)$ and $GDD(X^{(2)}; \lambda_j)$.

During the optimization, manual adjustment of the weight is necessary to obtain the best result. Finally, the designs of PC70 and PC470, which correspond to MS and IBS, respectively, were synthesized, which are shown in Figure 4.1 (a) and Figure 4.1 (b), respectively. The thickness structures are quite similar and there is just a slight difference due to the refractive index differences between the two plants as can be seen in Table 1. The total thickness of both structures is about 8.8 μm with 98 layers. Figure 4.2 depicts the GDD of the double angle DMs. The GDD oscillations of the individual mirror at two angles of incidence are just in anti-phase, and they cancel out each other. As a result, oscillations of the effective GDD, which is the arithmetic mean of the GDD for these two incident angles, has been suppressed significantly.

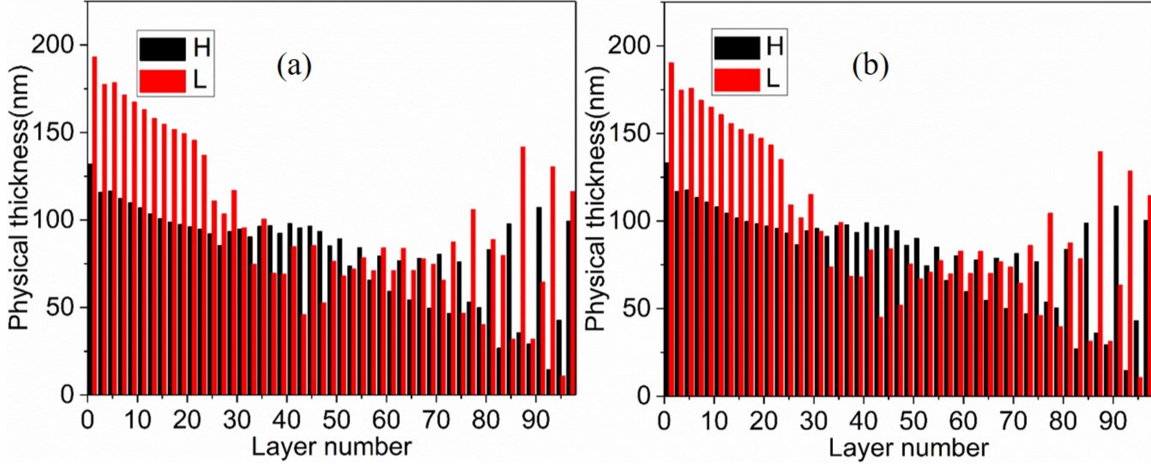

Figure 4.1: Layer thicknesses of double angle DMs: (a) MS, (b) IBS. The black and red bars represent the high and low index materials, respectively. The layer number starts at the substrate and increases towards the incident medium (air).

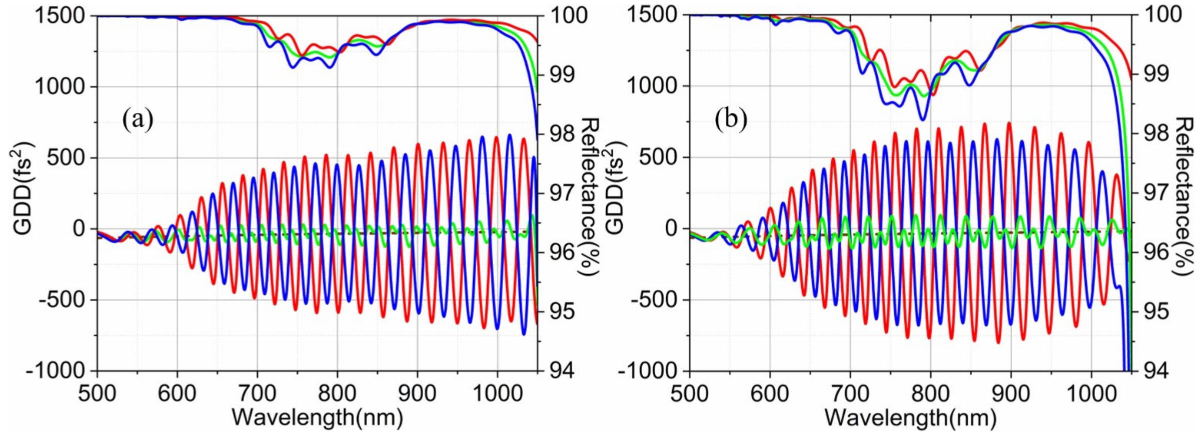

Figure 4.2: Theoretical GDD and reflectance of double angle DMs: (a) MS, (b) IBS. The red and blue curves correspond to the incident angle of 5° and 19°, while the green curves represent the effective GDD and reflectance.

4.1.2 Deposition and characterization of BBDMs

Both MS and IBS have proven to be the most reliable techniques for producing complicated DMs. The excellent stability and repeatability of sputtering techniques make them the most widely-used and successful methods to deposit all kinds of DMs. The design of PC470 was manufactured by a Navigator machine from Cutting Edge Coatings GmbH (Hannover, Germany). The ion beam is extracted from an Argon gas plasma by a three-grid multi-aperture extraction system. A cryogenic pump evacuates the coating chamber to 1×10^{-7} mbar before deposition. The pressure during the coating process is about 5×10^{-4} mbar. Due to stable sputtering rates, the layer thickness was controlled by time.

A broadband optical monitoring technique is also utilized, which allows us to monitor the in-situ transmittance and correct the deposition time during coating. Nb_2O_5 and SiO_2 materials were formed on the fused silica substrates by sputtering the pure Nb and Si target with additional oxygen. The deposition rates were approximately 0.09 nm/s and 0.1 nm/s, respectively. The design of PC70 was fabricated by a Helios machine from Leybold Optics GmbH (Alzenau, Germany). The plant is equipped with two proprietary dual-magnetrons and a plasma source for ion-assisted reactive middle frequency dual-magnetrons puttering. The magnetrons were optimized for high sputtering rates and high optical layer performance. The system was pumped by turbo-molecular pumps to 1×10^{-6} mbar before deposition. In the magnetron cathodes, Nb and Si targets were used. Oxygen was fed near the targets to oxidize the sputtering films. The distance from the targets to the substrates was 100 mm. The gas pressure was 1×10^{-3} mbar during the sputtering process. The layer thicknesses were also controlled by time. The deposition rates were approximately 0.5 nm/s for both materials.

After the production, the transmittance spectra of the DMs were measured by a spectrophotometer (Perkin Elmer Lambda 950) at normal incidence in the wavelength range of 400 to 1200 nm. The GDD was measured with a home-built white light interferometer [100]. The results of the measured transmittance and GDD can be compared with the theoretical values of the double angle DMs shown in Figure 4.3 and 4.4.

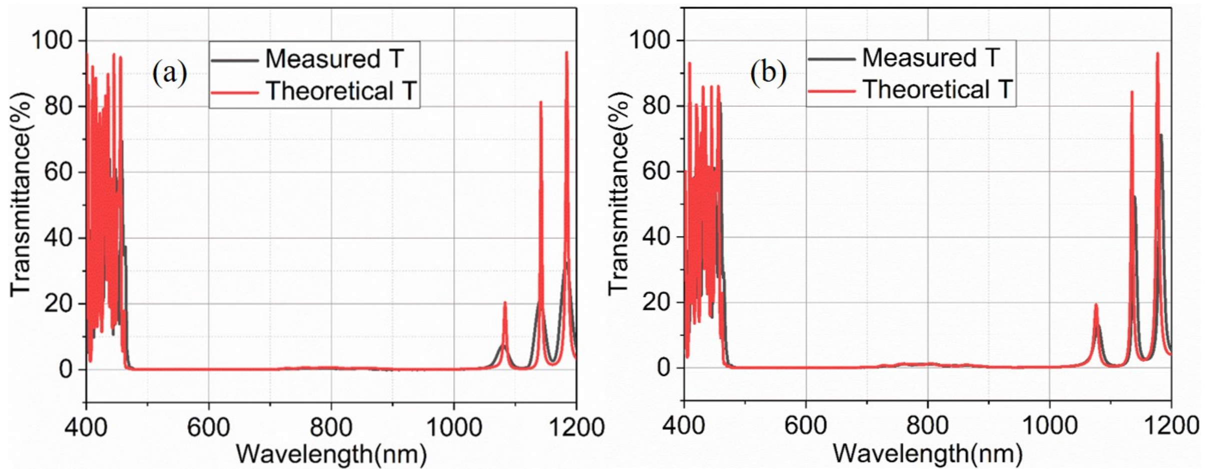

Figure 4.3: Measured and theoretical transmittance of double angle DMs: (a) MS, (b) IBS. Black and red curves represent the measured and theoretical transmittance, respectively.

Even though a small spectral shift can be observed in the measured transmittance, the measured GDD curves at 5° and 19° for both MS-produced and IBS-produced are matching each other, and the GDD oscillations are in anti-phase resulting in the significant decrease of the GDD oscillations for the effective GDD (black curves in Figure 4.4). Good agreement between the measured effective GDD and theoretical effective GDD for both IBS and MS processes was obtained.

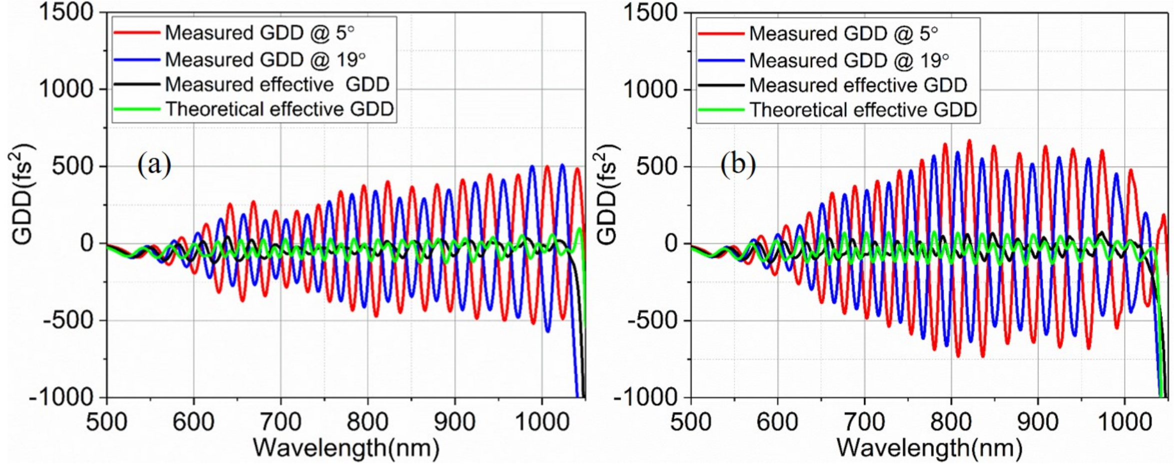

Figure 4.4: Measured and theoretical GDD of double angle DMs: (a) MS, (b) IBS. Red and blue curves correspond to the incident angle of 5° and 19°, black and green curves represent the measured and theoretical effective GDD.

4.2 Design, production and characterization of the robust HDMs

4.2.1 Design of HDMs

For the HDM, the well-known robust synthesis algorithm [105] was used to design the layer structure. It considered the layer thickness discrepancies. Ta_2O_5 and SiO_2 were chosen as the high and low refractive index materials, while Suprasil was the substrate. The refractive indices of the layer materials and the substrate for both MS and IBS technology were specified by the Cauchy formula. The coefficients of Cauchy formula and the refractive indices at 800 nm are shown in Table 4.2. The same trend is observed as for the Nb_2O_5 and SiO_2 pair shown in Table 4.1, which is a larger refractive indices ratio of MS than IBS. A larger ratio means less thickness is required to design a dispersive mirror with the same GDD and reflectance characteristics.

Technology	Material	A_0	$A_1(\mu m^2)$	$A_2(\mu m^4)$	n (0.8 μm)
IBS	SiO_2	1.486272	-3.996783e^{-3}	5.8433165e^{-4}	1.49
	Ta_2O_5	2.022438	1.8653421e^{-2}	1.1442954e^{-3}	2.05
	Suprasil	1.443268	0.004060	6.9481764e^{-6}	1.45
MS	SiO_2	1.465294	0.0	4.710804e^{-4}	1.47
	Ta_2O_5	2.065721	0.01683	0.001686	2.10
	Suprasil	1.443268	0.004060	6.9481764e^{-6}	1.45

Table 4.2: Cauchy formula coefficients for the layer materials and the Suprasil substrate.

By the robust synthesis approach [105], the number of samples in the cloud was set to

50 , which is enough for optimizing the DM according to our experience. The large weight of the absolute errors and small weight of the relative errors were considered. The absolute error and relative error were 0.5 nm and zero, respectively. The layer thickness of the j_{th} design in the cloud was described as:

$$d_i^{(j)} = d_i + \delta_{ij}, i = 1, ...N, j = 1, ...M \tag{4.6}$$

where N is the number of design layers, M is the number of designs in the cloud, the random values δ_{ij} are defined as:

$$\delta_{ij} = \delta\left(0, \sigma_{abs}^2\right) + \delta\left(0, \sigma_{rel}^2\right) \tag{4.7}$$

The reflectance and GDD values were optimized to 100% and -275 fs^2 at 800 nm for p-polarization. The corresponding merit functions were defined as follows:

$$MF_j = \left\{ \frac{1}{2L} \sum_{l=1}^{L} \left[\frac{R\left(X_j, \lambda_l\right) - R_l}{\Delta R_l} \right]^2 + \frac{1}{2L} \left[\frac{GDD\left(X_j, \lambda_l\right) - GDD_l}{\Delta GDD_l} \right]^2 \right\}^{1/2} \tag{4.8}$$

$$MF = \left\{ \frac{MF_0^2 + \sum_{j=1}^{M} MF_j^2}{M+1} \right\} \tag{4.9}$$

where λ_l are evenly distributed points in the wavelength range of 680 to 880 nm, $X_i = d_1, \ldots, d_m$ is the vector of layer thickness, MF_j is the partial merit function for the design X_j, $R(X_j, \lambda_l)$ and $GDD(X_j, \lambda_l)$ are the theoretical reflectance and GDD for the design X_j, R_l and GDD_l are the target reflectance, ΔR_l and ΔGDD_l are the corresponding tolerance, MF is the average merit function in the cloud.

The designs of HD58 and HD458 corresponding to MS and IBS were obtained. The theoretical reflectance and GDD of the two designs were depicted in Figure 4.6. The corresponding thickness structures are shown in Figure 4.5. The layer structure of HD58 consists of 74 layers with a total thickness of 12.6 μm, whereas the structure of HD458 includes 80 alternative high and low index layers with a total thickness of 13.2 μm. The IBS coating is a bit thicker due to the slightly smaller refractive index ratio of the material pair.

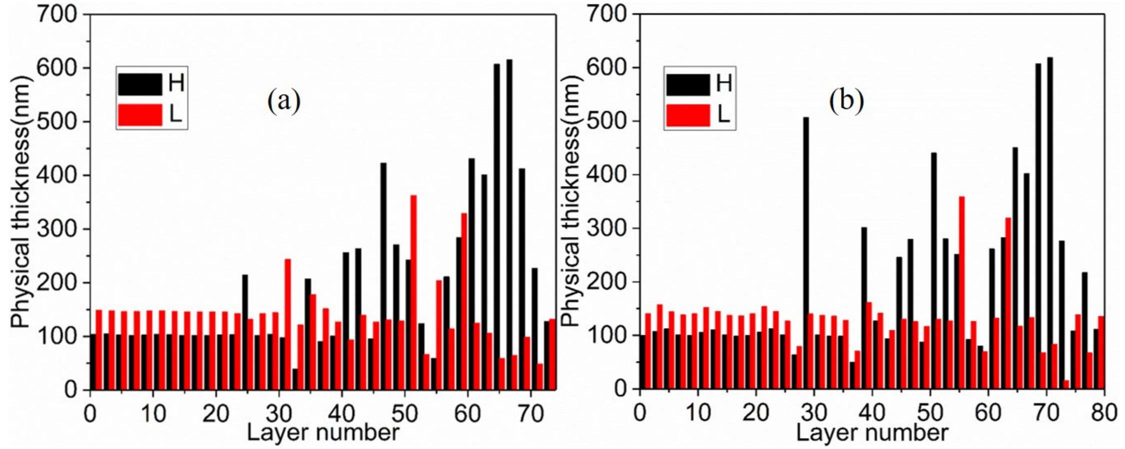

Figure 4.5: Layer thicknesses of HDMs: (a) MS, (b) IBS. The black and red bars represent the high and low index materials, respectively. The layer number starts at the substrate and increases towards the incident medium (air).

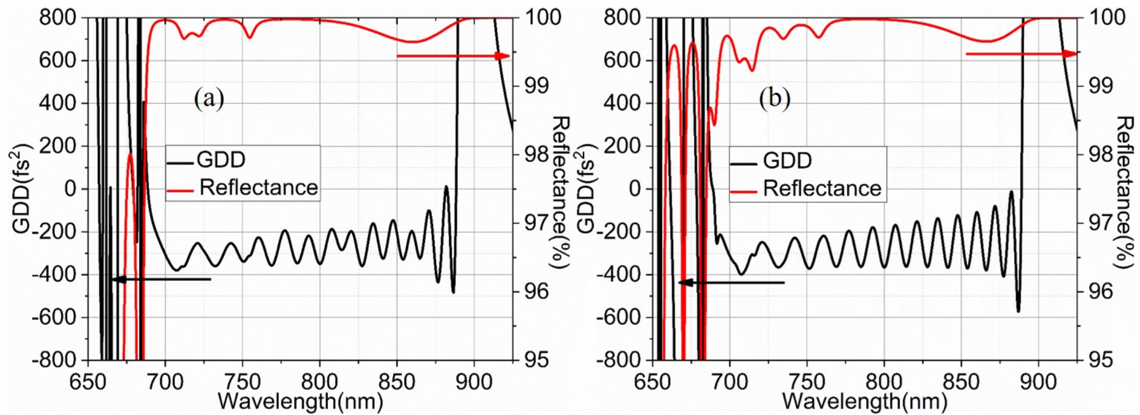

Figure 4.6: Theoretical GDD and reflectance of HDMs: (a) MS, (b) IBS. Red and black curves correspond to the theoretical reflectance and GDD.

4.2.2 Deposition and characterization of HDMs

The HDMs were produced by the IBS and MS technology with the same coating process to the double angle DMs. Ta_2O_5 and SiO_2 materials were sputtered from pure Ta and Si target with additional Oxygen. The deposition rates of Ta_2O_5 and SiO_2 were about 0.07 nm/s and 0.1 nm/s for IBS, while the deposition rates of both materials were about 0.5 nm/s for MS.

The measured transmittance and GDD compared with theoretical values of the HDMs produced by the two technologies are shown in Figure 4.7 and Figure 4.8. The transmittance measurements show that better agreement between the measured and the designed transmittance was obtained for the IBS-produced HDMs, especially for the longer wavelength region. GDD comparison shows that the measured GDD curves fit very well to the

theoretical GDD curves for both coating technologies.

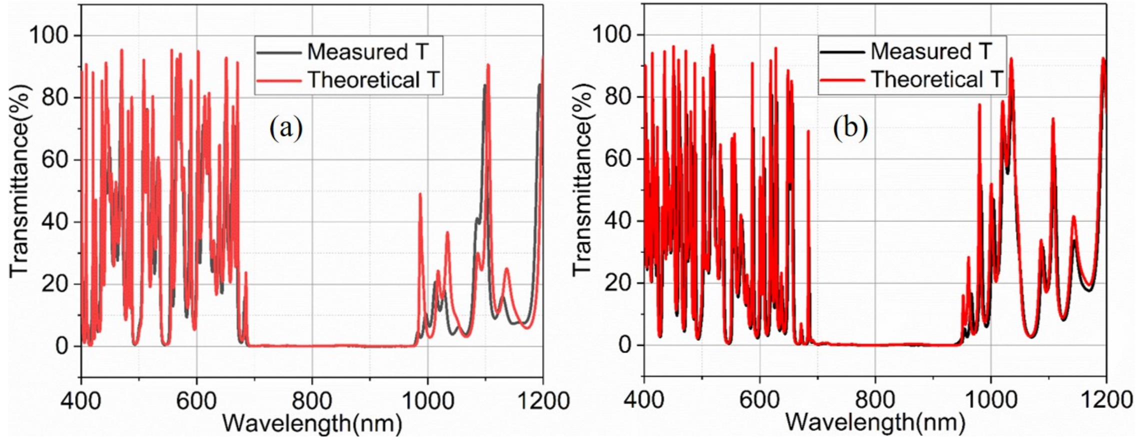

Figure 4.7: Measured and theoretical transmittance of HDMs: (a) MS, (b) IBS. Black and red curves represent the measured and theoretical transmittance.

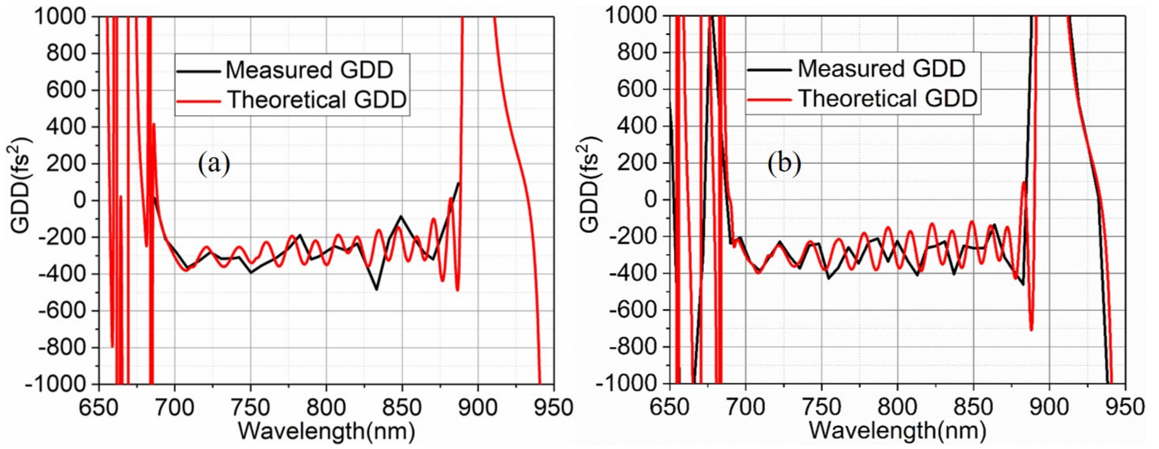

Figure 4.8: Measured and theoretical GDD of HMDs: (a) MS, (b) IBS. Black and red curves represent the measured and theoretical GDD.

4.3 Comparison of IBS with MS

GDD is the most important characteristic of DMs. Thus, the GDD results usually determine whether the coating run is successful or not. In order to estimate the measured GDD performance, we introduce a merit function to show the discrepancy between the measured GDD and target GDD. The merit function was defined as:

$$\mathrm{MF}^2 = \sum_{j=1}^{L} \left(\frac{\mathrm{GDD}(m, \lambda_j) - \mathrm{GDD}(T, \lambda_j)}{\Delta \mathrm{GDD}} \right)^2 \tag{4.10}$$

where $\{\lambda_j\}$ are the distributed wavelength points in the spectral range, GDD(m, λ_j) and GDD(T, λ_j) represent the measured GDD and target GDD at the corresponding wavelength, ΔGDD is the tolerance of GDD. According to equation 4.10, MF values are calculated, which is shown in the Table 4.3. One can see that for both broadband double angle DMs and Robust HDMs, the MF values of MS and IBS are very close and relatively small, which means a good agreement between the measured GDD and target GDD.

Technology	Broadband double angle DMs	Robust HDMs
MS	16.1	12.3
IBS	19.0	9.5

Table 4.3: MF values for the broadband double angle DMs and Robust HDMs.

Measured GDDs of double angle DMs produced by MS and IBS were plotted in Figure 4.9 (a). We can see that both GDD curves have relatively small GDD oscillations and almost the same amount of GDD oscillations. Furthermore, both measured GDD curves meet the target. A comparison of IBS-produced and MS-produced robust HDMs was investigated as well, presented in Figure 4.9 (b), which shows that both curves are close to the target and fulfill the GDD requirements. From the GDD comparison, both DMs manufactured by the two technologies have similar GDD characteristics, including the amount of GDD and the number of GDD oscillations. This demonstrates that IBS and MS have a comparable accuracy of the deposited layer thicknesses, by which the produced DMs are composed of.

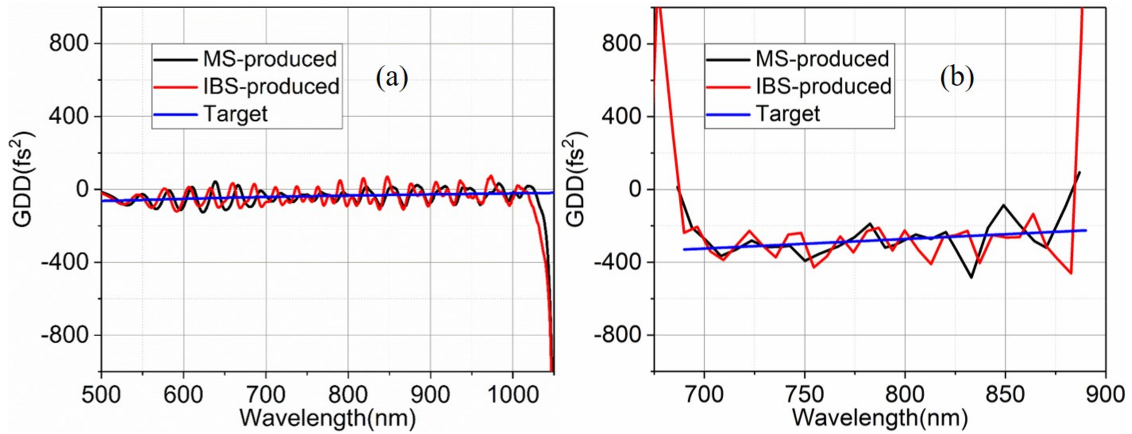

Figure 4.9: Measured GDD of MS-produced and IBS-produced DMs: (a) double angle DMs, (b) HDMs. Red, black and blue curves represent the MS-produced DMs, IBS-produced DMs and the corresponding target, respectively.

4.4 Conclusion and outlook

Two different types of DMs have been designed, fabricated and characterized. The comparison of the measured transmittance and GDD with the theoretical values indicates that both DMs produced by MS and IBS are successful. Furthermore, a comparison of the characteristics of the MS-produced and IBS-produced DMs is drawn for the first time. The GDD comparison proves that the IBS technology and the MS technology can produce DMs with the same precision.

With the demand of high-power laser systems increasing, large-scale and low-loss dielectric coatings, including highly reflective mirrors as well as dispersive mirrors, draw more and more scientist's attention. The IBS is able to deposit mirrors up to a diameter of 600 mm with a uniformity better than 1%. Ultra-low loss mirrors have been successfully produced with a total loss value of 1 ppm. The large coating area and the achievable loss values are the two main advantages of the IBS technology compared to the MS technology. These two advantages as well as the high deposition accuracy make IBS more suitable and promising for producing large-size, low-loss and complicated dispersive mirrors in the future. The MS technology is significantly faster (roughly by factor of 5) and can coat more substrates with smaller size (10 pieces of up to 200 mm in diameter) in comparison to only one 200 mm substrate in the case of IBS technology.

Chapter 5

New approaches to suppress the GDD oscillations

The impedance mismatching between the front layers and the incident medium results in the inevitable GDD oscillations [58]. DMs with large GDD oscillations will broaden the pulse duration and increase the satellites, which severely damage the pulse quality. Several methods including the single-mirror approach and the mirror-pair approach have been proposed to suppress GDD oscillations. In this chapter, two new approaches are proposed to deal with GDD oscillations. In section 5.1, we introduce a new method which employs two mirrors produced in one coating run with anti-phase GDD to suppress GDD oscillations. The anti-phase GDD is realized by the spectral shift between the two mirrors caused by the non-uniformity and post-deposition annealing. This section is mainly reproduced from my publication [106]. In section 5.2, a new one octave DM pair with smooth GDD oscillations based on non-uniformity is shown. Comparison of the new DM pair and the double angle DM pair in terms of GDD characteristics and pulse analysis is investigated.

5.1 Suppression of GDD oscillations of HDMs by non-uniformity and post-deposition treatment

Dispersive mirrors (DMs), providing precise control of group delay dispersion (GDD), have become one of the key elements in ultrafast laser systems over the last two and a half decades [14, 23, 32, 54, 55, 107–111]. Highly dispersive mirrors (HDMs), as one of the main research directions of DMs, which provide large values of GDD and high reflectance, have been used as the pulse compressor in Ti: Sa lasers [35–38], near-infrared Yb lasers [39, 40, 43, 45, 102, 112, 113] and Er-doped fiber lasers [41].

DMs provide the desired GD and GDD by combining the penetration effect and resonance effect [20]. The penetration effect means different frequencies of light penetrate and reflect at different positions in the layer structure. For example, red light penetrates deeper compared to the blue part of the light, which introduces negative GDD. While the resonance effect means that certain frequencies of light are trapped and oscillating in the

cavities, which act as Fabry–Perot interferometers in the multilayer structure. Therefore, large amounts of group delay can be introduced at the selected frequency. With an increasing amount of target GDD, resonance effects, which play the main role in introducing dispersion in HDMs, are significantly enhanced and the HDMs become much more sensitive to layer thickness inaccuracies [114]. Even a well-experienced coating engineer and state-of-the-art thickness monitoring techniques are not able to guarantee that every coating run is accurate enough and the GDD requirements are fulfilled. These production errors result in additional GDD oscillations and introduce higher order dispersions, even though the designed GDD curve has a small oscillation level. Moreover, most of the HDMs are used as pulse compressors [36, 37], which means a large number of bounces on the HDMs are needed in order to compress the pulses. Therefore, the GDD oscillations are significantly accumulated after several reflections, which will largely reduce the pulse quality of the laser system. Complementary DM pairs [22, 26] and double angle DM pairs [24] which are the two most common approaches to reduce GDD oscillations, share the same concept of shifting the spectra of two mirrors so that the GDD oscillations of the two mirrors are in antiphase and cancel each other. However, they are developed to suppress the GDD oscillations from the design side and don't consider the possible GDD oscillations due to the deposition discrepancies. Unfortunately, the inevitable deposition inaccuracies lead to a significant increase of the residual GDD oscillations. This effect is especially harmful in the case of complementary DM pairs.

Magnetron sputtering (MS) [23, 35–39, 107] and ion beam sputtering (IBS) [26, 41, 54] are the most reliable and widespread coating processes for manufacturing DMs. In this work, IBS was used to produce the HDMs. For IBS, the angular emission distribution of sputtered materials is often described as an under-cosine or heart shape distribution [115]. This means that at a certain plane, where the substrates are located, deposited thicknesses on the substrates on a large surface are not exactly the same, which is known as the non-uniformity effect [57]. Non-uniformity resulting in the shift of spectra is the disadvantage we are usually trying to avoid. However, in this work we propose to use this shift caused by the non-uniformity together with an additional shift due to annealing in order to suppress GDD oscillations at a post-deposition treatment stage. Simulations of pulse envelopes reflected from an individual mirror (without post treatment) and the HDM pair (one is with post treatment and the other is without post treatment) are presented, which shows that the new combination of non-uniformity and annealing could improve the pulse quality. The design approach of the HDM is shown in section 5.1.1. The production process and the characterization of the HDM are presented in section 5.1.2. The post-deposition annealing and pulse simulations reflected from the HDM are demonstrated in section 5.1.3. Finally, we give our conclusion in section 5.1.4.

5.1.1 Design of the HDM

For HDMs with a working range from 980 to 1080 nm, Ta_2O_5 and SiO_2 were considered as the high and low refractive index materials, respectively. Suprasil (fused silica) was chosen as the substrate. The refractive indices of the layer materials and the substrate

were specified by the Cauchy equation:

$$n(\lambda) = A_0 + A_1/\lambda^2 + A_2/\lambda^4 \quad (5.1)$$

with coefficients shown in Table 5.1 (for the wavelength expressed in μm). The comparison of the refractive indices at the wavelength of 1030 nm between with annealing and without annealing is also presented in Table 5.1. It indicates that the refractive indices of both Ta_2O_5 and SiO_2 decrease after annealing. The decrease of the refractive indices results from the increase of the void fraction, which is related to the stress relaxation of the films during annealing. The refractive indices of materials were calculated from the transmittance spectrum.

Material	A_0	$A_1(\mu m^2)$	$A_2(\mu m^4)$	n(1030 nm)	n_{an}(1030 nm)
SiO_2	1.486272	-3.996783e^{-3}	5.8433165e^{-4}	1.478	1.461
Ta_2O_5	2.022438	1.8653421e^{-2}	1.1442954e^{-3}	2.041	2.029
Suprasil	1.443268	0.004060	6.9481764e^{-6}	1.447	1.447

Table 5.1: Cauchy formula coefficients for the layer materials and the Suprasil substrate.

In order to design this HDM, the commercial Optilayer software [81], which includes powerful needle optimization and gradual evolution algorithms [82], was employed. The GDD and reflectance target were chosen as -500 fs^2 and 100% in the range from 980 to 1080 nm, respectively. The final layer structure is presented in Figure 5.1. It was composed of 18 pairs of approximately alternating quarter-wave layers (corresponding to the central wavelength of 1030 nm), which was used to provide high reflectance, and 14 top layer pairs, which mainly contributed to the dispersion. The theoretical GDD and reflectance were depicted in Figure 5.2.

5.1.2 Deposition and characterization

The HDMs were fabricated by ion beam sputtering at a Navigator IBS Deposition System (Cutting Edge Coatings GmbH, Germany). The well-calibrated time control technique was used to control the layer thickness. The plant is also equipped with a broadband optical monitoring system (BBM), which allows us to monitor the in-situ transmittance spectrum. A cryogenic pump was exploited to keep the coating chamber at a pressure of 5×10^{-7} mbar before deposition. Argon and oxygen were used in the process, and the pressure during the coating process was about 5×10^{-4} mbar. The Ta_2O_5 and SiO_2 materials were sputtered from Ta and Si targets on a zone target assembly. The corresponding deposition rates were approximately 0.07 nm/s and 0.1 nm/s. Four Suprasil substrates with the diameter of 1-inch were put at four different positions in the substrate fixture (the substrate 1 to 4 were put from the centre to the fourth cycle, respectively). The substrate fixture was rotated with a speed of 60 rounds per minute (rpm).

A load-lock was used to load and unload samples without venting the main coating chamber. The samples from the centre to the fourth cycle were named as HDM-1, HDM-2,

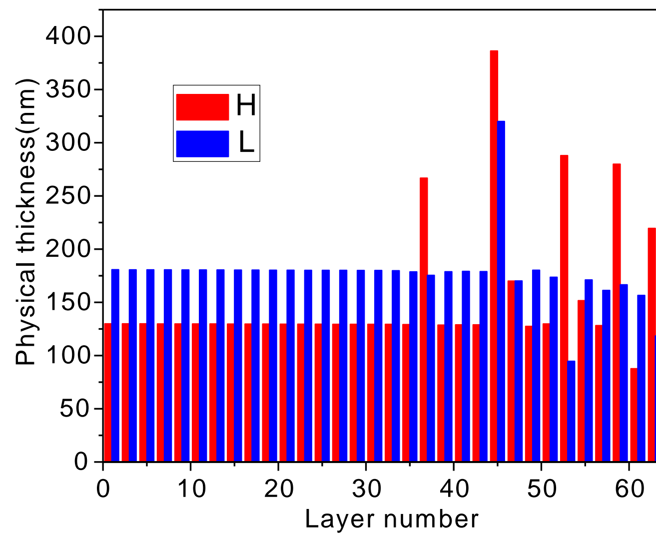

Figure 5.1: Layer thickness of the HDM. The red and blue bars represent the high and low index materials, respectively. The layer number is starting from the substrate to the incident medium (air).

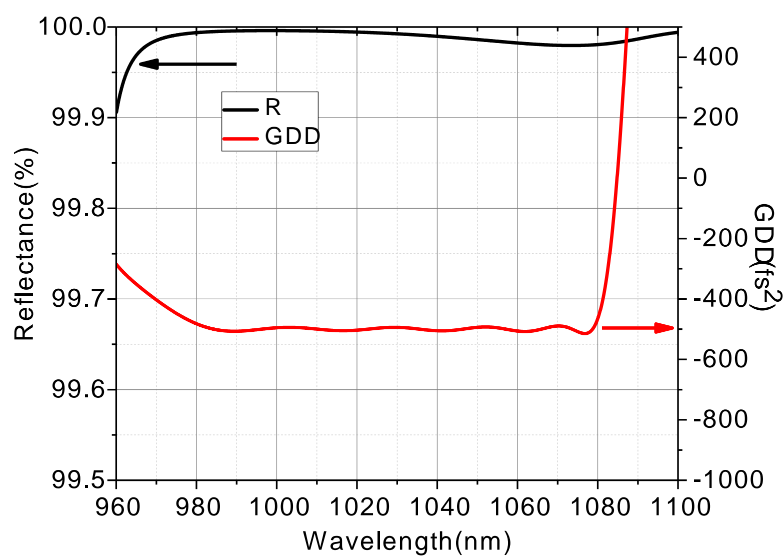

Figure 5.2: Theoretical GDD and reflectance of the HDM. Red and black curves correspond to the designed GDD and reflectance.

HDM-3 and HDM-4. The transmittance of the four samples in the wavelength range of 400 to 1400 nm were measured by a Perkin-Elmer Lambda 950 spectrophotometer. The results compared to the theoretical ones are shown in Figure 5.3. It can be seen that the transmittance spectra of HDM-1 to HDM-3 fit better to the theoretical one compared to the sample of HDM-4. Due to the non-uniformity, the sample HMD-4 is shifted to shorter wavelengths for about 10 nm in the vicinity of 1030 nm. The thickness non-uniformity on the 1-inch samples is negligible, especially in the direction perpendicular to the radius. For HDM-1 to HDM-3, every transmittance peak matches the theoretical one very well. However, the absolute value may have small differences to the designed value in some areas. That means layer thickness deviations exist in this coating run. In order to test whether these samples meet our dispersion requirements, GD and GDD data of the sample HDM-4 were measured by a home-built white light interferometer [100]. The results are depicted in Figure 5.5 and 5.6 (red line), which show large GDD and GD oscillations and ripples compared to the theoretical curves . These GDD ripples can broaden/deform the pulse shape, lead to the appearance of satellites of the initial single pulse and severely damage the laser pulse quality, which means the GDD requirement is not fulfilled. In this case another coating run is needed, but this is time-consuming and costly. Thus, on the purpose of saving a large amount of time and cost, a post-deposition treatment on HDMs to reduce GDD oscillations and improve the quality of HDMs was studied.

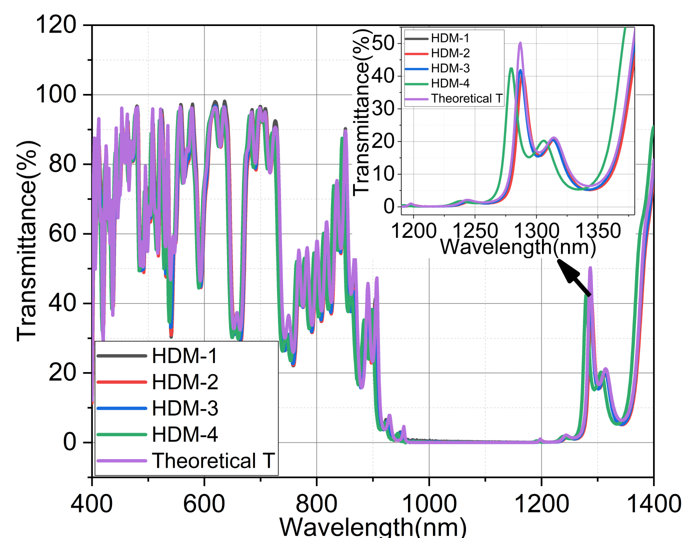

Figure 5.3: Measured transmittance and theoretical transmittance of HDMs. Black, red, blue and green curves represent the transmittance of sample HDM-1 to HDM-4, respectively. The violet curve corresponds to the theoretical transmittance. The inset shows the zoomed in transmittance around 1300 nm.

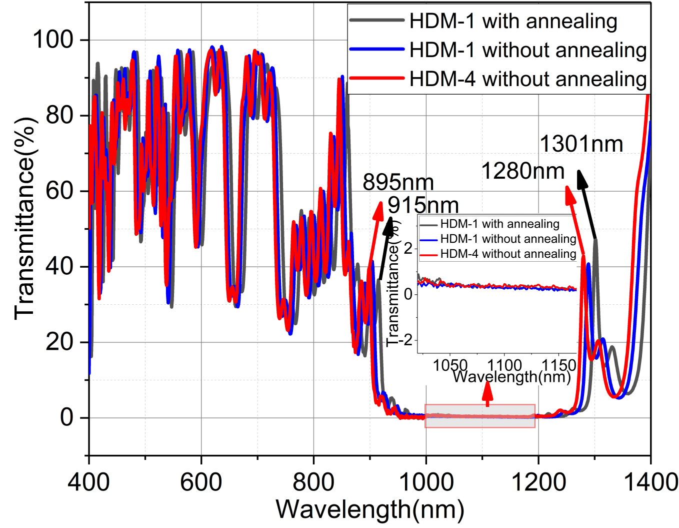

Figure 5.4: Measured transmittance of HDM with annealing and without annealing. The inset shows the enlarged transmittance curves from 1000 nm to 1150nm. Black, blue and red curves correspond to the transmittance spectrum of HDM-1 with annealing, HDM-1 without annealing and HDM-4 without annealing, respectively.

5.1.3 Post-deposition annealing and discussion

Based on the same concept as the complementary DM pairs and the double angle DM pairs, as long as we are able to let the spectrum of one sample shift to an optimal position where the GDD oscillations of the two samples are in antiphase, the effective GDD, which is the arithmetic mean of the GDDs of the two mirrors, will decrease significantly. Thus, we can use this concept at the stage of post-production HDM treatment.

The measured GDD results (in Figure 5.5) show that the distance between two GDD ripples is about 40 nm. So, if we shift the spectrum of one HDM for about 20 nm, the GDD ripples will be suppressed. In Figure 5.3, it is seen that due to the non-uniformity the sample of HDM-1 has approximately 10 nm red shift compared to sample of HDM-4. However, 10 nm shift is not enough to get the GDD oscillations exactly in antiphase and reduce the GDD oscillations. According to previous experiments and published literature [116], we know that post-deposition annealing can cause an increase of the optical thickness of the thin films, resulting in a red shift of the spectrum. Therefore, we decided to combine the spectral shift resulted from the non-uniformity and annealing. The increase of the optical thickness is the comprehensive result of a decrease in the refractive index and an increase in the physical thickness, which can be explained by a decrease in the density of the film, resulting from an increase in the void fraction. The change of the refractive index with annealing are shown in Table 5.1. The increase in the void fraction is related to the

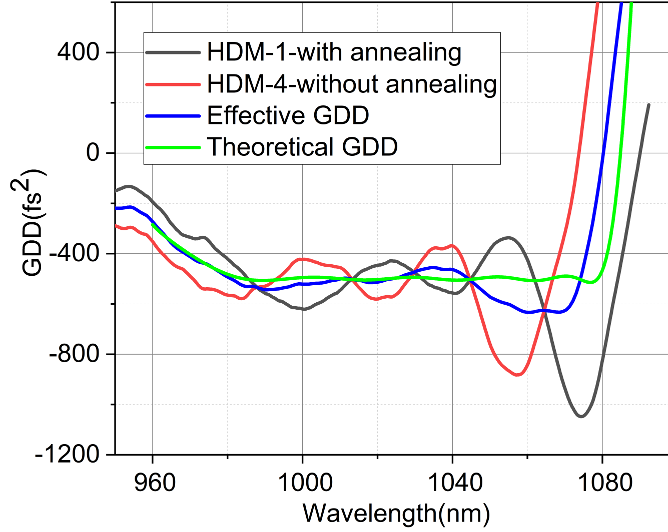

Figure 5.5: Measured GDD of HDMs. Black, red and blue curves correspond to the measured GDD of HDM-1 with annealing, HDM-4 without annealing and the effective GDD, respectively. The green curve corresponds to theoretical GDD.

stress relaxation of the film. The spectral shift is dependent on the annealing temperature, time and coefficient of thermal expansion of the substrate (CTE). The spectral shift can be manipulated by the annealing parameters. With a higher temperature, longer time and a smaller CTE, we can get a bigger spectral shift. However, we cannot increase the spectral shift indefinitely with the temperature and time. The film starts to be crystallized when the temperature is higher than 500℃ [96, 117], which will lead to a significant increase of the extinction coefficient. Furthermore, the spectral shift is saturated when the annealing time reaches 10 hours. In order to prevent the film from becoming crystalline and get the appropriate spectral shift, HDM-1 with 10 nm red shift compared to HDM-4 was chosen for a post-deposition annealing treatment. It was to be annealed at 400℃ in air for 12 hours in an oven. After annealing, the transmittance, GDD and GD of HDM-1 were measured, which are shown in Figure 5.4, 5.5 and 5.6, respectively. The characteristic of HDM with annealing is robust in respect to the aging issue. We have performed transmission measurement 22 months later and could not see any difference, which is shown in Figure 5.7.

In Figure 5.4, we can observe that the transmittance curves are similar in the low transmittance range, which shows that there should be negligible difference in reflectance in the high reflectance range between samples as well. In addition, the transmittance spectrum of HDM-1 has shifted for about 10 nm to longer wavelengths after annealing. This means that the combination of the non-uniformity and annealing will result in approximately 20 nm spectral shift between the HDM-1 with annealing and the HDM-4 without annealing, as

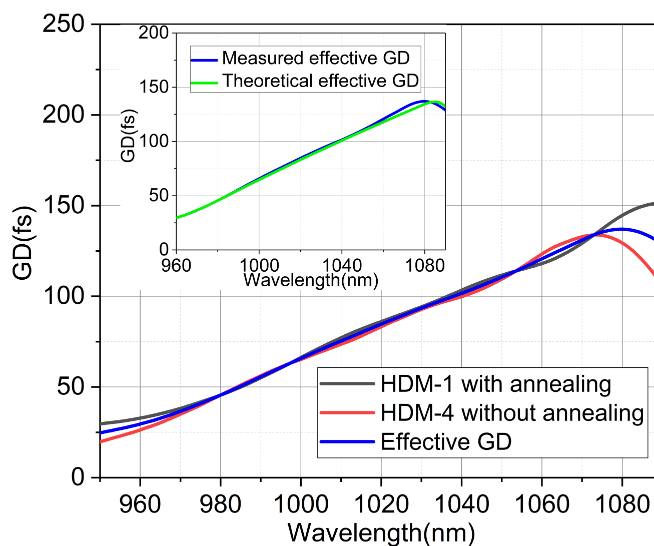

Figure 5.6: Measured GD of HDMs. Black, red and blue curves correspond to the measured GDD of HDM-1 with annealing, HDM-4 without annealing and the effective GDD, respectively. The blue curve and the green curve in the inset are the measured effective GD and theoretical GD.

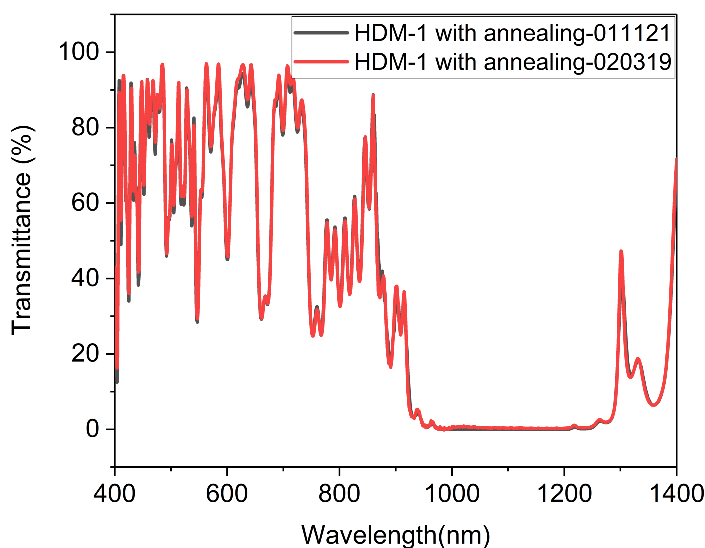

Figure 5.7: Measured transmittance of HDM-1 with annealing at different time. Black and red curves represent the measurement performed on 01112021 and 02032019.

shown in Figure 5.4, which positions GDD in antiphase. We choose HDM-1 with annealing and HDM-4 without annealing as a HDM pair whose effective GD and GDD oscillations should be suppressed. Figure 5.5 and 5.6 represent the measured GDD and GD results. It is clearly shown that GD and GDD oscillations of HDM-1 with annealing and HDM-4 without annealing are in antiphase, and the ripples match each other, resulting in a significant decrease of effective GD and GDD oscillations as the blue curves show. This proves that our HDM pair, based on the combination of non-uniformity and post-deposition treatment, is capable of decreasing the GD and GDD oscillations.

As a pulse compressor, dozens of reflections on highly dispersive mirrors are needed. This can potentially lead to a fast accumulation of GDD oscillations. These large GDD oscillations will decrease pulse quality significantly, including pulse duration and pulse intensity. In order to compare and evaluate the compression capability of the individual mirror and the HDM pair, we simulated the pulse envelopes reflected from the sample of HDM-4 without annealing and the HDM pair, respectively. We assumed that the input pulse was a Fourier-limited super-Gaussian pulse with a pulse duration of 32.2 fs covering the bandwidth from 980 to 1080 nm. The input pulse first propagated through an imaginary black box with dispersion which was 10 times of the amount of target GDD with opposite sign. Then the pulse was reflected by the HDM-4 without annealing and the HDM pair with 10 bounces, respectively. In Figure 5.8, the simulated envelopes of the input pulse and the pulse reflected from the individual mirror and the HDM pair are presented. During the simulations, the measured GDD values were used for both the individual mirror and the HDM pair. One can observe that the pulse shape after 10 bounces on the individual mirror has deformed and pulse intensity has decreased by 16% due to the increase of the pedestal. Moreover, the pulse duration has been broadened from 32.2 fs to 34 fs. On the other hand, the pulse shape reflected from the HDM pair keeps almost unchanged. The intensity has only dropped by approximately 3% and the pulse duration after bouncing 10 times is very close to the input pulse duration.

5.1.4 Conclusions

A highly dispersive mirror has been designed, produced and characterized. A post-deposition treatment, based on the selection of properly shifted HDM pairs due to non-uniformity and selective application of an additional annealing process, is proposed to suppress GDD oscillations. The measured GD and GDD have proven that our new method is an effective way to reduce GD and GDD oscillations. Furthermore, simulations of pulse envelopes reflected from the individual mirror and the HDM pair have been conducted, which further verified that our post-deposition treatment could improve the pulse quality for the corresponding laser system.

The advantage of our new approach is that large amounts of coating time and cost is saved, since it avoids the waste of failed coating runs. In addition, this offers a new post treatment way to deal with GDD oscillations resulting from deposition inaccuracies.

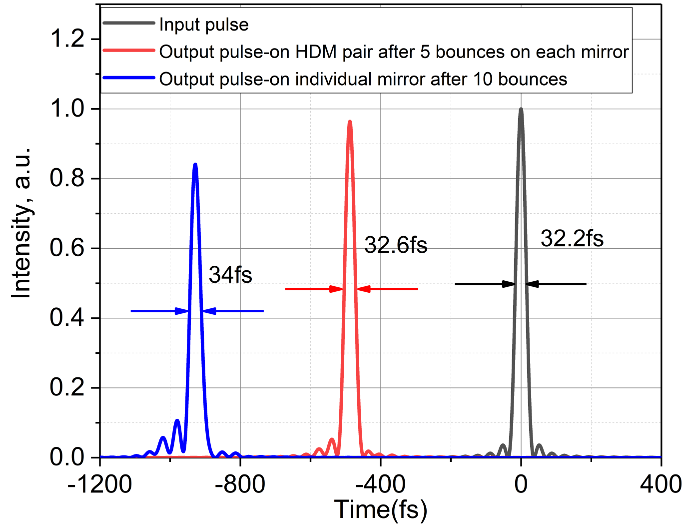

Figure 5.8: Input and output pulse simulations. The black curve shows the input pulse, the red and blue curves correspond to the output pulse after ten reflections from the HDM pair and the individual mirror, respectively.

5.2 One octave DM pair with smooth GDD characteristics based on non-uniformity

Attosecond pulses offer us tools to study electron dynamics in atoms [118], solids [119] and molecules [120]. The attosecond pulse generation relies on ultra-broadband few-cycle laser pulses in the visible/near infrared range [121–125]. Few-cycle laser pulses require perfect group delay dispersion (GDD) compensation over one octave range, which makes the ultra-broadband dispersive mirror [22, 24, 25] the only way to compensate the dispersion in such a wide spectral range.

However, the undesired GDD oscillations originating from the impedance mismatching between the mirror and the incident medium have always accompanied DMs. A DM with large GDD oscillations could broaden the pulse duration and introduce satellite pulses, which will severely damage the pulse quality. Moreover, the larger spectral bandwidth of the DM, the stronger GDD oscillations. Several single mirror methods [54, 62–64] have been proposed to suppress the GDD oscillations in the late 90s and early 21st century. However, these methods are not successful enough for the one octave spanning DM and their structures are very complex, which limit their applications.

Complementary DM pairs [22, 26, 29], double angle DM pairs [24] and wedge DMs [25] are the most effective approaches to suppress the undesired GDD oscillations over one octave. The former two methods utilize two mirrors with anti-phase GDD oscillations to

cancel each other and realize a smooth GDD. For the complementary DM pair, two coating runs are necessary which must be perfectly matched. The precision of the total thickness should be better than 0.1% from run to run. Higher deposition rate deviations will affect the spectral matching and result in an increased amplitude of the residual oscillations. Therefore, producing a complementary DM pair in two coating runs is much more difficult than producing a DM in a single coating run. Meanwhile, the double angle DM pair using two identical mirrors, which work at two different incident angles, could be produced in one coating run. Thus, the spectral matching is not a problem for double angle DM pair. The disadvantage of double angle DM pair is that they must be accurately aligned in order to meet the angles of incidence (AOI) of the coating design, which increase the time and difficulty for the alignment. Moreover, small deviations of the AOI could lead to the increase of GDD oscillations. Another disadvantage is that the GDD oscillations will be enhanced significantly at the other polarization, which makes it only work at one polarization. The wedge DM is a newly developed single mirror approach. It is composed of an AR coating, a wedged layer and a multilayer stack. The wedged layer introduces high frequent GDD oscillations which are spectrally shifted along the gradient of the wedge. The wedge DM is able to provide a low GDD oscillation with odd reflections. However, the production of this mirror is very complicated. It needs three different coating runs to coat the three parts. Any deposition errors in the three coating runs could increase the residual GDD oscillations significantly. Moreover, the total thickness of the wedge DM is more than 20 μm, which will result in severe stress issues. Considering the difficulties of the production between three different methods, the double angle DM pair is still the most widely used few-cycle dispersion compensator so far [24, 126–129]. However, the double angle DM pair only works at one polarization and works at two AOIs, making it more sensitive to the incident angle and polarization, which are still unsolvable.

In this section, a novel one octave DM pair based on the non-uniformity of the ion beam sputtering (IBS) coating process is designed, produced and characterized. The DM pair consisting of two mirrors with slightly different thickness, where the GDD oscillations are just in anti-phase, can be produced within one coating run by using the non-uniformity effect. The non-uniformity is known to be the variation of physical thickness along the deposition area. The non-uniformity of IBS is mainly dominated by the angular distribution of the sputtered particles. The distance between the target and substrates is a major parameter to adjust this distribution. Thus, the desired non-uniformity can be obtained by changing the distance between the target and substrates. The new DM pair works at the same AOI (5°), which has the advantages of working at both polarizations and a lower sensitivity to the incident angle compared to the well-known double angle DM pair. In addition, much less time would be necessary to align these new mirrors compared to the double angle DM pair. In order to prove these advantages, comparison between the new DM pair and the double angle DM pair, including the GDD characteristics and pulse analysis, was studied.

5.2.1 Design and production of the one octave DM pair

The new one octave DM pair is composed of two mirrors which have slightly different thicknesses. The anti-phase oscillations of the GDD are achieved by the spectral shift between the two mirrors due to the thickness differences. The physical thicknesses of two mirrors are proportional to each other, which means the thickness of the second one is related to the first one with a certain proportion. This proportion could be realized by the non-uniformity effect in the coating process.

The DM pair was designed by the special multi-coating function included in the Optilayer software [81]. In order to cover a wide-range from 500 nm to 1050 nm, Nb_2O_5 and SiO_2, which have a high refractive index ratio, were chosen as the layer materials. Suprasil was used as the substrate. The optical constants of the substrate and layer materials are specified by the Cauchy formula with the coefficients shown in Table 4.1.

Both mirrors were designated to work at an incident angle of 5°. The proportion of the second mirror to the first one was set to vary from 1.9% to 1%, which is achievable in the production by changing the distance between target and substrate. The optimal proportion could be obtained during the minimization of the merit function. The target reflectance was set to 100%. We choose to optimize the GD with the special floating constants method [130], which allows us to shift the GD values up and down to get the best design without changing the amount of GDD. This mirror is optimized to compensate the dispersion of 1 m air and 1 mm fused silica with two reflections. The $GD(\omega)$ can be integrated from the $GDD(\omega)$ with an additional arbitrary constant C:

$$\hat{GD} = \int_{\omega_o}^{\omega_1} GDD\left(\omega\right) d\omega + C \tag{5.2}$$

The corresponding GDD values are the same as for the double angle DM pair. The needle optimization [82] and gradual evolution [83] techniques were used to minimize the merit function to synthesize the design. The combined merit functions were described as follows:

$$MF\left(X,C\right)_{\Sigma}^{2} = \sum_{j=1}^{500}\left(\frac{R_{\Sigma}\left(X,\lambda_j\right) - R\left(\lambda_j\right)}{\Delta R_j}\right)^2 + \sum_{j=1}^{500}\left(\frac{GD_{\Sigma}\left(X,\lambda_j\right) - \hat{GD}\left(\lambda_j\right)}{\Delta GD_j}\right)^2 \tag{5.3}$$

where $\{\lambda_j\}$ are evenly distributed wavelength points in the spectral range from 500 to 1050 nm; $\{X\}$ includes $\{X_1\}$ and $\{X_2\}$, which are the vectors of layer thickness of the first mirror and the second mirror of the DM pair; R_Σ is the geometric mean of R_1 and R_2, which are the reflectance of the first and the second mirror, while GD_Σ is the arithmetic mean of GD_1 and GD_2, which are the GD of the first and the second mirror; $R\left(\lambda_j\right)$ and $\hat{GD}\left(\lambda_j\right)$ are the reflectance and GD target, where $R\left(\lambda_j\right)$ equals 100%, $\hat{GD}\left(\lambda_j\right)$ equals $\hat{GD}\left(\omega\right)$ and therefore includes the constant C; ΔR and ΔGD are tolerances of reflectance and GD.

During the optimization, carefully adjusting the tolerances of the reflectance and GD is necessary. A one octave DM pair was synthesized finally. The layer thicknesses and

theoretical curves are shown in Figure 5.9 and 5.10, respectively. One can clearly see the slight thickness difference between the first and second mirror from Figure 5.9. Due to this thickness difference, the GD and GDD oscillations of the two mirrors are exactly in anti-phase, as shown in Figure 5.10. The first and second mirror were named as PC70-modified-3 and PC70-modified-5. The final proportion of PC70-modified-3 to PC70-modified-5 is 1.8%. The proportion corresponds to the non-uniformity during the production process.

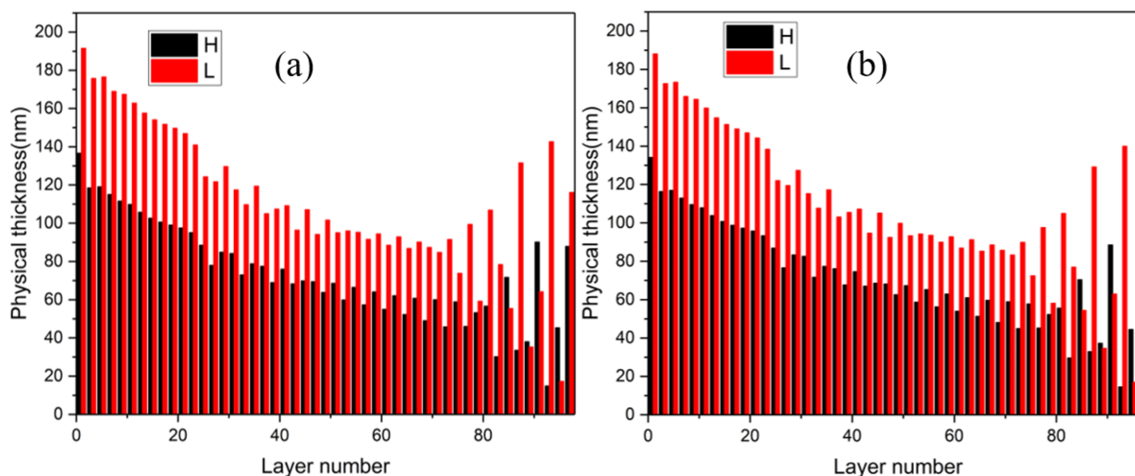

Figure 5.9: Layer thickness structure of the two designs; (a) and (b) correspond to the first and second design. The proportion is 1.8%. Black and red bars represent the high and low index materials, respectively.

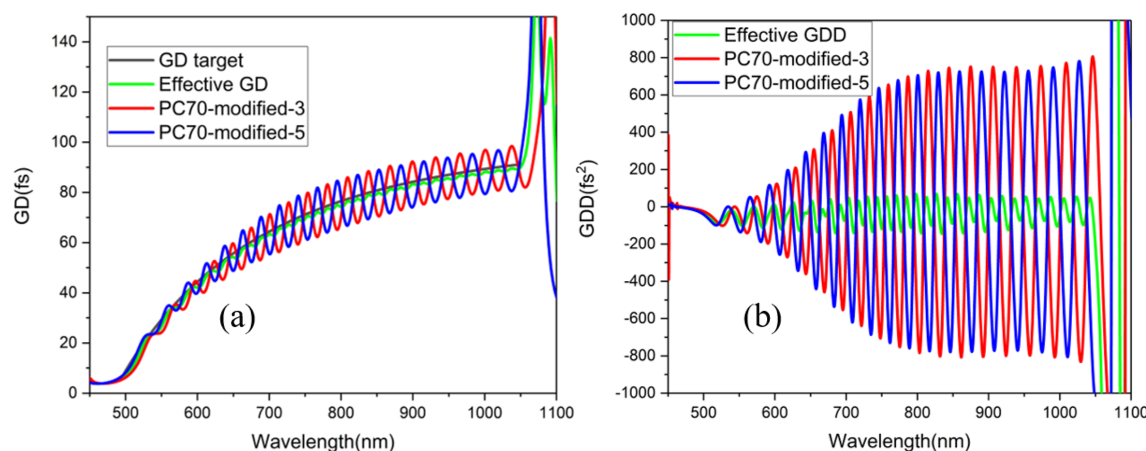

Figure 5.10: GD and GDD characteristic of the one octave DM. (a) theoretical GD, (b) theoretical GDD. Red and blue curves represent the first and second design named as PC70-modified-3 and PC70-modified-5.

For ion beam sputtering the angular emission distribution for sputtered atoms from the target is often described as an under-cosine or heart shape distribution [115]. Due to

such a distribution, the desired non-uniformity could be obtained by changing the distance between target and substrate, which in our case is to adjust the substrate height. In order to get 1.8% non-uniformity, we produced single Nb_2O_5 and SiO_2 layers and Quarter-wave multilayer coatings with different substrate heights. The transmittance spectra were used for reverse engineering to calculate the non-uniformity. Finally, the optimal substrate heights, which were -35 mm for Nb_2O_5 and -50 mm for SiO_2 material, were obtained to realize 1.8% non-uniformity between the third ring and fifth ring in the substrate fixture, which is illustrated in Figure 5.11. The transmittance spectra of single Nb_2O_5 and SiO_2 layers as well as a multilayer filter were depicted in Figure 5.12.

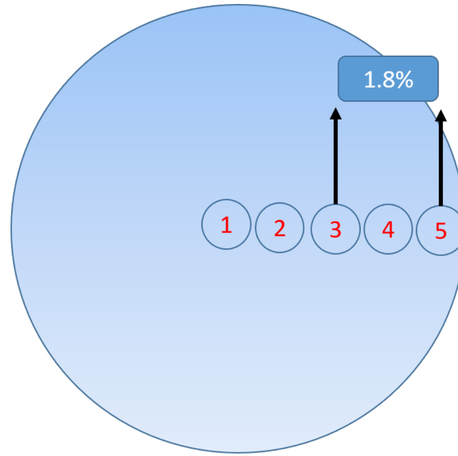

Figure 5.11: The schematic picture of the substrate holder with the desired non-uniformity.

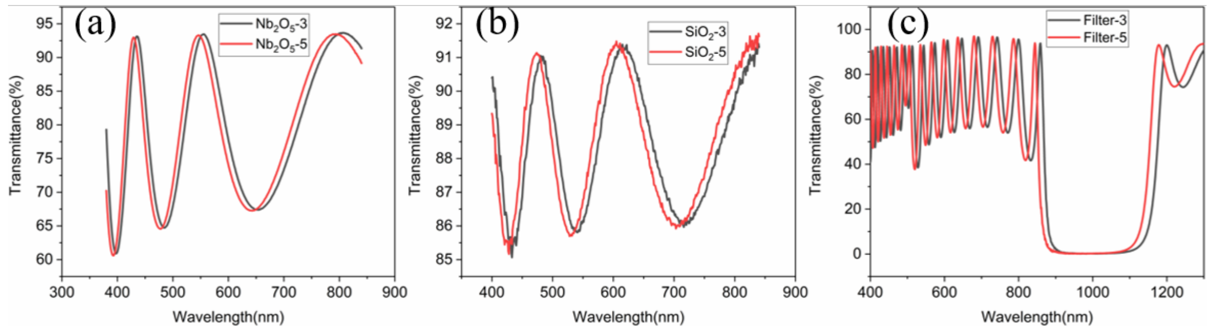

Figure 5.12: Transmittance spectra of single Nb_2O_5, SiO_2 layers and a multilayer filter.

After the desired non-uniformity was obtained, we started to deposit the one octave DM pair. Two fused silica substrates were put at the third ring and fifth ring in the substrate fixture with the correct substrate heights. The DM pair was produced with the ion beam sputtering from Cutting Edge Coatings GmbH (Hannover, Germany). The ion beam is extracted from an Argon gas plasma by a three-grid multi-aperture extraction system. A cryogenic pump evacuates the coating chamber to 1×10^{-7} mbar before deposition. The

pressure during the coating process is about 5×10^{-4} mbar. Due to stable sputtering rates, the layer thickness is controlled by time. The IBS coating machine is also equipped with a broadband optical monitoring system, which allows us to monitor the in-situ transmittance. The deposition rates of Nb_2O_5 and SiO_2 materials were approximately 0.1 nm/s and 0.13 nm/s, respectively.

After the production, a load-lock was used to unload the samples without venting the coating chamber. The samples located in the third and fifth ring were named as PC70-modified-3 and PC70-modified-5, respectively. The transmittance of both samples was measured by a Perkin-Elmer Lambda 950 spectrophotometer at normal incidence, which is plotted in Figure 5.13. A great agreement between the measured and theoretical data of both mirrors can be observed from Figure 5.13. Moreover, the spectral shift of the measured transmittance between two mirrors is exactly the same to the theoretical spectral shift, which proves that the 1.8% non-uniformity is realized based on the current coating parameters. The GD and GDD were measured by a home-built white light interferometer [100]. The measured GD and GDD compared to the theoretical curves are presented in Figure 5.14. One can see that the measured GD and GDD of PC70-modified-3 and PC70-modified-5 are just in anti-phase and cancel each other. The effective GD and GDD oscillations have been decreased significantly. Great agreement between the measured and theoretical GD and GDD was obtained, as can be seen in Figure 5.14.

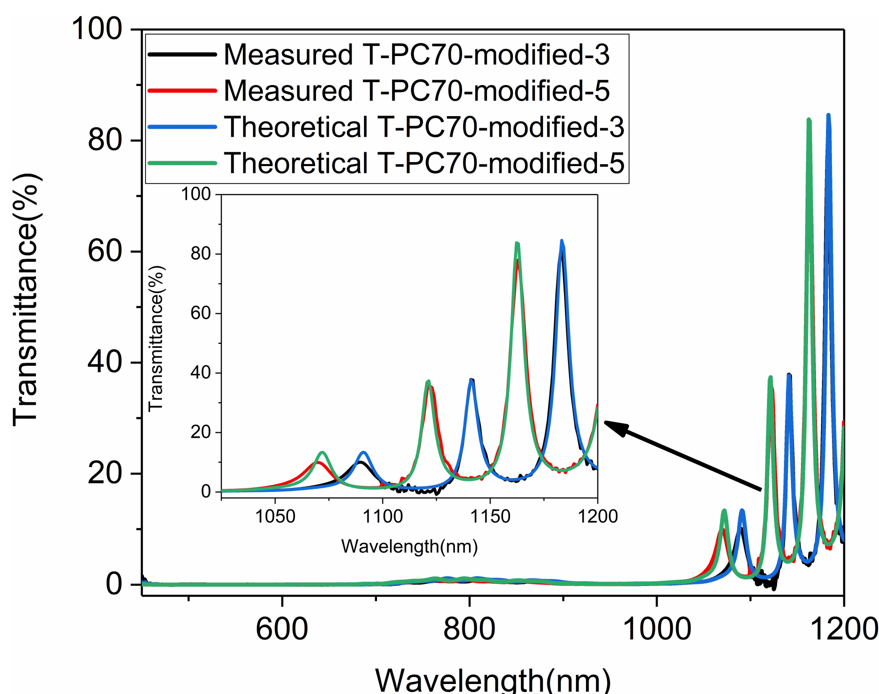

Figure 5.13: Comparison of measured transmittance and theoretical transmittance of the two mirrors. Black and red curves represent the measured transmittance, while blue and green curves correspond to the theoretical transmittance.

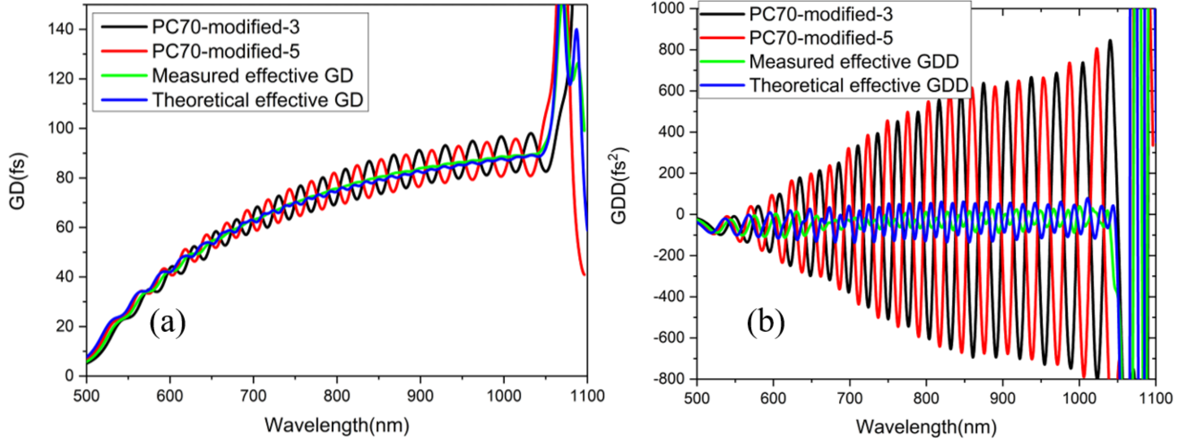

Figure 5.14: Measured GD and GDD compared to the theoretical values. (a) GD, (b) GDD. Black and red curves represent PC70-modified-3 and PC70-modified-5, respectively. Green and blue curves represent measured and theoretical curves.

5.2.2 Comparison of the one octave DM pair with double angle DM pair

In order to verify the advantages of our new DM pair, comparisons of the DM pair to the well-known double angle DM pair were studied, which include GDD characteristics and pulse analysis. On the purpose of simplifying the names of the two different DM pairs, the double angle DM pair and the new DM pair were named as PC70 and PC70-modified, respectively.

5.2.2.1 GDD characteristics

The GDDs of PC70 and PC70-modified were measured with a white light interferometer at the designed angles of incidence (AOI) and polarization, which are 5° & 19° and 5° for p-polarization, respectively. The results are shown in Figure 5.15. One can clearly see that both curves are quite close, which means at the designed AOI and polarization both mirrors have comparable GDD characteristics. Furthermore, the GDDs of both mirrors were also measured for the s-polarization, which were plotted in Figure 5.16 (a) and 5.16 (b). For the PC70, the GDD oscillations at s-polarization have been enhanced significantly compared to the p-polarization, while for the PC70-modified, the measured GDDs are almost identical for both polarizations. It proves that the PC70-modified could work at both polarizations, while PC70 is only able to work at one polarization and is sensitive to the polarization.

Additionally, in order to study the sensitivity of the GDDs to the incident angle, the GDDs of PC70 were measured at two degrees deviations to the designed AOI, which are 5° & 21° and 7° & 19°, respectively. Meanwhile, the GDDs of PC70-modified were measured at the incident angle of 3° and 7°. The results compared to the measured GDDs at the designed AOI are presented in Figure 5.17. For the PC70, the GDD oscillations increase

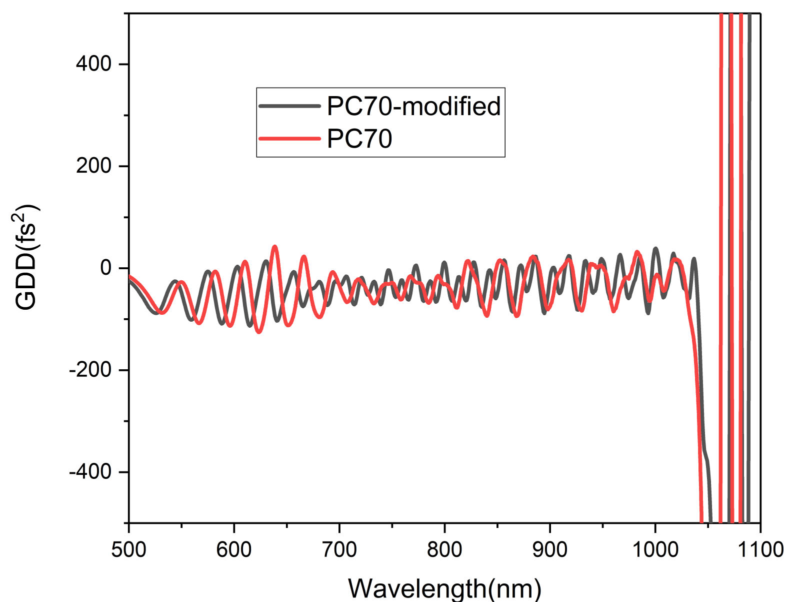

Figure 5.15: Measured GDD at the designed incident angle and polarization. Black and red curves represent PC70-modified and PC70, respectively.

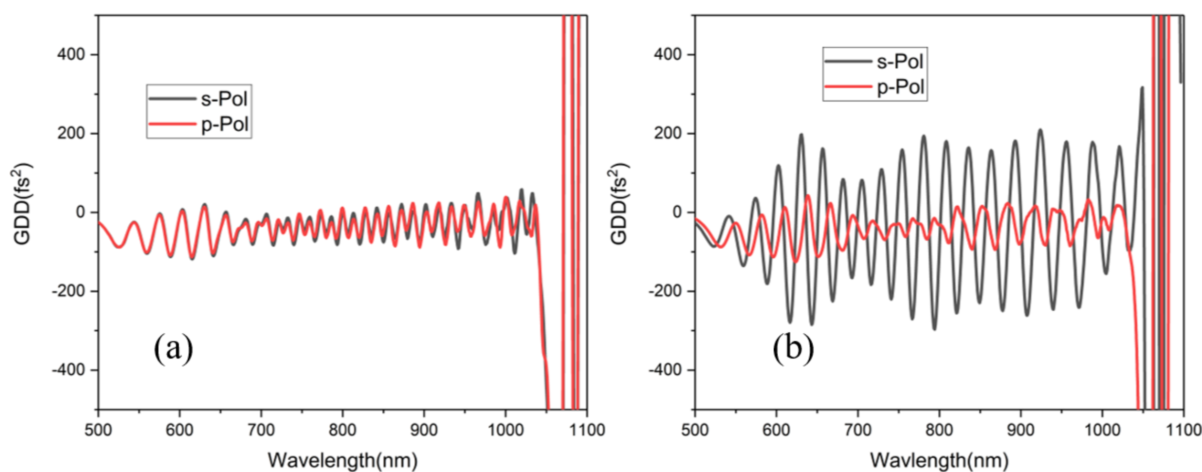

Figure 5.16: Measured GDD at both polarizations. (a) PC70-modified, (b) PC70. Black and red curves represent s polarization and p polarization.

a lot even though there are only two degree deviations, while for the PC70 modified, the measured GDDs at AOI of 3° and 7° are almost the same, and there is only a few nm spectral shift. Figure 5.17 show great evidence that the PC70-modified is much less sensitive to the incident angle than PC70.

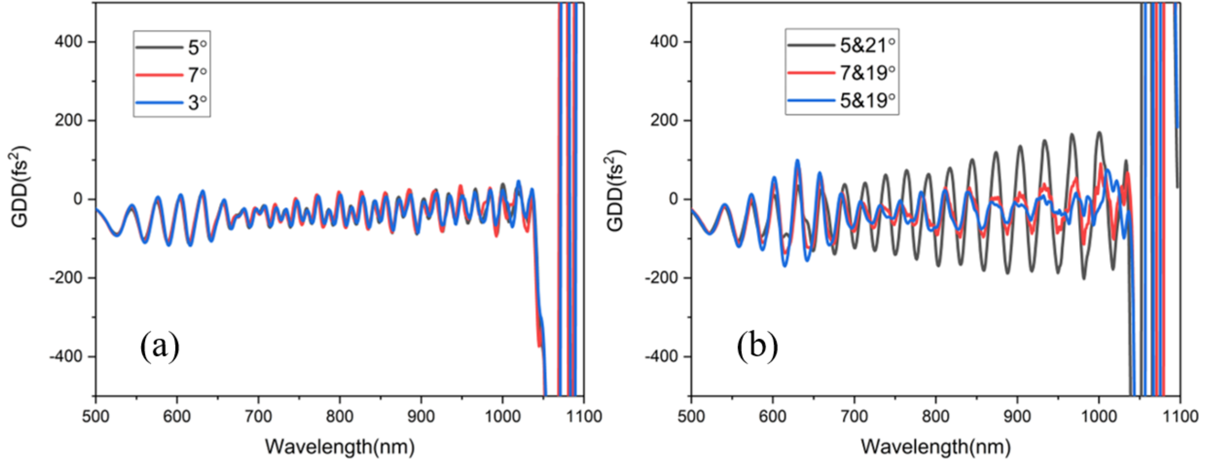

Figure 5.17: Measured GDD at different AOI. (a) PC70-modified, (b) PC70.

5.2.2.2 Pulse analysis

In order to further compare these two DM pairs, we simulated the pulse envelopes reflected from PC70 and PC70-modified under different conditions. During the simulations, we assume that the input pulse is a Fourier transform limited pulse with a pulse duration of 3.47 fs and a super-Gaussian spectrum with a full width of half maximum (FWHM) of 500 THz covering 500 to 1050 nm, which is exactly the working range of these mirrors. The input pulse was sent to an imaginary black box which has 10 times the amount of the target dispersion with opposite sign. Then the stretched pulses were re-compressed by the PC70-modified and PC70 with 10 bounces, respectively.

We first simulated the pulse envelopes after 10 bounces on the PC70-modified and PC70 at the designed AOI for both p-pol and s-pol. The results are shown in Figure 5.18 (a) and 5.18 (b), respectively. As we can see from Figure 5.18 (a), the pulse envelopes and pulse duration almost keep unchanged for both polarizations, while Figure 5.18 (b) shows that the pulse envelope reflected from PC70 does not change for p-pol, but the pulse envelope for s-pol changes significantly. The pulse duration has been broadened to more than 5 fs and the intensity has decreased by 45% due to the satellite. The simulations prove that the PC70-modified works at both polarizations, while PC70 works at only one polarization.

The pulse envelopes reflected from PC70-modified and PC70 at two degree deviations to the designed AOI were also simulated. In Figure 5.19 (a) and 5.19 (b), the simulated envelopes of input pulse and output pulses are presented. For the PC70-modified, the output pulses at the incident angle of 3°, 5° and 7° are almost the same to the input pulse. The pulse duration was only stretched by 0.04 fs at most after 10 bounces. For the PC70, the pulse duration at the incident angle of 7° & 19° and 5° & 21° was stretched larger than the PC70-modified, especially at the angle of 5° & 21°, the pulse intensity has decreased by more than 20% and the pedestal effect becomes more significant. The pulse simulations show that the pulse quality including pulse duration and pulse intensity reflected from the PC70, is much worse than the pulse quality reflected from the PC70-modified at the same

two degree deviations to the designed AOI, which verify that the PC70-modified is less sensitive and more robust to the AOI than the PC70.

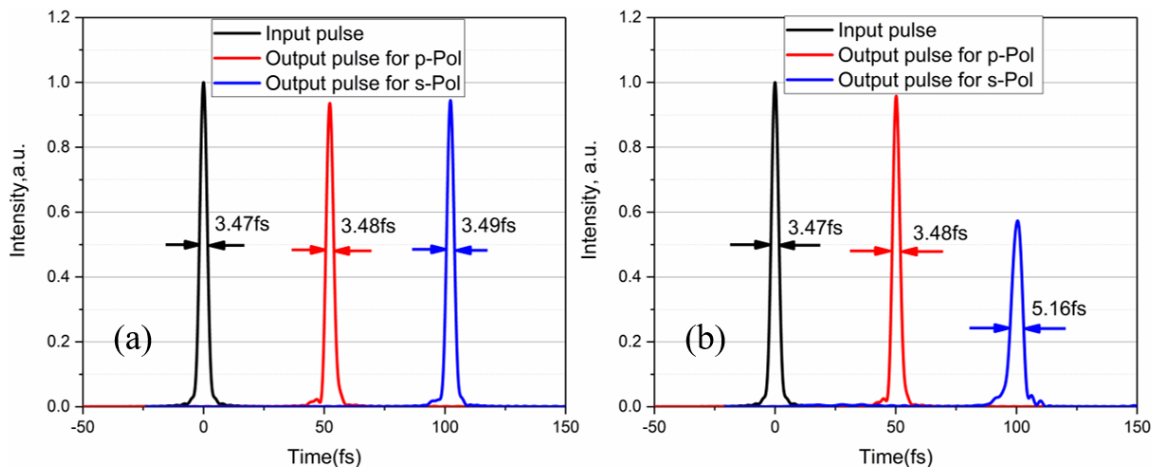

Figure 5.18: Input and output pulse simulations. (a) PC70-modified, (b) PC70. Black, red and blue curves represent the simulated input pulse, output pulse for p-pol and output pulse for s-pol, respectively.

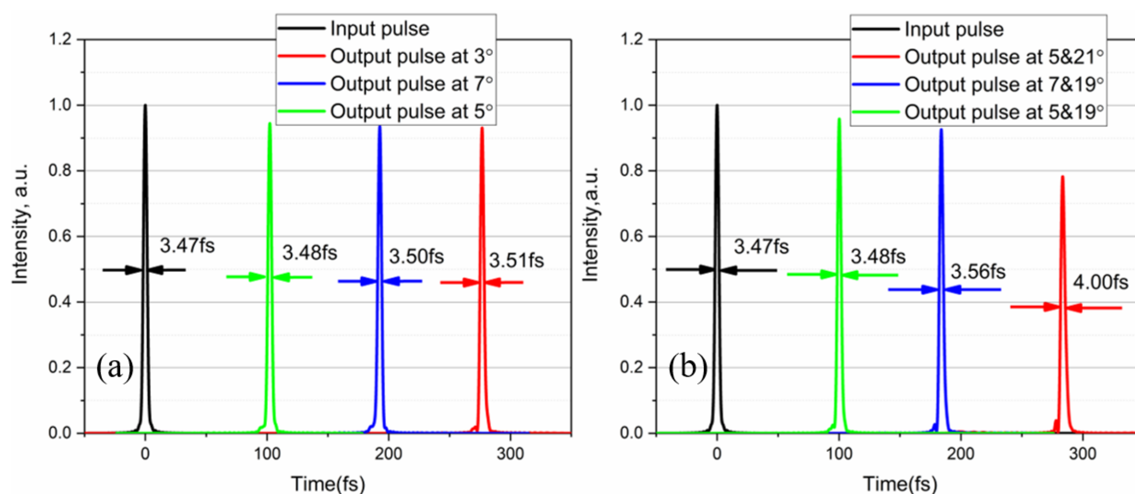

Figure 5.19: Input and output pulse simulations. (a) PC70-modified, Black green, blue and red curves represent the simulated input pulse, output pulse at AOI of 5°, output pulse at AOI of 7° and output pulse at AOI of 3°; (b) PC70. Black green, blue and red curves represent the simulated input pulse, output pulse at AOI of 5° & 19°, output pulse at AOI of 7° & 19° and output pulse at AOI of 5° & 21°.

5.2.3 Conclusions

A new DM pair which was able to compensate the dispersion of 1 m Air and 1 mm fused silica over one octave has been successfully designed, produced and characterized. The DM pair composed of two mirrors with slightly different thickness, where the GDD oscillations are just in anti-phase, was realized within one coating run based on the adjustable non-uniformity. Comparison of the new one octave DM pair with the double angle DM pair regarding GDD characteristics and pulse analysis has been done, which proved the advantages of the new DM pair. The new DM pair works at one AOI and is much easier to implement in the laser system. Moreover, it is less sensitive and more robust to the AOI than the double angle DM pair. Most importantly, it works at both polarizations, while the double angle DM pair only works at one polarization.

Chapter 6

3-6 μm dispersive mirrors compensating the dispersion introduced by the GaAs crystal

Dispersive mirrors (DMs) which provide precise group delay dispersion (GDD) compensation have been successfully used in the visible [34–37, 55] and near infrared range [21, 21, 29, 39–42, 45, 131]. It includes Ti:Sa lasers [34–37, 55], Yb:YAG lasers [21, 39, 40, 45], Erbium-doped fiber lasers [41] and Cr:ZnS/Cr:ZnSe lasers [21, 29, 42, 131]. DMs in this range have been improved further and further and are now commercially available. The mid-infrared (MIR) fingerprint region where molecules have their distinct absorption features associated with ro-vibrational transitions is critical for high-resolution spectroscopy, trace molecular sensing, and chemical standoff detection [66, 132, 133]. As more scientists are attracted towards MIR laser systems, the demand of corresponding dispersion compensation elements is growing. Broadband DMs operating in the spectral range from 6.5 to 11.5 μm were successfully developed and applied in a broadband MIR field resolving spectrometer [27]. In [53], a DM providing a group delay (GD) variation of 60 fs with an average reflectance of 97.5% in the spectral range from 9 to 11.5 μm was synthesized. DMs in this region have become a key element to compensate dispersion.

The extension of the frequency comb to the mid-infrared enables exciting applications such as coherent molecular spectroscopy and trace gas detection [132, 134], attosecond physics [135], and laser-driven particle acceleration [136]. Optical parametric oscillators (OPO) are one of the key components to realize the extension of the frequency comb to the mid-infrared fingerprint region. An orientation-patterned (OP)-GaAs crystal, which has a large second-order nonlinear optical coefficient and good MIR transparency, makes it very suitable for MIR optical parametric frequency conversion. However, to the best of our knowledge, in most of the published works [137–140], the dispersion of the GaAs crystal was compensated by CaF_2 or YAG plates. The dispersion was not perfectly compensated in a wide range, since the dispersion of GaAs and CaF_2 or YAG do not match each other exactly, which results in large residual dispersion. It limits the achievable pulse duration and spectral bandwidth [137–139].

In this chapter, for the first time, a new DM composed of Si and SiO_2 layers, which can compensate the dispersion of a 0.5 mm GaAs crystal in the spectral range of 3 to 6 μm was designed, fabricated and characterized. The refractive indices of Si and SiO_2 were determined by measuring the transmittance and reflectance spectra of the single layers and quarter wave multilayer. The design and production of the MIR DM are shown in section 6.2. In section 6.3, the characterization of the DM and pulse simulations compared to the CaF_2 are described. We draw our conclusions and outlook in section 6.4.

6.1 Determination of the refractive indices of the layer materials

In order to design a mid-infrared DM spanning over one octave, which could compensate the dispersion introduced by a 0.5 mm GaAs crystal, a proper material combination must be chosen. As we know, due to the relatively low refractive index ratio and absorption problem, the widely used thin film materials for the visible and near infrared range are no longer suitable for the mid infrared range. Si and SiO_2 with a higher refractive index ratio of about 2.3 have proven to be very successful in a 2 to 4 μm DM [21, 29]. In this work, Si and SiO_2 were considered as the high and low index materials.

The refractive indices of Si and SiO_2 were determined from single Si and SiO_2 layers as well as a Si/SiO_2 quarter-wave mirror. A single Si layer was deposited on a fused silica substrate with a temperature of 180 ℃ by ion beam sputtering. After the production, the transmittance, reflectance, and back side reflectance were measured by a Perkin Elmer Lambda 950 spectrophotometer, respectively. The refractive index was determined by the well-known Cauchy model, while the extinction coefficient was defined by the non-parameter approach [141, 142] based on the following discrepancy function:

$$DF^2 = \sum_{j=1}^{L} \{S(n(\lambda_j), k(\lambda_j), d, \lambda_j - S(\lambda_j))\}^2 + \alpha_1 \sum_{j=1}^{L} \{n''(\lambda_j)\}^2 + \alpha_2 \sum_{j=1}^{L} \{k''(\lambda_j)\}^2 \quad (6.1)$$

where $S(n(\lambda_j), k(\lambda_j), d, \lambda_j)$ is the theoretical spectral characteristic of the sample, $S(\lambda_j)$ is the measured spectral characteristic, $n''(\lambda_j)$ and $k''(\lambda_j)$ are the finite-difference second order derivatives of the refractive index and extinction coefficient, α_1 and α_2 are the weight parameters. Calculation of the refractive indices and extinction coefficient was performed with OptiRe software. The optical constants of Si are shown in Figure 6.1 (a). In Figure 6.1 (b), a great agreement between the experimental data and model data can be observed.

A single SiO_2 layer was deposited on a Ge substrate with a temperature of 180 ℃. The transmittance and reflectance were measured by the Perkin Elmer Lambda 950 spectrophotometer in the wavelength range from 400 to 2600 nm. The spectra beyond 2600 nm were measured by a Bruker Fourier Transform Infrared spectrometer (FTIR, Vertex 70, Bruker Optics GmbH). The dispersion behavior of the SiO_2 refractive index was described by the Cauchy model, the extinction coefficient was described by the non-parameter approach.

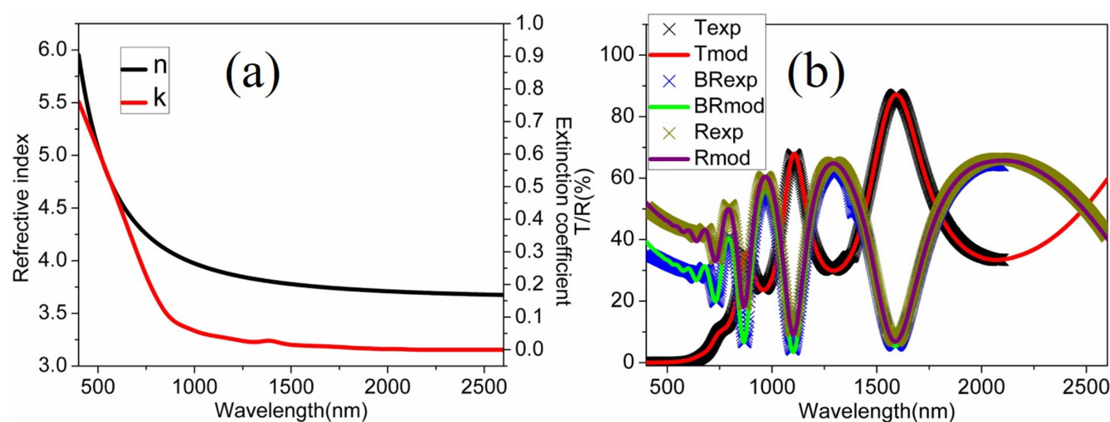

Figure 6.1: (a) Determined optical constant of Si layer, (b) Fitting of measured transmittance and reflectance data of Si layer by the model data.

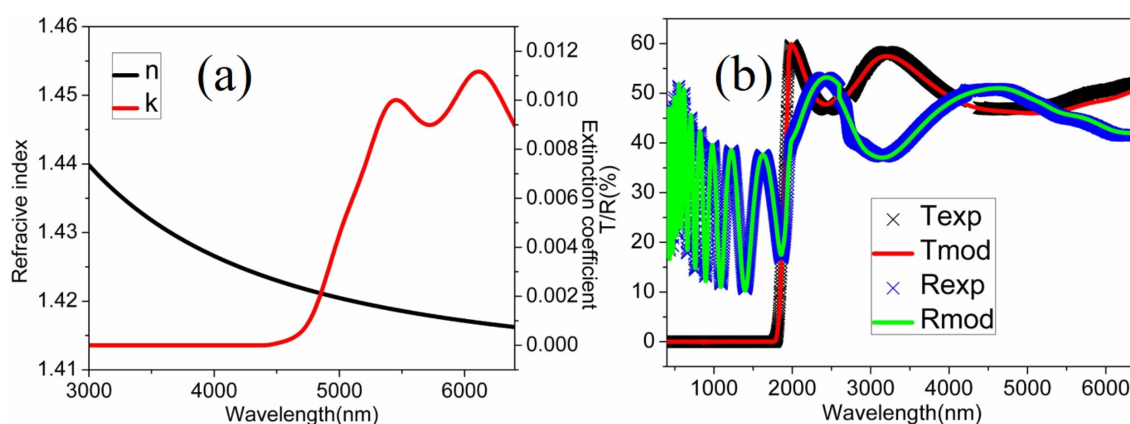

Figure 6.2: (a) Determined optical constant of SiO_2 layer, (b) Fitting of measured transmittance and reflectance data of SiO_2 layer by the model data.

The optical constants are plotted in Figure 6.2 (a). The experimental data show a great agreement to the model data, which is shown in Figure 6.2 (b).

A quarter-wave mirror with a central wavelength of 4100 nm was deposited on a fused silica substrate with a temperature of 180 ℃ to calibrate the deposition rates and verify the refractive indices in the multilayer structure. The reflectance was recorded by a FTIR spectrometer. Based on the OptiRe software, the deposition rates were calibrated by reverse engineering. The experimental reflectance compared to the model reflectance is presented in Figure 6.3. A good correspondence between the measurement and the model was obtained.

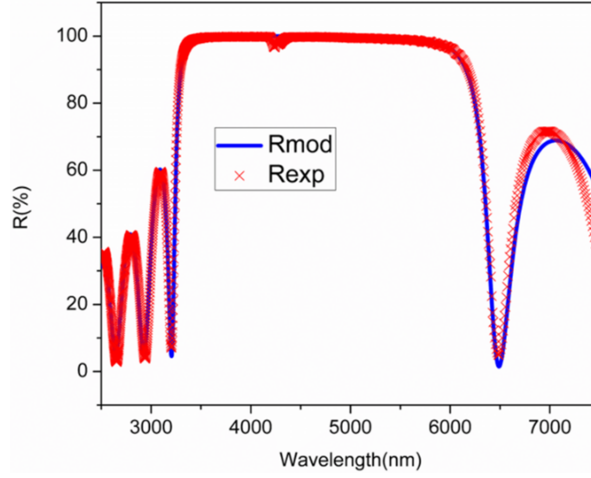

Figure 6.3: Correspondence between the experimental and model reflectance.

6.2 Design and production of the DMs

After determining the refractive indices of both materials, we started to design the DM. The OptiLayer software [81] with powerful needle optimization and gradual evolution algorithms was used in the design process. The reflectance and GD were chosen as the target characteristics. The target GD was the GD of a 0.5 mm GaAs crystal with the opposite sign and shifting in the vertical direction, while the target reflectance was 100%. The target GD value at the wavelength of 4500 nm is 59 fs and the GD difference between 3000 and 6000 nm is about 60 fs. The merit function was defined as:

$$MF(X)^2 = \sum_{j=1}^{520} \left(\frac{R(X, \lambda_j) - R(\lambda_j)}{\Delta R_j} \right)^2 + \sum_{j=1}^{520} \left(\frac{GD(X, \lambda_j) - GD(\lambda_j)}{\Delta GD_j} \right)^2 \tag{6.2}$$

where $\{\lambda_j\}$ are distributed wavelength points in the spectral range of 3000 to 6000 nm; $X = (d_1, \ldots, d_m)$ is the vector of the layer thicknesses, m is the layer number; $R(X, \lambda_j)$ and $GD(X, \lambda_j)$ are the actual reflectance and GD; $R(\lambda_j)$ and $GD(\lambda_j)$ are the reflectance and GD target, while ΔR_j and ΔGD_j are the tolerance of reflectance and GD.

A DM which is able to compensate the dispersion of a 0.5 mm GaAs crystal per bounce was obtained, after carefully adjusting the tolerance and optimizing the design. The layer structure is shown in Figure 6.4 (a). The total thickness is about 9.7 μm, which is not very thick considering that this mirror works in the MIR range. The theoretical reflectance, GD as well as an error analysis are plotted in Figure 6.4 (b). Layer thicknesses were randomly varied with a relative error of 2% and an absolute error of 2 nm, which are much larger than the real deposition errors. For each design we computed the GD and performed a statistical analysis of the obtained GD dependencies. The red and green curves in Figure 6.4 (b) define the border of errors that encloses GD values with a probability of 68.3%. Based on the computational error analysis, we could study the sensitivity of the DM to deposition errors. Figure 6.4 (b) shows that even with a 2% relative error and a 2 nm

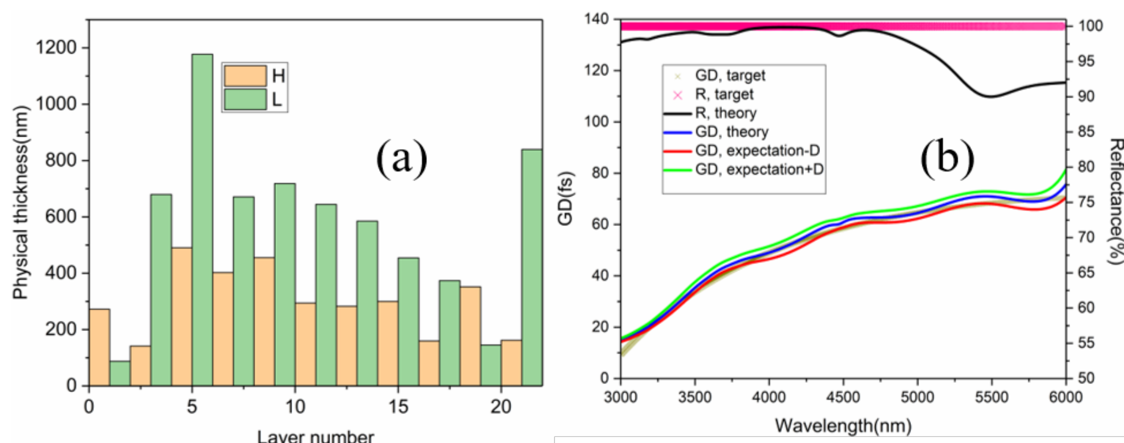

Figure 6.4: (a) Layer structure of the DM. Yellow and green bar represent high and low index materials. The layer number is starting from the substrate to the incident medium (air), (b) Theoretical reflectance and GD. Pink and yellow cross represent R and GD target. Black and blue curves represent the theoretical R and GD. Red and green curves represent the probability corridor for a 2% relative error and a 2 nm absolute error.

absolute error, the GD curves only have a small deviation to the theoretical GD curve and fit well to the GD target. This means the DM is quite robust to the layer thickness errors.

The 3-6 μm DM was fabricated with ion beam sputtering (Cutting Edge Coatings, Hannover, Germany). To reduce the absorption of both materials, the substrates were heated to 180 ℃ for two hours before deposition by two quartz radiation heaters. The chamber was pumped down to 1×10^{-7} mbar by a cryogenic pump. The Argon gas plasma is generated by a radio-frequency ion source. Both Si and SiO_2 were sputtered from a silicon target with a purity of 99.999%. During the Si layers, no oxygen was added to the coating chamber. While for the SiO_2 layers, the amount of 90 standard cubic centimeters per minute (sccm) was ejected near the pure Si target. The thickness was controlled by a well-calibrated time control technique. The deposition rates for Si and SiO_2 were 0.13 nm/s and 0.15 nm/s, respectively.

6.3 Characterization of the DMs

After the deposition, reflectance data were measured by the FTIR in the wavelength range from 2500 to 6500 nm. Comparison between measured and theoretical reflectance is shown in Figure 6.5. The reflectance degradation around 4300 nm is due to water absorption. It should be noted that this water absorption dip does not affect the phase performance of the laser system [27]. In addition, the water absorption around 4300 nm does not affect the GD and GDD measurement. The GD and GDD were recorded by a MIR white light interferometer built in-house [101], which is also based on the FTIR. The measured GD

and GDD compared to the theoretical values were plotted in Figure 6.6. A good agreement between the measured and theoretical GD and GDD data could be observed. The measured GD and GDD curves are fitting very well to the theoretical ones. Especially for the GD curves, the steep increase beyond 6 μm and the GD difference between 3 and 6 μm of about 60 fs could be measured.

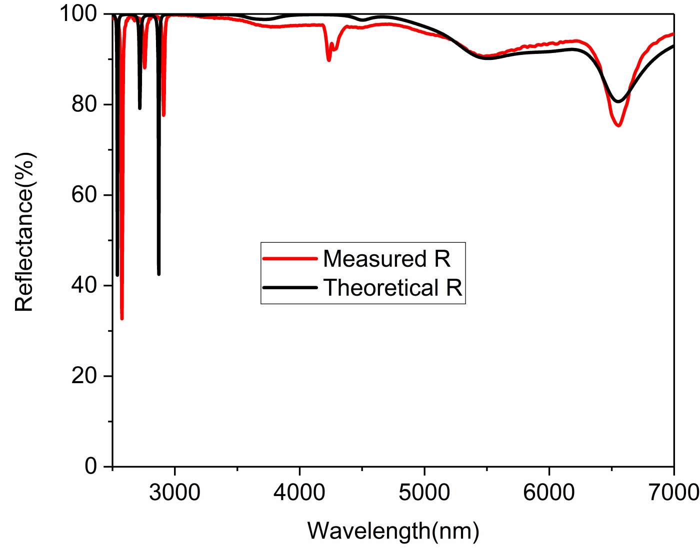

Figure 6.5: Comparison between the measured and theoretical reflectance. Black and red curves correspond to the measured and theoretical reflectance.

In order to compare the compensation effect between the MIR DM and CaF_2, which is commonly used to compensate the dispersion of GaAs, we simulated the envelopes of input and output pulses, which were compensated by the DM and CaF_2, respectively. During the simulations, we assumed that the input pulse was a Fourier transform limited pulse with a pulse duration of 18.8 fs and a full width at half maximum (FWHM) of 500 THz covering 3 to 6 μm. The input pulse first went through a 0.5 mm thick GaAs crystal. The stretched pulse was compressed by the DM and a 0.3 mm thick CaF_2, respectively. The simulated input pulse and output pulse are shown in Figure 6.7.

From the simulations, we could see that the pulse duration and pulse shape do not change at all after one and four bounces from the DM (blue and red curves in Figure 6.7). The pulse intensity only drops a little bit. Additionally, there are no satellites observed. On the contrary, the pulse shape which is compressed by CaF_2 has been changed significantly after passing one and four times through it (green and pink curves in Figure 6.7). The pulse durations have been increased to 19.4 fs and 29.2 fs after one and four times through the CaF_2. The intensity of the main pulse decreases drastically due to the appearance of the satellites. What's worse, the more times passing through the CaF_2, the longer the pulse duration and the worse the pulse quality. These simulations have proven that the dispersion introduced by the GaAs crystal could be perfectly compensated by the DM. While the compensation effect from the CaF_2 plate is much worse than the DM.

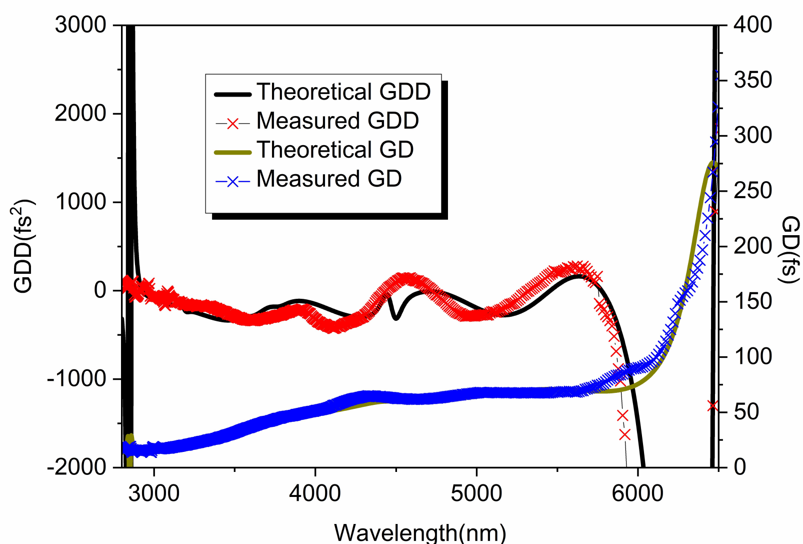

Figure 6.6: Comparison between measured and theoretical GD and GDD. Yellow and black curves represent the theoretical GD and GDD, blue and red crosses correspond to the measured GD and GDD.

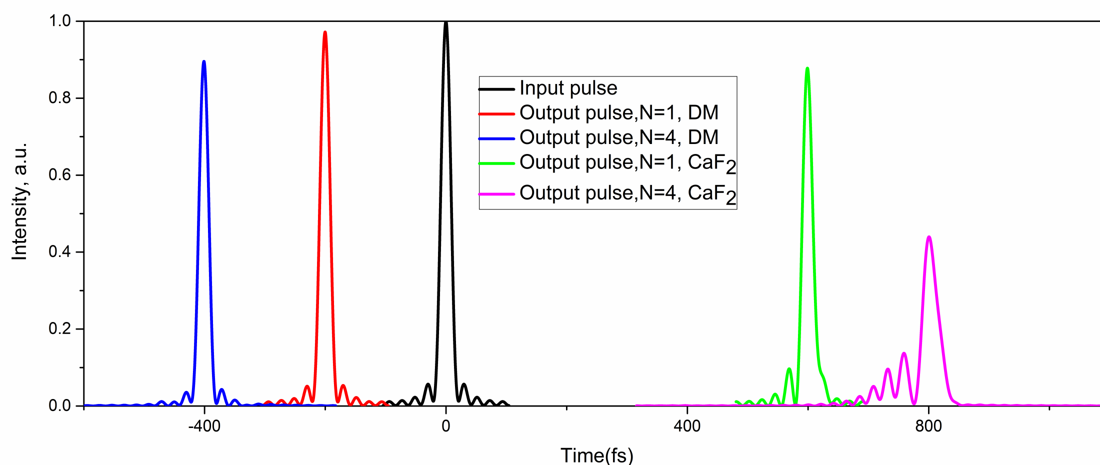

Figure 6.7: Simulated input and output pulses. Black curve represents the input pulse. Red and blue curves correspond to the output pulses which are reflected from the DM with one and four bounces, respectively. Green and pink curves correspond to the output pulses which are compensated by 0.3 mm CaF_2 with one and four times, respectively.

6.4 Conclusions and outlook

A new broadband DM which could perfectly compensate the dispersion of a 0.5 mm GaAs crystal in the spectral range of 3 to 6 μm has been successfully designed and produced

by ion beam sputtering for the first time. Pulse simulations show that the compensation effect of the DM is much better than the commonly used CaF_2 plates. This new type of DM could perfectly compensate the dispersion of a GaAs crystal, which will benefit the MIR OPO output spectrum, including better pulse quality and shorter pulse duration.

However, the water absorption around 4.3 μm results in the reflection dip. Such reflection dip will degrade the performance of the DM as the bounces on the DM increased. Further coating process modification should be done to avoid the water absorption in the future.

Chapter 7

Production of multilayer coatings with large substrates

The straightforward way to bypass the weak point of low damage threshold for multilayer coatings and achieve a higher intensity laser is to increase the beam size of the laser system, which requires coatings with large-scale. HR coatings with large-scale are not only able to support large beam size reflection but multiple reflections with small beam size, which can be used as end mirrors for multi-pass cell nonlinear pulse broadening. Compared to the HR coatings, CMs have even lower damage threshold due to the local electric field enhancement in the CMs structure [143–145]. The laser induced damage threshold can be improved by optimizing the electric field (E-field) [146,147] or replacing the layer which has the E-field maximum with larger band gap and higher laser resistant material [148, 149]. However, neither way seems easy and increases the damage threshold significantly. The straightforward approach is to increase the substrate size so that the energy density will be lower on the coating surface. In this chapter, the production of 300×130 mm rectangular HR coatings and 200 mm in diameter chirped mirrors are presented.

7.1 300 × 130 mm rectangular HR coatings

In order to design a HR coating with high damage threshold and low loss, HfO_2 and SiO_2 were considered as the high and low refractive index materials, which were specified by the Cauchy equation, where the coefficients were shown in Table 7.1. A HR coating was synthesized to provide a reflectance of >99.9% from 970 nm to 1100 nm for normal incidence. The GDD value is close to zero at 1030 nm and the maximum GDD is smaller than ± 50 fs^2 from 970 nm to 1100 nm. The HR coating is composed of 38 quarter-wave optical thickness layers, corresponding to the wavelength 1030 nm, except the last layer with half-wave optical thickness, which is intended to shift the maximum electric field from the interface to the first silica layer. With such electric field optimization, the laser resistance of the HR coating will be enhanced. The thickness structure and theoretical curves are shown in Figure 7.1.

Material	A_0	$A_1(\mu m^2)$	$A_2(\mu m^4)$
SiO_2	1.486272	-3.996783e^{-3}	5.8433165e^{-4}
HfO_2	1.981802	1.0719327e^{-2}	5.715660e^{-4}

Table 7.1: Cauchy formula coefficients for HfO_2 and SiO_2.

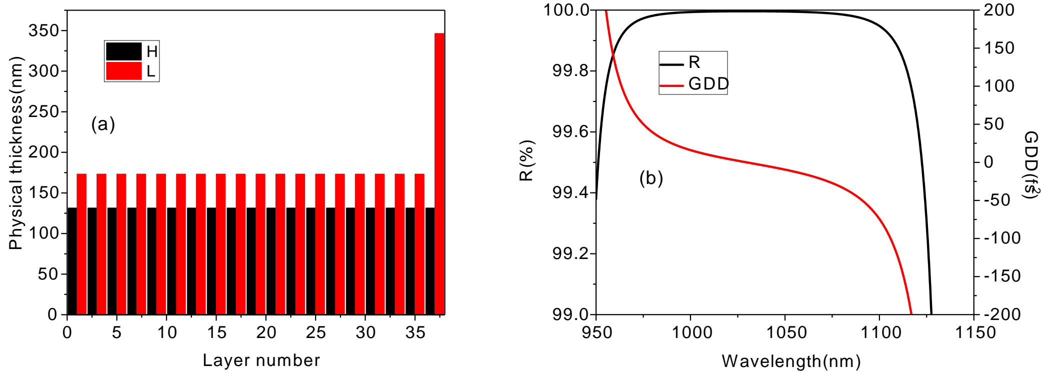

Figure 7.1: (a) Layer thickness structure of the HR coating. (b) Theoretical reflectance and GDD of the HR coating.

Prior to produce the 300×130 mm rectangular HR coating, a special designed substrate holder was developed, which is shown in Figure 7.2. The center of the substrate is exactly located at the center of the holder. The substrate is put in such a way perpendicular to the radii of the holder. Another 1-inch fused silica substrate was also filled in the substrate holder, which was used for broadband monitoring and post-deposition measurement. The substrates were coated by ion beam sputtering with the time-control. The deposition rates for HfO_2 and SiO_2 were approximately 0.07nm/s and 0.1nm/s, respectively.

The 300×130 mm rectangular HR coating compared to the 1-inch sample are displayed in Figure 7.3. The total loss measured by a cavity ring-down Lossmeter at 1030 nm was about 130 ppm, which corresponded to the reflectance of 99.98%. Two 300×130 mm rectangular HR coatings providing up to 23 reflections on each surface were successfully used as end mirrors for an Argon-filled Herriott cell [150, 151].

7.2 200 mm in diameter chirped mirrors

Nb_2O_5 and SiO_2 which have a larger refractive index ratio were chosen as the layer materials for the CMs. The refractive indexes were specified by the Cauchy equation with the coefficients shown in Table 4.1. A CM which provides a GDD of -100 fs^2 from 820 nm to 1000 nm with the average reflectance higher than 99.8% was designed by the needle optimization and gradual evolution algorithm. The CM consists of 46 layers with the total thicknesses of 5.5 μm. The layer structure and theoretical curves are presented in Figure 7.4.

One 200 mm in diameter substrate and another 1-inch substrate were filled in the

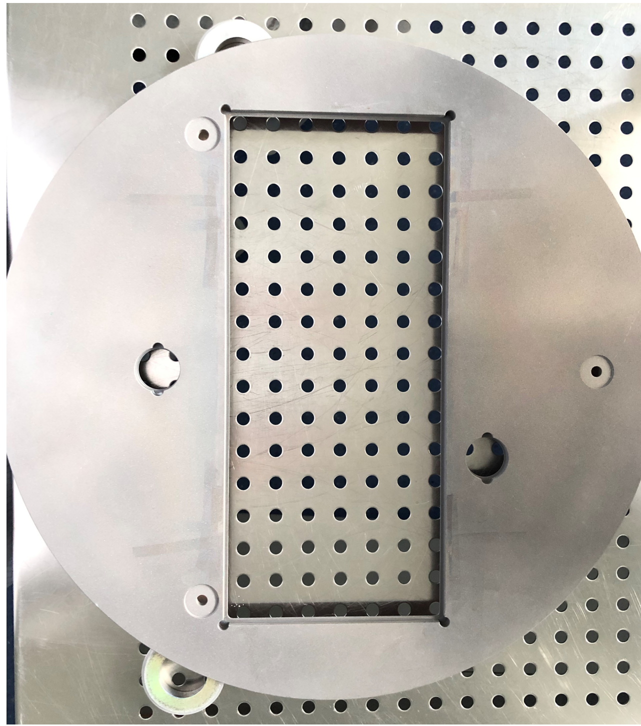

Figure 7.2: The substrate holder for 300×130 mm rectangular substrate

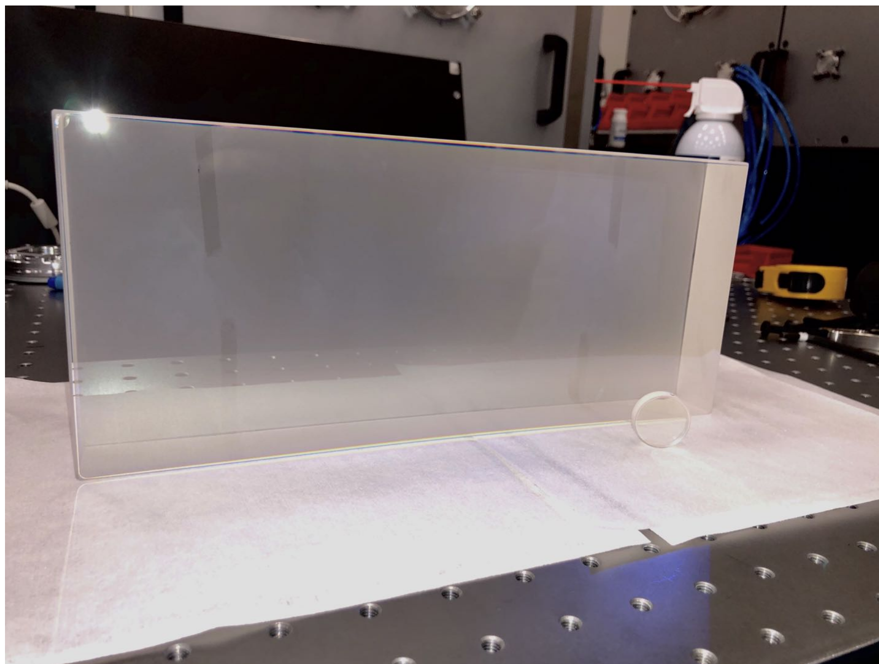

Figure 7.3: The 300×130 mm rectangular HR coating compared to 1-inch sample.

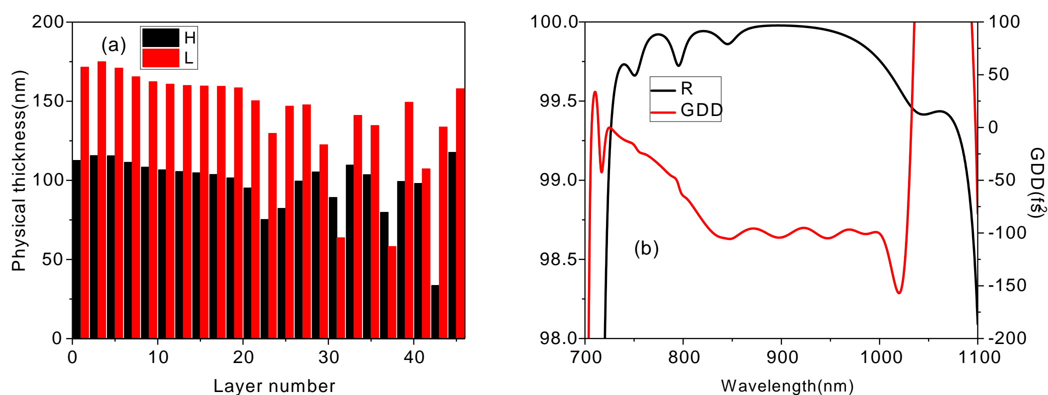

Figure 7.4: (a) Layer thickness structure of the CM. (b)Theoretical reflectance and GDD of the CM.

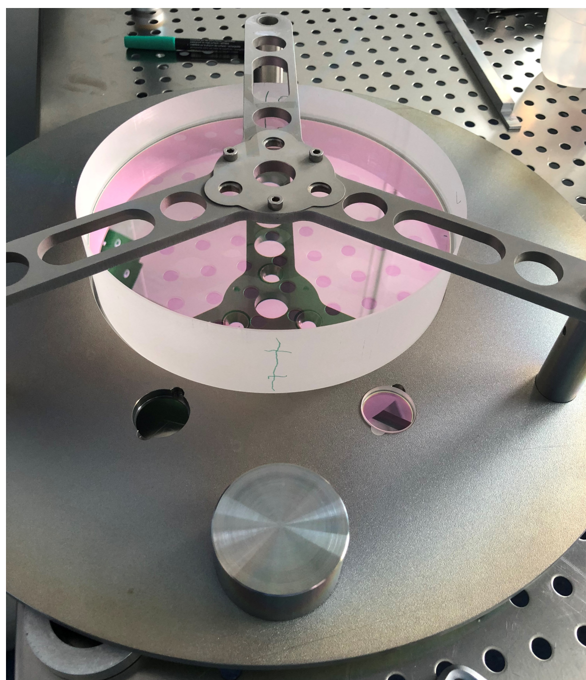

Figure 7.5: 200 mm in diameter mirror compared to 1-inch mirror in the substrate holder.

special-made substrate holder, which is shown in Figure 7.5. Production of the CMs was achieved with ion beam sputtering described in section 3.1. After the deposition, the transmittance and GDD measurement were performed on the 1-inch sample. The comparison of the theoretical and measured data is displayed in Figure 7.6. One can see that a great agreement between the theory and experiment for both transmittance and GDD was obtained.

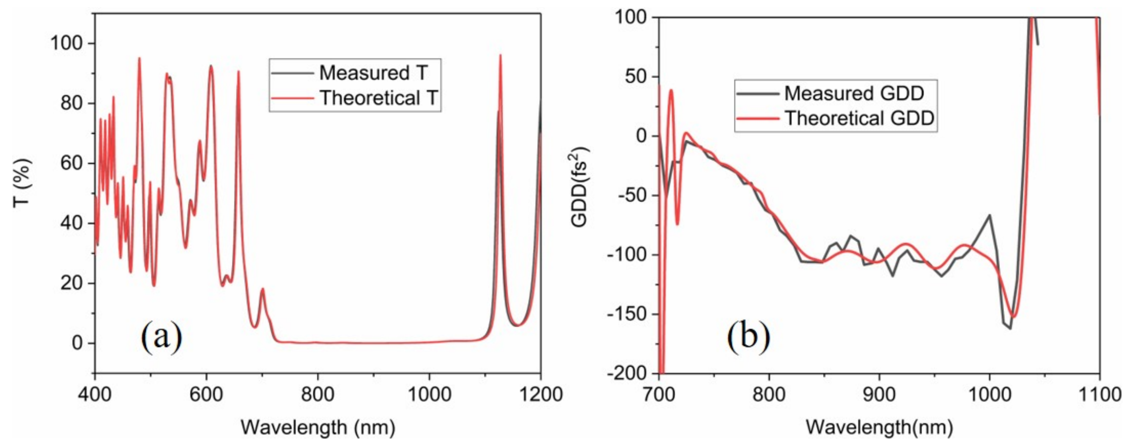

Figure 7.6: Comparison of the theoretical and experimental data for the CM.(a) Transmittance, (b) GDD

7.3 Conclusions

300 mm × 130 mm rectangular HR coatings were successfully produced with ion beam sputtering. In addition, they were used as end mirrors for an Argon-filled Herriott cell supporting up to 23 reflections on each mirror. 200 mm in diameter CMs providing a GDD of -100 fs^2 from 820 nm to 1000 nm with the average reflectance higher than 99.8% were designed, produced and characterized. The development of 300 mm × 130 mm rectangular HR coatings and 200 mm in diameter chirped mirrors proved the capability of ion beam sputtering to produce large-scale multilayer coatings.

Chapter 8

Summary and outlook

This work has demonstrated the high capacity of ion beam sputtering to produce multilayer dispersive mirrors. Broadband dispersive mirrors and high dispersive mirrors, which are regarded as two typical DMs and sensitive to different deposition errors, have been designed, produced and characterized. A comparison between IBS and MS regarding transmittance and GDD characteristics based on these two kinds of DMs has been investigated to verify the deposition accuracy of IBS. Transmittance and GDD comparison have proven that the IBS technology has comparable layer accuracy to the MS technology and verified the capacity of IBS to produce multilayer DMs.

At the same time, the GDD oscillations problem has been accompanying the development of DMs, since the first discovery of DM. Two mirror-pair methods have been proposed to suppress GDD oscillations. The first method used the spectral shift caused by non-uniformity and post-deposition annealing to realize anti-phase GDD oscillations. GDD oscillations have been suppressed significantly and the pulse quality can be improved by applying this method. With the second method, a new one octave DM pair with smooth GDD oscillations based on non-uniformity has been proposed. The suppression of GDD oscillations was fulfilled by the spectral shift due to the non-uniformity. The desired non-uniformity was obtained by adjusting the distance between the target and substrates. Thus the one octave DM pair could be produced within one coating run. The novel one octave DM pair has the advantages of working at both polarizations and being less sensitive to the AOI compared to the well-known double angle DM pair, which were verified by the comparison between the new one octave DM pair and double angle DM pair in teams of GDD characteristics and pulse analysis.

The working range of IBS has been extended to the mid-infrared regime with a mid-infrared DM. The mid-infrared fingerprint region where molecules have their distinct absorption features associated with ro-vibrational transitions has attracted lots of scientists towards MIR laser systems. At the same time, the demand of corresponding dispersion compensation elements is growing. For the first time, a new DM composed of Si and SiO_2 layers, which can compensate the dispersion of a 0.5 mm thick GaAs crystal in the spectral range of 3 to 6 μm was developed. The ion beam sputtering was employed to fabricate the mid-infrared DM. Pulse simulations show that the compensation effect of the DM is

much better than the commonly-used CaF_2 plates. Moreover, a shorter pulse with fewer satellites could be obtained with the dispersion compensated by the DM. The development of this DM has demonstrated the capacity of IBS to produce mid-infrared DMs. Due to a higher layer thickness control of the IBS, more complex DMs can be deposited by IBS.

Optical coatings with large-scale supporting large beam size laser pulse is the straightforward way to increase the damage threshold and achieve higher intensity lasers. 300 $\times$ 130 mm rectangular HR coatings were produced with IBS and successfully used as ending mirrors for an Argon-filled Herriott cell. 200 mm in diameter CMs providing a GDD of -100 fs^2 from 820 nm to 1000 nm with the average reflectance higher than 99.8% were successfully designed, produced and characterized. The development of both multilayer coatings has proven the ability of IBS to produce large diameter multilayer coatings and paved the way for the new large-scale multilayer coatings.

The capability of the ion beam sputtering to produce multilayer DMs has been proven based on broadband dispersive mirrors, high dispersive mirrors, mid-infrared DMs and large-scale DMs. Further improvement of the IBS performance could be investigated in the future. To achieve even denser and higher damage threshold optical coatings, the secondary ion assistant source could be employed. A new coating process which involves both primary source and assistant source could be developed. Besides this, extending the limits of IBS to the deep-UV and the mid-infrared range is also of great interest. The demand of multilayer dispersive mirrors below 250 nm and up to 12 μm is increasing. To achieve that, appropriate material combinations have to be used. HfO_2/SiO_2 or Al_2O_3/SiO_2 might be good options for far-UV multilayer DMs, while Ge/YbF_3 might be an excellent material combination for infrared DMs up to 12 μm. With accomplishing all these tasks, IBS will be able to deposit multilayer DMs from the deep-UV to the mid-infrared range as well as denser, lower absorption and higher damage threshold multilayer coatings.

Appendix A

Ion beam sputtering coating process

Throughout the whole PHD period, ion beam sputtering has been the main workhorse for the development of multilayer coatings. A comprehensive coating procedure is summarised.

Prior to starting the coating process, the coating design and substrate cleaning must be finished, which are described in chapter 3 and chapter 4, respectively. The coating procedure is as follow:

1. Load substrates. You can load substrates either manually or automatically. It kind of depends on the substrate size. 1.1, if substrates are relatively small, the automatic procedure is recommended. You need first put the substrate holder on the transfer arm from the transfer chamber. Then pump down the transfer chamber with the procedure of pump down-transfer chamber. After the vacuum in the transfer chamber is ready, start the load procedure. 1.2, if substrates are large and heavy, it is safer to load it manually. You need to open the coating chamber and put the substrate holder inside the coating chamber manually. When you fill substrates in the holder, three position must be chosen, which are dark, sample and reference. Otherwise, the BBM is not triggered.

2. Pump down. Pump down the coating chamber with the pump down procedure. It usually takes 2 to 3 hours until the vacuum is ready for coating. The base pressure should be in the magnitude of 10^{-7} mbar.

3. Set up the software, including the Process software in VISU computer and Thickness Monitoring, TruIBS BBM tool and OptiRe software in BBM computer. 3.1, process software in VISU computer: 3.1.1, modify the design file generated from Optilayer software, in the design file, ##CAUCHY-KOEFF=TRUE and ##K-WERTE=FALSE should be changed to ##CAUCHY-KOEFF=FALSE and ##K-WERTE=TABLE for both high and low refractive index materials, set the deposition rates for both materials in the file, 3.1.2, load the coating design under the coating procedure and activate the time control. 3.2, Thickness Monitoring and TruIBS BBM tool: 3.2.1 set the trigger positions and spectrometer wavelength range, 3.2.2 load the coating design. 3.3 OptiRe software: 3.3.1, load the coating design and choose the correct the BBM Data location (it should be the latest folder `C:/coatings`), 3.3.2, load OptiRe.

4. Warm up the primary source and neutralizer. 4.1, switch on the primary source and neutralizer, 4.2 switch on the positive voltage when the Ar gas flow decreases, 4.3, check

the matchbox, if it is about 40:80, then switch off the positive voltage, 4.4, after about 10 minutes, beam on the neutralizer and primary source, 4.5, adjust the current, voltage and RF powder according to the first layer in the coating design, 4.6, let the primary source and neutralizer run for about 30 minutes.

5. Start the coating process. Click start under the coating procedure.

6. Monitoring the coating process. Keep eyes on the Thickness Monitoring and TruIBS tool software during coating, correct the coating time if the discrepancy between the remaining time shown in Process software and the remaining time to end the current layer in TruIBS tool software. COrrecting the coating time should not be performed after 15th layer, since the errors will be accumulated to quite large in the Thickness Monitoring and TruIBS tool software and the result will not be reliable.

7. Unload substrates manually or automatically after the coating is finished.

Appendix B

Data archiving

All experimental data and all figures shown in this thesis are stored on the data archive server of the laboratory for Attosecond physics located at the Max Planck Institute of Quantum Optic in Garching:

/afs/ipp-garching.mpg.de/mpq/lap/publication_archive/Theses/2021/.

The data and figures are stored in separated chapters. All the figures in each chapter are saved in the subfolder named figures of the corresponding chapter folder. The data are stored in the subfolder named data of the corresponding chapter folder. The figures are named as fig.x.x, where x.x represents the figure number in the thesis. A word file in each chapter named Chapter.x.doc describes the detailed information of the figures and experimental data.

Bibliography

[1] T. H. Maiman *et al.*, “Stimulated optical radiation in ruby,” 1960.

[2] E. Ippen, C. Shank, and A. Dienes, “Passive mode locking of the cw dye laser,” *Applied Physics Letters*, vol. 21, no. 8, pp. 348–350, 1972.

[3] L. Hargrove, R. L. Fork, and M. Pollack, “Locking of he–ne laser modes induced by synchronous intracavity modulation,” *Applied Physics Letters*, vol. 5, no. 1, pp. 4–5, 1964.

[4] P. W. Smith, “Mode-locking of lasers,” *Proceedings of the IEEE*, vol. 58, no. 9, pp. 1342–1357, 1970.

[5] C. Shank and E. Ippen, “Subpicosecond kilowatt pulses from a mode-locked cw dye laser,” *Applied Physics Letters*, vol. 24, no. 8, pp. 373–375, 1974.

[6] E. Ippen and C. Shank, “Dynamic spectroscopy and subpicosecond pulse compression,” *Applied Physics Letters*, vol. 27, no. 9, pp. 488–490, 1975.

[7] I. Ruddock and D. Bradley, “Bandwidth-limited subpicosecond pulse generation in mode-locked cw dye lasers,” *Applied Physics Letters*, vol. 29, no. 5, pp. 296–297, 1976.

[8] P. French, “The generation of ultrashort laser pulses,” *Reports on Progress in Physics*, vol. 58, no. 2, p. 169, 1995.

[9] P. F. Moulton, “Spectroscopic and laser characteristics of ti: Al 2 o 3,” *JOSA B*, vol. 3, no. 1, pp. 125–133, 1986.

[10] T. Brabec, C. Spielmann, P. Curley, and F. Krausz, “Kerr lens mode locking,” *Optics letters*, vol. 17, no. 18, pp. 1292–1294, 1992.

[11] D. K. Negus, L. Spinelli, N. Goldblatt, and G. Feugnet, “Sub-100 femtosecond pulse generation by kerr lens mode-locking in ti: Al2o3,” in *Advanced Solid State Lasers*, p. SPL7, Optical Society of America, 1991.

[12] D. E. Spence, P. N. Kean, and W. Sibbett, “60-fsec pulse generation from a self-mode-locked ti: sapphire laser,” *Optics letters*, vol. 16, no. 1, pp. 42–44, 1991.

[13] F. Krausz, C. Spielmann, T. Brabec, E. Wintner, and A. Schmidt, "Generation of 33-fs optical pulses from a solid-state laser," *Optics letters*, vol. 17, no. 3, pp. 204–206, 1992.

[14] R. Szipöcs, K. Ferencz, C. Spielmann, and F. Krausz, "Chirped multilayer coatings for broadband dispersion control in femtosecond lasers," *Optics letters*, vol. 19, no. 3, pp. 201–203, 1994.

[15] F. Gires and P. Tournois, "Interferometre utilisable pour la compression dimpulsions lumineuses modulees en frequence," *Comptes Rendus Hebdomadaires Des Seances De L Academie Des Sciences*, vol. 258, no. 25, p. 6112, 1964.

[16] J. Heppner and J. Kuhl, "Intracavity chirp compensation in a colliding pulse mode-locked laser using thin-film interferometers," *Applied physics letters*, vol. 47, no. 5, pp. 453–455, 1985.

[17] J. Kuhl and J. Heppner, "Compression of femtosecond optical pulses with dielectric multilayer interferometers," *IEEE journal of quantum electronics*, vol. 22, no. 1, pp. 182–185, 1986.

[18] K. D. Li, W. H. Knox, and N. M. Pearson, "Broadband cubic-phase compensation with resonant gires–tournois interferometers," *Optics letters*, vol. 14, no. 9, pp. 450–452, 1989.

[19] B. Golubovic, R. Austin, M. Steiner-Shepard, M. Reed, S. A. Diddams, D. Jones, and A. G. Van Engen, "Double gires–tournois interferometer negative-dispersion mirrors for use in tunable mode-locked lasers," *Optics letters*, vol. 25, no. 4, pp. 275–277, 2000.

[20] V. Pervak, "Recent development and new ideas in the field of dispersive multilayer optics," *Applied optics*, vol. 50, no. 9, pp. C55–C61, 2011.

[21] V. Pervak, T. Amotchkina, Q. Wang, O. Pronin, K. F. Mak, and M. Trubetskov, "2/3 octave si/sio 2 infrared dispersive mirrors open new horizons in ultrafast multilayer optics," *Optics express*, vol. 27, no. 1, pp. 55–62, 2019.

[22] V. Pervak, A. Tikhonravov, M. Trubetskov, S. Naumov, F. Krausz, and A. Apolonski, "1.5-octave chirped mirror for pulse compression down to sub-3 fs," *Applied Physics B*, vol. 87, no. 1, pp. 5–12, 2007.

[23] V. Pervak, I. Ahmad, J. Fulop, M. Trubetskov, and A. Tikhonravov, "Comparison of dispersive mirrors based on the time-domain and conventional approaches, for sub-5-fs pulses.," *Optics express*, vol. 17, no. 4, pp. 2207–2217, 2009.

[24] V. Pervak, I. Ahmad, M. Trubetskov, A. Tikhonravov, and F. Krausz, "Double-angle multilayer mirrors with smooth dispersion characteristics," *Optics express*, vol. 17, no. 10, pp. 7943–7951, 2009.

[25] F. Habel, V. Shirvanyan, M. Trubetskov, C. Burger, A. Sommer, M. F. Kling, M. Schultze, and V. Pervak, "Octave spanning wedge dispersive mirrors with low dispersion oscillations," *Optics express*, vol. 24, no. 9, pp. 9218–9223, 2016.

[26] F. Kärtner, U. Morgner, R. Ell, T. Schibli, J. Fujimoto, E. Ippen, V. Scheuer, G. Angelow, and T. Tschudi, "Ultrabroadband double-chirped mirror pairs for generation of octave spectra," *JOSA B*, vol. 18, no. 6, pp. 882–885, 2001.

[27] T. Amotchkina, M. Trubetskov, S. A. Hussain, D. Hahner, D. Gerz, M. Huber, W. Schweinberger, I. Pupeza, F. Krausz, and V. Pervak, "Broadband dispersive ge/ybf 3 mirrors for mid-infrared spectral range," *Optics letters*, vol. 44, no. 21, pp. 5210–5213, 2019.

[28] V. Laude and P. Tournois, "Chirped-mirror pairs for ultra-broadband dispersion control," in *Technical Digest. Summaries of papers presented at the Conference on Lasers and Electro-Optics. Postconference Edition. CLEO'99. Conference on Lasers and Electro-Optics (IEEE Cat. No. 99CH37013)*, pp. 187–188, IEEE, 1999.

[29] V. Pervak, T. Amotchkina, D. Hahner, S. Jung, Y. Pervak, M. Trubetskov, and F. Krausz, "Complementary si/sio 2 dispersive mirrors for 2-4 μm spectral range," *Optics express*, vol. 27, no. 24, pp. 34901–34906, 2019.

[30] Y. Chen, D. Hahner, M. Trubetskov, S. Schrameyer, W. Sakiew, K. Starke, and V. Pervak, "Comparison of magnetron sputtering and ion beam sputtering on dispersive mirrors," *Applied Physics B*, vol. 126, no. 5, pp. 1–6, 2020.

[31] T. R. Schibli, O. Kuzucu, J.-W. Kim, E. P. Ippen, J. G. Fujimoto, F. X. Kaertner, V. Scheuer, and G. Angelow, "Toward single-cycle laser systems," *IEEE Journal of Selected Topics in Quantum Electronics*, vol. 9, no. 4, pp. 990–1001, 2003.

[32] S.-H. Chia, G. Cirmi, S. Fang, G. M. Rossi, O. D. Mücke, and F. X. Kärtner, "Two-octave-spanning dispersion-controlled precision optics for sub-optical-cycle waveform synthesizers," *Optica*, vol. 1, no. 5, pp. 315–322, 2014.

[33] Y. Ozeki, G. Omura, and K. Itoh, "Broadband group delay dispersion compensation for a microscope objective lens with a speciallydesigned mechanical deformable mirror," *Optics express*, vol. 16, no. 4, pp. 2778–2783, 2008.

[34] S. R. Dods, Z. Zhang, and M. Ogura, "Highly dispersive mirror in ta 2 o 5/sio 2 for femtosecond lasers designed by inverse spectral theory," *Applied optics*, vol. 38, no. 21, pp. 4711–4719, 1999.

[35] V. Pervak, C. Teisset, A. Sugita, S. Naumov, F. Krausz, and A. Apolonski, "High-dispersive mirrors for femtosecond lasers," *Optics express*, vol. 16, no. 14, pp. 10220–10233, 2008.

[36] V. Pervak, I. Ahmad, S. A. Trushin, Z. Major, A. Apolonski, S. Karsch, and F. Krausz, "Chirped-pulse amplification of laser pulses with dispersive mirrors," *Optics express*, vol. 17, no. 21, pp. 19204–19212, 2009.

[37] P. Dombi, P. Rácz, M. Lenner, V. Pervak, and F. Krausz, "Dispersion management in femtosecond laser oscillators with highly dispersive mirrors," *Optics express*, vol. 17, no. 22, pp. 20598–20604, 2009.

[38] V. Pervak, O. Pronin, O. Razskazovskaya, J. Brons, I. Angelov, M. Trubetskov, A. Tikhonravov, and F. Krausz, "High-dispersive mirrors for high power applications," *Optics express*, vol. 20, no. 4, pp. 4503–4508, 2012.

[39] E. Fedulova, K. Fritsch, J. Brons, O. Pronin, T. Amotchkina, M. Trubetskov, F. Krausz, and V. Pervak, "Highly-dispersive mirrors reach new levels of dispersion," *Optics express*, vol. 23, no. 11, pp. 13788–13793, 2015.

[40] O. Pronin, J. Brons, C. Grasse, V. Pervak, G. Boehm, M.-C. Amann, A. Apolonski, V. L. Kalashnikov, and F. Krausz, "High-power kerr-lens mode-locked yb: Yag thin-disk oscillator in the positive dispersion regime," *Optics letters*, vol. 37, no. 17, pp. 3543–3545, 2012.

[41] Y. Chen, Y. Wang, L. Wang, M. Zhu, H. Qi, J. Shao, X. Huang, S. Yang, C. Li, K. Zhou, *et al.*, "High dispersive mirrors for erbium-doped fiber chirped pulse amplification system," *Optics express*, vol. 24, no. 17, pp. 19835–19840, 2016.

[42] T. Amotchkina, M. Trubetskov, F. Habel, Y. Pervak, J. Zhang, K. Mak, O. Pronin, F. Krausz, and V. Pervak, "Synthesis, fabrication and characterization of a highly-dispersive mirrors for the 2 μm spectral range," *Optics express*, vol. 25, no. 9, pp. 10234–10240, 2017.

[43] R. Chen, Y. Wang, K. Guo, Y. Zhang, Z. Wang, J. Niu, B. Liu, M. Zhu, K. Yi, and J. Shao, "Highly-dispersive mirrors with advanced group delay dispersion," *IEEE Photonics Technology Letters*, vol. 32, no. 2, pp. 113–116, 2019.

[44] P. Ma, Y. Chen, T. Amotchkina, M. Trubetskov, V. Pervak, and L. Li, "Design, fabrication and measurement of highly-dispersive mirrors with total internal reflection," *Optics Express*, vol. 28, no. 20, pp. 29230–29238, 2020.

[45] P. Wnuk, P. Wasylczyk, M. Dems, K. Hejduk, K. Regiński, A. Wójcik-Jedlińska, A. Jasik, *et al.*, "Continuously tunable yb: Kyw femtosecond oscillator based on a tunable highly dispersive semiconductor mirror," *Optics express*, vol. 22, no. 15, pp. 18284–18289, 2014.

[46] A. Jasik, M. Dems, P. Wnuk, P. Wasylczyk, A. Wójcik-Jedlińska, K. Regiński, Ł. Zinkiewicz, and K. Hejduk, "Design and fabrication of highly dispersive semiconductor double-chirped mirrors," *Applied Physics B*, vol. 116, no. 1, pp. 141–146, 2014.

[47] Y. I. Salamin, S. Hu, K. Z. Hatsagortsyan, and C. H. Keitel, "Relativistic high-power laser–matter interactions," *Physics Reports*, vol. 427, no. 2-3, pp. 41–155, 2006.

[48] S. Seuferling, M. A. O. Haug, P. Hilz, D. Haffa, C. Kreuzer, and J. Schreiber, "Efficient offline production of freestanding thin plastic foils for laser-driven ion sources," *High Power Laser Science and Engineering*, vol. 5, 2017.

[49] D. Umstadter, "Review of physics and applications of relativistic plasmas driven by ultra-intense lasers," *Physics of Plasmas*, vol. 8, no. 5, pp. 1774–1785, 2001.

[50] H. T. Kim, K. H. Pae, H. J. Cha, I. J. Kim, T. J. Yu, J. H. Sung, S. K. Lee, T. M. Jeong, and J. Lee, "Enhancement of electron energy to the multi-gev regime by a dual-stage laser-wakefield accelerator pumped by petawatt laser pulses," *Physical review letters*, vol. 111, no. 16, p. 165002, 2013.

[51] S. Bulanov, T. Z. Esirkepov, M. Kando, J. Koga, K. Kondo, and G. Korn, "On the problems of relativistic laboratory astrophysics and fundamental physics with super powerful lasers," *Plasma Physics Reports*, vol. 41, no. 1, pp. 1–51, 2015.

[52] K. Seshan, *Handbook of thin film deposition processes and techniques*. William Andrew, 2001.

[53] F. Habel and V. Pervak, "Dispersive mirror for the mid-infrared spectral range of 9–11.5 μm," *Applied optics*, vol. 56, no. 4, pp. C71–C74, 2017.

[54] F. Kärtner, N. Matuschek, T. Schibli, U. Keller, H. Haus, C. Heine, R. Morf, V. Scheuer, M. Tilsch, and T. Tschudi, "Design and fabrication of double-chirped mirrors," *Optics letters*, vol. 22, no. 11, pp. 831–833, 1997.

[55] R. Chen, Y. Wang, K. Guo, Y. Zhang, Z. Wang, M. Zhu, K. Yi, Y. Leng, and J. Shao, "Angle-adjustment-based tunable chirped mirrors with continuous dispersion compensation," *Optics Letters*, vol. 44, no. 24, pp. 6053–6056, 2019.

[56] F. Habel, *Advanced dispersive mirrors for ultrashort laser pulses from the near-UV to the mid-IR spectral range*. PhD thesis, Ludwig Maximilians Universität München, 2017.

[57] W. Sakiew, S. Schrameyer, P. Schwerdtner, N. Erhart, and K. Starke, "Large area precision optical coatings by reactive ion beam sputtering," *Applied Optics*, vol. 59, no. 14, pp. 4296–4302, 2020.

[58] N. Matuschek, F. X. Kartner, and U. Keller, "Theory of double-chirped mirrors," *IEEE Journal of selected topics in quantum electronics*, vol. 4, no. 2, pp. 197–208, 1998.

[59] N. Matuschek, F. X. Kartner, and U. Keller, "Exact coupled-mode theories for multilayer interference coatings with arbitrary strong index modulations," *IEEE journal of quantum electronics*, vol. 33, no. 3, pp. 295–302, 1997.

[60] N. Matuschek, F. X. Kartner, and U. Keller, "Analytical design of double-chirped mirrors with custom-tailored dispersion characteristics," *IEEE Journal of Quantum Electronics*, vol. 35, no. 2, pp. 129–137, 1999.

[61] G. Steinmeyer, "Brewster-angled chirped mirrors for high-fidelity dispersion compensation and bandwidths exceeding one optical octave," *Optics express*, vol. 11, no. 19, pp. 2385–2396, 2003.

[62] P. Baum, M. Breuer, E. Riedle, and G. Steinmeyer, "Brewster-angled chirped mirrors for broadband pulse compression without dispersion oscillations," *Optics letters*, vol. 31, no. 14, pp. 2220–2222, 2006.

[63] N. Matuschek, L. Gallmann, D. Sutter, G. Steinmeyer, and U. Keller, "Back-side-coated chirped mirrors with ultra-smooth broadband dispersion characteristics," *Applied Physics B*, vol. 71, no. 4, pp. 509–522, 2000.

[64] G. Tempea, V. Yakovlev, B. Bacovic, F. Krausz, and K. Ferencz, "Tilted-front-interface chirped mirrors," *JOSA B*, vol. 18, no. 11, pp. 1747–1750, 2001.

[65] E. R. Crosson, K. N. Ricci, B. A. Richman, F. C. Chilese, T. G. Owano, R. A. Provencal, M. W. Todd, J. Glasser, A. A. Kachanov, B. A. Paldus, *et al.*, "Stable isotope ratios using cavity ring-down spectroscopy: determination of 13c/12c for carbon dioxide in human breath," *Analytical Chemistry*, vol. 74, no. 9, pp. 2003–2007, 2002.

[66] A. Schliesser, N. Picqué, and T. W. Hänsch, "Mid-infrared frequency combs," *Nature photonics*, vol. 6, no. 7, pp. 440–449, 2012.

[67] Z. Du, S. Zhang, J. Li, N. Gao, and K. Tong, "Mid-infrared tunable laser-based broadband fingerprint absorption spectroscopy for trace gas sensing: a review," *Applied sciences*, vol. 9, no. 2, p. 338, 2019.

[68] J. Li, Z. Yu, Z. Du, Y. Ji, and C. Liu, "Standoff chemical detection using laser absorption spectroscopy: a review," *Remote Sensing*, vol. 12, no. 17, p. 2771, 2020.

[69] F. Träger, *Springer handbook of lasers and optics.* Springer Science & Business Media, 2012.

[70] J.-C. Diels and W. Rudolph, *Ultrashort laser pulse phenomena.* Elsevier, 2006.

[71] W. Sellmeier, "Ueber die durch die aetherschwingungen erregten mitschwingungen der körpertheilchen und deren rückwirkung auf die ersteren, besonders zur erklärung der dispersion und ihrer anomalien," *Annalen der Physik*, vol. 223, no. 12, pp. 525–554, 1872.

[72] A. Monmayrant, S. Weber, B. Chatel, *et al.*, “A newcomer’s guide to ultrashort pulse shaping and characterization,” *J. Phys. B*, vol. 43, no. 10, p. 103001, 2010.

[73] R. Trebino, *Frequency-Resolved Optical Gating: The Measurement of Ultrashort Laser Pulses: The Measurement of Ultrashort Laser Pulses*. Springer Science & Business Media, 2000.

[74] D. J. Kane and R. Trebino, “Characterization of arbitrary femtosecond pulses using frequency-resolved optical gating,” *IEEE Journal of Quantum Electronics*, vol. 29, no. 2, pp. 571–579, 1993.

[75] D. Strickland and G. Mourou, “Compression of amplified chirped optical pulses,” *Optics communications*, vol. 55, no. 6, pp. 447–449, 1985.

[76] R. Fork, O. Martinez, and J. Gordon, “Negative dispersion using pairs of prisms,” *Optics letters*, vol. 9, no. 5, pp. 150–152, 1984.

[77] J. P. Gordon and R. Fork, “Optical resonator with negative dispersion,” *Optics letters*, vol. 9, no. 5, pp. 153–155, 1984.

[78] H. A. Macleod, *Thin-film optical filters*. CRC press, 2017.

[79] N. Kaiser and H. K. Pulker, *Optical interference coatings*, vol. 88. Springer, 2013.

[80] A. V. Tikhonravov, “Design of optical coatings,” in *Optical interference coatings*, pp. 81–104, Springer, 2003.

[81] A. V. Tikhonravov and M. K. Trubetskov, “Optilayer.” `http://www.optilayer.com`, 1996.

[82] A. V. Tikhonravov, M. K. Trubetskov, and G. W. DeBell, “Application of the needle optimization technique to the design of optical coatings,” *Applied optics*, vol. 35, no. 28, pp. 5493–5508, 1996.

[83] A. V. Tikhonravov and M. K. Trubetskov, “Modern design tools and a new paradigm in optical coating design,” *Applied optics*, vol. 51, no. 30, pp. 7319–7332, 2012.

[84] P. Bentley, “The modern cryopump,” *Vacuum*, vol. 30, no. 4-5, pp. 145–158, 1980.

[85] M. Becker, M. Gies, A. Polity, S. Chatterjee, and P. Klar, “Materials processing using radio-frequency ion-sources: Ion-beam sputter-deposition and surface treatment,” *Review of Scientific Instruments*, vol. 90, no. 2, p. 023901, 2019.

[86] B. G. Bovard, “Rugate filter theory: an overview,” *Applied optics*, vol. 32, no. 28, pp. 5427–5442, 1993.

[87] M. Jupé, M. Lappschies, L. Jensen, K. Starke, and D. Ristau, "Laser-induced damage in gradual index layers and rugate filters," in *Laser-Induced Damage in Optical Materials: 2006*, vol. 6403, p. 640311, International Society for Optics and Photonics, 2007.

[88] Z. Qiao, P. Ma, H. Liu, Y. Pu, and Z. Liu, "Laser-induced damage of rugate and quarter-wave stacks high reflectors deposited by ion-beam sputtering," *Optical Engineering*, vol. 52, no. 8, p. 086103, 2013.

[89] K. Starke, T. Grosz, M. Lappschies, and D. Ristau, "Rapid prototyping of optical thin film filters," in *Optical and Infrared Thin Films*, vol. 4094, pp. 83–92, International Society for Optics and Photonics, 2000.

[90] D. Ristau, H. Ehlers, T. Gross, and M. Lappschies, "Optical broadband monitoring of conventional and ion processes," *Applied Optics*, vol. 45, no. 7, pp. 1495–1501, 2006.

[91] A. V. Tikhonravov, M. K. Trubetskov, and T. V. Amotchkina, "Investigation of the effect of accumulation of thickness errors in optical coating production by broadband optical monitoring," *Applied optics*, vol. 45, no. 27, pp. 7026–7034, 2006.

[92] M. Gross, S. Dligatch, and A. Chtanov, "Optimization of coating uniformity in an ion beam sputtering system using a modified planetary rotation method," *Applied optics*, vol. 50, no. 9, pp. C316–C320, 2011.

[93] W. Sakiew, S. Schrameyer, M. Jupé, P. Schwerdtner, N. Erhart, K. Starke, and D. Ristau, "Influence of ion beam parameters onto two-dimensional optical thin film thickness distributions deposited by ion beam sputtering," *Thin Solid Films*, vol. 682, pp. 109–120, 2019.

[94] D. Depla, S. Mahieu, *et al.*, *Reactive sputter deposition*, vol. 109. Springer, 2008.

[95] E. Çetinörgü-Goldenberg, J.-E. Klemberg-Sapieha, and L. Martinu, "Effect of post-deposition annealing on the structure, composition, and the mechanical and optical characteristics of niobium and tantalum oxide films," *Applied optics*, vol. 51, no. 27, pp. 6498–6507, 2012.

[96] S. Chandra, P. S. Reddy, G. M. Rao, and S. Uthanna, "Effect of postdeposition annealing on the structural, electrical, and optical properties of dc magnetron sputtered ta2o5 films," *Research Letters in Materials Science*, vol. 2007, 2007.

[97] D. Z. Anderson, J. C. Frisch, and C. S. Masser, "Mirror reflectometer based on optical cavity decay time," *Applied optics*, vol. 23, no. 8, pp. 1238–1245, 1984.

[98] A. O'Keefe and D. A. Deacon, "Cavity ring-down optical spectrometer for absorption measurements using pulsed laser sources," *Review of scientific instruments*, vol. 59, no. 12, pp. 2544–2551, 1988.

[99] D. Grupe, *Measuring group delay dispersion in the UV-VIS-IR range by white-light interferometry.* PhD thesis, PhD thesis, Ludwig-Maximilians-University, 2008.

[100] T. V. Amotchkina, A. V. Tikhonravov, M. K. Trubetskov, D. Grupe, A. Apolonski, and V. Pervak, "Measurement of group delay of dispersive mirrors with white-light interferometer," *Applied optics*, vol. 48, no. 5, pp. 949–956, 2009.

[101] F. Habel, M. Trubetskov, and V. Pervak, "Group delay dispersion measurements in the mid-infrared spectral range of 2-20 μm," *Optics express*, vol. 24, no. 15, pp. 16705–16710, 2016.

[102] H.-W. Chen, T. Sosnowski, C.-H. Liu, L.-J. Chen, J. R. Birge, A. Galvanauskas, F. X. Kärtner, and G. Chang, "Chirally-coupled-core yb-fiber laser delivering 80-fs pulses with diffraction-limited beam quality warranted by a high-dispersion mirror based compressor," *Optics express*, vol. 18, no. 24, pp. 24699–24705, 2010.

[103] O. Razskazovskaya, M. T. Hassan, T. T. Luu, E. Goulielmakis, and V. Pervak, "Efficient broadband highly dispersive hfo 2/sio 2 multilayer mirror for pulse compression in near ultraviolet," *Optics express*, vol. 24, no. 12, pp. 13628–13633, 2016.

[104] S. Vasilyev, I. Moskalev, M. Mirov, S. Mirov, and V. Gapontsev, "Multi-watt mid-ir femtosecond polycrystalline cr 2+: Zns and cr 2+: Znse laser amplifiers with the spectrum spanning 2.0–2.6 μm," *Optics express*, vol. 24, no. 2, pp. 1616–1623, 2016.

[105] V. Pervak, M. Trubetskov, and A. Tikhonravov, "Robust synthesis of dispersive mirrors," *Optics Express*, vol. 19, no. 3, pp. 2371–2380, 2011.

[106] Y. Chen, D. Hahner, M. Trubetskov, and V. Pervak, "Suppression of group delay dispersion oscillations of highly dispersive mirrors by non-uniformity and post-deposition treatment," *Optics & Laser Technology*, vol. 142, p. 107192, 2021.

[107] V. Pervak, F. Krausz, and A. Apolonski, "Dispersion control over the ultraviolet-visible-near-infrared spectral range with hfo 2/sio 2-chirped dielectric multilayers," *Optics letters*, vol. 32, no. 9, pp. 1183–1185, 2007.

[108] M. T. Hassan, T. T. Luu, A. Moulet, O. Raskazovskaya, P. Zhokhov, M. Garg, N. Karpowicz, A. Zheltikov, V. Pervak, F. Krausz, *et al.*, "Optical attosecond pulses and tracking the nonlinear response of bound electrons," *Nature*, vol. 530, no. 7588, pp. 66–70, 2016.

[109] O. Razskazovskaya, F. Krausz, and V. Pervak, "Multilayer coatings for femto-and attosecond technology," *Optica*, vol. 4, no. 1, pp. 129–138, 2017.

[110] C. Marceau, G. Gingras, S. T. Bah, R. Vallée, and B. Witzel, "Femtosecond laser pulse compression using angle of incidence optimization of chirped mirrors," *Laser Physics Letters*, vol. 11, no. 6, p. 065302, 2014.

[111] S. Melnikas, U. Gimževskis, and S. Kičas, "Stress compensated back side coated chirped mirror with high negative dispersion," *Optics & Laser Technology*, vol. 121, p. 105820, 2020.

[112] L. Ren, L. Chen, M. Zhang, C. Zhou, Y. Cai, and Z. Zhang, "Group delay dispersion compensation in an ytterbium-doped fiber laser using intracavity gires–tournois interferometers," *Optics & Laser Technology*, vol. 42, no. 7, pp. 1077–1079, 2010.

[113] A. Jasik, P. Wasylczyk, P. Wnuk, M. Dems, A. Wójcik-Jedlińska, K. Regiński, Ł. Zinkiewicz, and K. Hejduk, "Tunable semiconductor double-chirped mirror with high negative dispersion," *IEEE Photonics Technology Letters*, vol. 26, no. 1, pp. 14–17, 2013.

[114] V. Pervak, V. Fedorov, Y. A. Pervak, and M. Trubetskov, "Empirical study of the group delay dispersion achievable with multilayer mirrors," *Optics express*, vol. 21, no. 15, pp. 18311–18316, 2013.

[115] H. H. Andersen, "Sputtering from atomic-collision cascades," *Nuclear Instruments and Methods in Physics Research Section B: Beam Interactions with Materials and Atoms*, vol. 33, no. 1-4, pp. 466–473, 1988.

[116] S.-H. Woo and C. K. Hwangbo, "Effects of annealing on the optical, structural, and chemical properties of tio 2 and mgf 2 thin films prepared by plasma ion-assisted deposition," *Applied optics*, vol. 45, no. 7, pp. 1447–1455, 2006.

[117] T. Plirdpring, M. Horprathum, C. Chananonnawathorn, P. Eiamchai, A. Harnwunggmoung, T. Boonpichayapha, P. Lorwongtragool, and A. Charoenphakdee, "Effect of annealing temperature on structure and optical properties of ta2o5 thin films prepared by dc magnetron sputtering," in *Advanced Materials Research*, vol. 770, pp. 149–152, Trans Tech Publ, 2013.

[118] M. Drescher, M. Hentschel, R. Kienberger, M. Uiberacker, V. Yakovlev, A. Scrinzi, T. Westerwalbesloh, U. Kleineberg, U. Heinzmann, and F. Krausz, "Time-resolved atomic inner-shell spectroscopy," *Nature*, vol. 419, no. 6909, pp. 803–807, 2002.

[119] A. L. Cavalieri, N. Müller, T. Uphues, V. S. Yakovlev, A. Baltuška, B. Horvath, B. Schmidt, L. Blümel, R. Holzwarth, S. Hendel, *et al.*, "Attosecond spectroscopy in condensed matter," *Nature*, vol. 449, no. 7165, pp. 1029–1032, 2007.

[120] B. Muskatel, F. Remacle, and R. D. Levine, "The post-born–oppenheimer regime: dynamics of electronic motion in molecules by attosecond few-cycle spectroscopy," *Physica Scripta*, vol. 80, no. 4, p. 048101, 2009.

[121] M. Fieß, M. Schultze, E. Goulielmakis, B. Dennhardt, J. Gagnon, M. Hofstetter, R. Kienberger, and F. Krausz, "Versatile apparatus for attosecond metrology and spectroscopy," *Review of Scientific Instruments*, vol. 81, no. 9, p. 093103, 2010.

[122] E. Goulielmakis, V. S. Yakovlev, A. L. Cavalieri, M. Uiberacker, V. Pervak, A. Apolonski, R. Kienberger, U. Kleineberg, and F. Krausz, “Attosecond control and measurement: lightwave electronics,” *Science*, vol. 317, no. 5839, pp. 769–775, 2007.

[123] F. Krausz and M. Ivanov, “Attosecond physics,” *Reviews of modern physics*, vol. 81, no. 1, p. 163, 2009.

[124] M. Hentschel, R. Kienberger, C. Spielmann, G. A. Reider, N. Milosevic, T. Brabec, P. Corkum, U. Heinzmann, M. Drescher, and F. Krausz, “Attosecond metrology,” *Nature*, vol. 414, no. 6863, pp. 509–513, 2001.

[125] F. Krausz, “The birth of attosecond physics and its coming of age,” *Physica Scripta*, vol. 91, no. 6, p. 063011, 2016.

[126] F. Silva, M. Miranda, B. Alonso, J. Rauschenberger, V. Pervak, and H. Crespo, “Simultaneous compression, characterization and phase stabilization of gw-level 1.4 cycle vis-nir femtosecond pulses using a single dispersion-scan setup,” *Optics express*, vol. 22, no. 9, pp. 10181–10191, 2014.

[127] F. Silva, B. Alonso, W. Holgado, R. Romero, J. San Román, E. C. Jarque, H. Koop, V. Pervak, H. Crespo, and Í. J. Sola, “Strategies for achieving intense single-cycle pulses with in-line post-compression setups,” *Optics letters*, vol. 43, no. 2, pp. 337–340, 2018.

[128] A. Wirth, M. T. Hassan, I. Grguraš, J. Gagnon, A. Moulet, T. T. Luu, S. Pabst, R. Santra, Z. Alahmed, A. Azzeer, *et al.*, “Synthesized light transients,” *Science*, vol. 334, no. 6053, pp. 195–200, 2011.

[129] T. Nagy, M. Kretschmar, M. J. Vrakking, and A. Rouzée, “Generation of above-terawatt 1.5-cycle visible pulses at 1 khz by post-compression in a hollow fiber,” *Optics Letters*, vol. 45, no. 12, pp. 3313–3316, 2020.

[130] M. Trubetskov, V. Pervak, and A. Tikhonravov, “Phase optimization of dispersive mirrors based on floating constants,” *Optics express*, vol. 18, no. 26, pp. 27613–27618, 2010.

[131] N. Nagl, K. F. Mak, Q. Wang, V. Pervak, F. Krausz, and O. Pronin, “Efficient femtosecond mid-infrared generation based on a cr: Zns oscillator and step-index fluoride fibers,” *Optics letters*, vol. 44, no. 10, pp. 2390–2393, 2019.

[132] F. Adler, P. Masłowski, A. Foltynowicz, K. C. Cossel, T. C. Briles, I. Hartl, and J. Ye, “Mid-infrared fourier transform spectroscopy with a broadband frequency comb,” *Optics express*, vol. 18, no. 21, pp. 21861–21872, 2010.

[133] Z. Zhang, C. Gu, J. Sun, C. Wang, T. Gardiner, and D. T. Reid, "Asynchronous mid-infrared ultrafast optical parametric oscillator for dual-comb spectroscopy," *Optics letters*, vol. 37, no. 2, pp. 187–189, 2012.

[134] F. Keilmann, C. Gohle, and R. Holzwarth, "Time-domain mid-infrared frequency-comb spectrometer," *Optics letters*, vol. 29, no. 13, pp. 1542–1544, 2004.

[135] P. á. Corkum and F. Krausz, "Attosecond science," *Nature physics*, vol. 3, no. 6, pp. 381–387, 2007.

[136] C. M. Sears, E. Colby, R. England, R. Ischebeck, C. McGuinness, J. Nelson, R. Noble, R. H. Siemann, J. Spencer, D. Walz, *et al.*, "Phase stable net acceleration of electrons from a two-stage optical accelerator," *Physical Review Special Topics-Accelerators and Beams*, vol. 11, no. 10, p. 101301, 2008.

[137] V. Smolski, H. Yang, S. Gorelov, P. Schunemann, and K. Vodopyanov, "Coherence properties of a 2.6–7.5 μm frequency comb produced as a subharmonic of a tm-fiber laser," *Optics letters*, vol. 41, no. 7, pp. 1388–1391, 2016.

[138] V. Smolski, S. Vasilyev, P. Schunemann, S. Mirov, and K. Vodopyanov, "Cr: Zns laser-pumped subharmonic gaas optical parametric oscillator with the spectrum spanning 3.6–5.6 μm," *Optics letters*, vol. 40, no. 12, pp. 2906–2908, 2015.

[139] N. Leindecker, A. Marandi, R. L. Byer, K. L. Vodopyanov, J. Jiang, I. Hartl, M. Fermann, and P. G. Schunemann, "Octave-spanning ultrafast opo with 2.6-6.1 μm instantaneous bandwidth pumped by femtosecond tm-fiber laser," *Optics express*, vol. 20, no. 7, pp. 7046–7053, 2012.

[140] K. Vodopyanov, E. Sorokin, I. T. Sorokina, and P. Schunemann, "Mid-ir frequency comb source spanning 4.4–5.4 μm based on subharmonic gaas optical parametric oscillator," *Optics letters*, vol. 36, no. 12, pp. 2275–2277, 2011.

[141] T. V. Amotchkina, V. Janicki, J. Sancho-Parramon, A. V. Tikhonravov, M. K. Trubetskov, and H. Zorc, "General approach to reliable characterization of thin metal films," *Applied optics*, vol. 50, no. 10, pp. 1453–1464, 2011.

[142] T. Amotchkina, M. Trubetskov, D. Hahner, and V. Pervak, "Characterization of e-beam evaporated ge, ybf 3, zns, and laf 3 thin films for laser-oriented coatings," *Applied optics*, vol. 59, no. 5, pp. A40–A47, 2020.

[143] S. Li Chen, Y. An Zhao, J. Da Shao, Y. Zhi Wang, Z. Fang, X. Feng Liu, G. Hang Hu, Y. Xin Leng, and Y. Xu, "Ultrashort laser-driven stable-buckling of blisters in chirped mirror," *Applied Physics Letters*, vol. 102, no. 8, p. 081605, 2013.

[144] S. Chen, P. Gao, Y. Zhao, Y. Wang, Z. Fang, Y. Leng, and J. Shao, "Thermal-dynamical analysis of blister formation in chirped mirror irradiated by single femtosecond lasers," *Applied optics*, vol. 53, no. 15, pp. 3347–3354, 2014.

[145] I. B. Angelov, M. von Pechmann, M. K. Trubetskov, F. Krausz, and V. Pervak, "Optical breakdown of multilayer thin-films induced by ultrashort pulses at mhz repetition rates," *Optics express*, vol. 21, no. 25, pp. 31453–31461, 2013.

[146] S. Melnikas, T. Tolenis, L. Smalakys, G. Batavičiūtė, A. Melninkaitis, and S. Kičas, "Enhancement of laser-induced damage threshold in chirped mirrors by electric field reallocation," *Optics express*, vol. 25, no. 22, pp. 26537–26545, 2017.

[147] M. Chorel, T. Lanternier, E. Lavastre, N. Bonod, B. Bousquet, and J. Néauport, "Robust optimization of the laser induced damage threshold of dielectric mirrors for high power lasers," *Optics express*, vol. 26, no. 9, pp. 11764–11774, 2018.

[148] T. Willemsen, M. Jupé, M. Gyamfi, S. Schlichting, and D. Ristau, "Enhancement of the damage resistance of ultra-fast optics by novel design approaches," *Optics express*, vol. 25, no. 25, pp. 31948–31959, 2017.

[149] T. Willemsen, M. Brinkmann, M. Jupé, M. Gyamfi, S. Schlichting, and D. Ristau, "Approaches toward optimized laser-induced damage thresholds of dispersive compensating mirrors applying nanolaminates," in *Laser-Induced Damage in Optical Materials 2017*, vol. 10447, p. 1044712, International Society for Optics and Photonics, 2018.

[150] M. Kaumanns, V. Pervak, D. Kormin, V. Leshchenko, A. Kessel, M. Ueffing, Y. Chen, and T. Nubbemeyer, "Multipass spectral broadening of 18 mj pulses compressible from 1.3 ps to 41 fs," *Optics letters*, vol. 43, no. 23, pp. 5877–5880, 2018.

[151] M. Kaumanns, D. Kormin, T. Nubbemeyer, V. Pervak, and S. Karsch, "Spectral broadening of 112 mj, 1.3 ps pulses at 5 khz in a lg 10 multipass cell with compressibility to 37 fs," *Optics Letters*, vol. 46, no. 5, pp. 929–932, 2021.

Acknowledgements

During my four years study in Garching, I have been learning a lot from the people around me. Without the help of these extraordinary people, I wouldn't be able to accomplish my PHD thesis. I would like to use this opportunity to address my sincere gratitude to those people.

First of all, I would like to thank my supervisor Professor Ferenc Krausz, who offers me this unique position and allows me to work in his outstanding LAP group surrounding with those kind, talented and ambitious colleagues. I am really horned to be part of your group. Thank you for your valuable suggestion and permanent support for my scientific work.

I am deeply grateful to my direct supervisor Dr. Vladimir Pervak. From the first day I came to Munich, he almost helped me everything from the contract, registration and extending my visa as well as other small stuff. Without his help, I could not be able to adapt to the life in Munich so quickly. He is always open to discuss any topic with me. Regarding my scientific work, Vladimir always give me invaluable and feasible suggestions. His idea and concept for scientific research have enlightened and guided me to the road of science. Thank you for sharing with me your valuable experience regarding the coating techniques. Also, my skill of preparing presentations and writing papers have been continuously improved with Vladimir's advice and feedback. Thank you for generous support during my four years' PHD study. It was a great memory of my life.

I would also like to thank all the members from our AMO group. Thank you Dr. Michael Trubetskov for always providing me valuable and constructive advice. Thank you for your support in the Optilayer software. Without it, I could not make ant dispersive mirror designs. Thank you Dr. Tatiana Amotchkina for teaching me characterizing the refractive index and all the help for my experiments. Many thanks to my colleague Daniel Hahner, who gave me plenty of useful suggestions. Thank you for sharing your experience and idea either scientific work or non-scientific work. In addition, many thanks to Daniel for helping me translate the abstract. I also would like to thank Bernd and Sigi, who are technicians in our group. Thank you for preparing substrates for me and doing the maintenance for the coating machines. I feel very pleasant to work with you guys. Moreover, I would like to thank Wolfgang Sturm from Ultrafast innovations. Thank you for preparing substrates for me when Bernd and Sigi are not available. And thank you for sharing lunch with me.

Many thanks to Keyhan Golyari for performing the FROG measurements. Thank you

for your effort to further improve the measurements. I have learnt a lot of knowledge about ultrashort laser from you.

I am also indebted to Mrs. Monika Wild, who helped me find the apartment when I arrived in Munich. Looking for an apartment is not easy in Munich especially for a person who can not speak German. I really appreciate your help.

I would like to thank my office mates: Dr. Yuya Morimoto, Dr. Maxim Tsarev, Tobias Saule and Daniel Hahner. Thank you for sharing the office with me. I enjoyed the talks with you, either about daily life or scientific work.

Many thanks to Dr. Kai Starke and Stefan Schrameyer from Cutting edge coating company. Thank you for your support to our IBS coating machine.

Thank all the members from our amazing Attoworld group. Thank you Prof. Stefan Karsch, Dr. Thomas Nubbemeyer, Dr. Martin Kaumanns, Dmitrii Kormin, Christina Hofer and Syed Ali Hussain for your collaboration. It is of great honor and pleasure to work with you.

I would like to my friends Dr. Jinwei Zhang, Dr. Qingcao Liu, Dr. Zilong Wang, Dr. Shaohua Sun, Yang Cui, Weiwei Li et al.. Thanks for all the parties and dinners that we had. The life in Munich became more colorful because of you.

Last but not least, I would like to thank all my family: my grandfather, my father and my mother. Thank you for always supporting and encouraging me to pursue my dream.